



MASTER THESIS

Magneto-optical anisotropy enhancement by Pt overcoats on Co films

by

Patricia Riego Saavedra

Supervisor: Dr. Andreas Berger

Date of defense: July 15th, 2015

ABSTRACT

In this work I have studied the effect of an ultrathin Pt overcoat onto epitaxial Co ($10\bar{1}0$) films with an in-plane easy axis of magnetization. Our samples are 8-cm-long strips, on which we have deposited epitaxial Co by means of sputter deposition. On top of the Co film, we have deposited an ultrathin Pt overcoat. The Pt overcoat has been deposited in a wedge-shaped form, with 0.3 nm of Pt thickness on one end, 1.8 nm of Pt on the other end, and an almost linear increase of Pt thickness in between, along the 8 cm of the strip. This particular sample choice has enabled a systematic measurement and allowed for an excellent homogeneity of the Co-film quality due to the simultaneous fabrication of entire sample sets. I have fabricated two different sets of samples, one of them with 20 nm Co, and the other with 100 nm Co, in order to study magneto-optical and magnetocrystalline effects. Reference samples have also been fabricated, deposited under the very same conditions, but without the Pt overcoat, to check for possible inhomogeneities along the strip induced by the growth or misalignments during the magneto-optical characterization measurements.

The effect of the thickness of the Pt overcoat on the magneto-optical anisotropy of Co has been studied by means of generalized magneto-optical ellipsometry (GME), a robust magneto-optical method. For a consistent explanation of the measured data, my analysis of the results incorporates magneto-optical anisotropy (MOA), allowing for a different coupling factor between light and magnetization depending on the orientation of the magnetization with respect to the easy axis of the material. Even if in most studies metallic ferromagnets are assumed to be magneto-optically isotropic, my experiments show a considerable level of magneto-optical anisotropy in Co, which is very substantially enhanced by depositing an ultrathin Pt overcoat layer. The approximation of magneto-optical isotropy is no longer good and leads to an inaccurate description of the magnetization vector. By means of the approach explained in this thesis, I have been able to quantify the degree of MOA, and to separate its effects from the rotation of the magnetization vector.

I have also studied how the Pt overcoat affects the magnetocrystalline anisotropy. For this I have combined GME and vibrating sample magnetometry (VSM). An increase in magnetocrystalline anisotropy is observed as the Pt overcoat thickness increases. This effect could be of potential interest for technological applications.

ACKNOWLEDGMENTS

I would like to deeply acknowledge my supervisor Dr. Andreas Berger for the opportunity he has given me to work in the Nanomagnetism group during this year, for all his help and guidance, for his ideas and active contributions to this work, and for his dedication and time.

I would also like to thank Lorenzo Fallarino for the hours he has spent with me in the lab, for patiently explaining me how to use the sputter, the VSM, the X-rays..., for his very useful pieces of advice, and for being always ready to help me. A huge thank you also goes to Jon Ander Arregi, who is always willing to help. He has explained me a lot about magneto-optics and he has taught me to handle the GME setup and all the Matlab programs, and very specially, he has transmitted me his passion for research.

Thanks a lot to the rest of the Nanomagnetism group, César, Paolo, Alba, Matteo and Nicolò. It has been a pleasure to work with you. Also, thanks to my master colleagues because of the nice environment they have created. Finally, many thanks to all the people who have supported me during this year.

OUTLINE

	Page
Introduction	1
1 - Basic concepts of magnetism	3
1.1 - Ferromagnetism and its energy contributions	3
1.2 - Stoner-Wohlfarth model of ferromagnetism	6
2 - Experimental techniques	9
2.1 - Fabrication techniques: sputter deposition	9
2.2 - Structural characterization techniques	11
2.2.1 - X-ray diffractometry (XRD)	12
2.2.2 - X-ray reflectivity (XRD)	14
2.2.3 - Spectroscopic ellipsometry	15
2.3 – Magnetic and magneto-optical characterization techniques	16
2.3.1 - Vibrating sample magnetometry (VSM)	16
2.3.2 - Generalized magneto-optical ellipsometry (GME)	16
3 - Sample fabrication and structural characterization	25
3.1 - Thickness calibrations	26
3.1.1 - Thickness calibrations of Ag, Cr, Co and SiO ₂	26
3.1.2 - Thickness calibrations for the Pt wedge	28
3.2 - Sample fabrication	30
3.3 - Crystallographic characterization. Epitaxy	32
4 - Generalized magneto-optical ellipsometry results	35
4.1 - Data quality	36
4.2 - Qualitative data from least-squares fitting of $\frac{\delta I}{I}$ maps	37
4.3- Quantitative analysis of the data	40
4.3.1- Pure rotation of magnetization without magneto-optical anisotropy	40
4.3.2- Pure rotation of magnetization with magneto-optical anisotropy	41

4.4- Overcoat thickness dependence of magneto-optical anisotropy	47
4.5 - Overcoat thickness dependence of magnetocrystalline anisotropy	50
5 - Vibrating sample magnetometry results	53
Conclusions	59
Appendix A: Analytical derivation of generalized magneto-optical ellipsometry parameters for systems with magneto-optical anisotropy	61
References	67

INTRODUCTION

Magnetism has fascinated humankind throughout the ages. From the first reported observations of lodestone by Greek philosophers in 600 B.C. to the studies by Oersted in 1820 that proved that an electric current creates a magnetic field, people were using the magnetic properties of materials to build compasses for navigation. But it was not until the XIXth century, after Oersted's discovery, that the science of magnetism took off, when the works of Oersted, Faraday and Maxwell, among others, unified electricity and magnetism. Ever since, the research field of magnetism and magnetic materials has not stopped advancing and is nowadays a very relevant field in condensed matter physics. Of course, the interest in magnetism is not only of fundamental character, as this phenomenon has a large number of applications, ranging from the already mentioned compasses to transformers, detectors or information storage, to name a few.

The topic that I have studied in my master thesis is magneto-optical anisotropy (MOA), an effect that arises in magneto-optics, but to which not much attention has been paid. As we have studied in this work, though, the consequences of MOA can be very relevant for a broad branch of research. Indeed, characterization methods based on magneto-optical effects [1] such as the magneto-optical Kerr effect (MOKE) [2,3], which are well-established tools for the study of magnetism, virtually always assume that the magneto-optical coupling Q which defines the magnetization-dependent elements in the dielectric tensor of the material does not depend on the orientation of the magnetization. This means that Q , which is a tensor, is assumed to be isotropic, neglecting the crystallographic structure and the symmetry of the system. This assumption is understood to be reasonable for metals, which display weak optical anisotropies [4]. Nevertheless, deviations from this assumption of magneto-optical isotropy have been studied in some systems such as FeSi and Ni [5], Co [6-8], Fe/Au superlattices [9] or permalloy structures [10]. Recently, MOA has been related to strain in epitaxial hcp Co films, and substantial differences between the magneto-optical couplings along different crystallographic directions have been reported for the type of Co films that I have fabricated in this work [11]. Neglecting MOA can thus lead to a misinterpretation of MOKE data, and it could be necessary to correct for its effect in future studies.

In this thesis, sputter-deposited epitaxial Co ($10\bar{1}0$) films have been coated with an ultrathin Pt film, whose thickness ranges from 0.3 to 1.8 nm, and the effect of this overcoat on the MOA has been systematically studied as a function of the Pt thickness via GME. I have observed that Pt enhances very substantially the MOA present in pure Co very significantly, obtaining a difference of 100% between the magneto-optical coupling factor for two nonequivalent crystallographic directions. The enhancement effect saturates once the overcoat is thick enough, of the order of 1.5 nm. The degree of MOA in our samples is very high and we see that neglecting this effect leads to an important error in the interpretation of the angle of magnetization.

Apart from the MOA, I have also studied the effect of the Pt overcoat on the magnetocrystalline anisotropy of Co, a property arising from spin-orbit coupling which leads to a preferred orientation of the magnetization along specific directions in the crystal. It is already known that the alloying of Pt with Co increases the magnetocrystalline anisotropy of Co [12] due to the large spin-orbit coupling of Pt, and this kind of alloys are widely used in magnetic storage media [13]. Indeed, as magnetic storage requires the stability of the information high anisotropy is desirable, because this makes it more difficult to switch the magnetization via thermal fluctuations, which would correspond to a thermal erasure of information. The effect of an individual Pt overcoat layer on a Co-film now allows for a very detailed study in how far Pt influences magnetic properties of an adjacent ferromagnetic film, and can enable to elucidate the underlying interface physics. This is an interesting and relevant subject, potentially even for magnetic storage applications, because Co/Pt and other magnetic multilayers are considered relevant candidates for information storage technology [14]. The studies of overcoat materials on Co, to my knowledge, have not investigated the effect on the magnetocrystalline anisotropy directly. However, overcoats in general are very important because they are needed for chemical protection of the magnetic materials and hence, their role is of great relevance in technology. An example of one of the overcoat materials that have been studied is hydrogenated amorphous carbon, which shows very good tribology and corrosion-resistance performance [15].

To sum up, this work supports previous results about MOA, and furthermore it demonstrates the possibility to enhance MOA to very substantial levels by adding an ultrathin Pt overcoat to Co. On the other hand, this work also shows a possible pathway to explore and modify magnetocrystalline anisotropy of ferromagnetic thin films.

This work is organized as follows. In Chapter 1 I will present basic concepts of ferromagnetism and magnetocrystalline anisotropy. I will also explain the simple Stoner-Wohlfarth model for a homogeneously magnetized particle, which I shall utilize to describe the behavior of our samples. In Chapter 2 I will explain the experimental techniques that I have used to fabricate and characterize my samples. Hereby, I will focus especially on the technique of generalized magneto-optical ellipsometry (GME). After that, in Chapter 3, I will explain how I have fabricated my samples, including the relevant calibrations that I have performed. Chapter 4 will be focused on the results obtained from GME measurements, showing that MOA is necessary to explain them consistently. I will present the measured values of the MOA and the magnetocrystalline anisotropy. In Chapter 5 I will present VSM results, which also probe the magnetocrystalline anisotropy. Finally, I will present the conclusions of this work and suggest possible future work.

Chapter 1

BASIC CONCEPTS OF MAGNETISM

In this chapter I will review the basic concepts of magnetism and magnetic ordering, discussing the most important energy contributions that give rise to magnetic order and to the hysteretic behavior of ferromagnetic materials. I will also introduce the Stoner-Wohlfarth model of ferromagnetism, a very simple model for hysteresis in a single-domain nanoparticle which describes the main parts of the field response curve in monocrystalline thin films.

1.1- Ferromagnetism and its energy contributions

Ferromagnetic materials are materials that possess spontaneous net magnetization below a certain critical temperature, called Curie temperature T_c , even in the absence of an applied magnetic field. The origin of magnetic ordering is the alignment of spins and lies in the fact that parallel and antiparallel configurations of spins have different energies. It is crucial to point out that the origin of this energy difference is not the dipolar interaction among the magnetic moment of the spins. Indeed, the energy difference between the parallel and antiparallel spins is several eV, an order of magnitude that cannot be accounted for with dipole-dipole interactions, which are only of the order of meV. Instead, the energy difference between the parallel and antiparallel configurations comes from the so-called exchange interaction, which is the basis of magnetic order [16].

Exchange interaction is a quantum phenomenon that arises from the combination of pure electrostatic interactions between electrons with the fact that two electrons (which are fermions) with the same spin cannot be in the same orbital quantum state, i.e., the Pauli exclusion principle. This quantum-mechanical principle constrains the wave-function of the electronic system to switch sign upon the exchange of two particles. As the wave-function has both spatial and spin parts, the symmetry properties of one of the parts affect the other one: the spin state of the system will thus influence the spatial distribution of the electrons and vice versa. So, even if electrostatic energy only depends directly on spatial coordinates and not on spins, the Pauli exclusion principle makes the spin affect the spatial coordinates [17]. Accordingly, the energy will eventually depend in an indirect manner on the spin state of the system.

A way to map this effective influence of the spin alignment in the case of a two-electron system is the Heisenberg Hamiltonian [17]

$$E_x = -J \widehat{\mathbf{S}}_1 \cdot \widehat{\mathbf{S}}_2, \quad (1.1)$$

where $\widehat{\mathbf{S}}_1$ and $\widehat{\mathbf{S}}_2$ are the dimensionless quantum-mechanical operators for the spin (normalized to \hbar), and J is the exchange integral, which accounts for the energy difference between the antiparallel and parallel states¹. The sign of J determines the type of coupling. If $J > 0$, the parallel alignment of the spins is favored, and their coupling is said to be ferromagnetic. Instead, if $J < 0$, the system prefers the antiparallel alignment and the coupling is antiferromagnetic. If one assumes a pairwise interaction of spins, Eq. (1.1) can be generalized to a sum of terms

$$E_x = -\sum_{i < j} J_{ij} \widehat{\mathbf{S}}_i \cdot \widehat{\mathbf{S}}_j. \quad (1.2)$$

Even if this energy contribution has the form of a dipolar interaction, one should always remember that its origin is purely quantum-mechanical.

Exchange interaction explains the origin of the spin alignment but does not account for the hysteretic behavior of magnetic materials. If there were no other energy contributions, the magnetization could take any direction in the material, i.e., it would be isotropic. However, this is not the case due to other energy contributions, such as magneto-crystalline anisotropy (MCA) and magnetostatic energy.

In crystalline materials, MCA occurs due to the fact that it is energetically more favorable for the magnetization to lie along a certain crystallographic axis, a phenomenon that arises from spin-orbit coupling [18]. There are certain crystal structures that due to their symmetry favor the alignment of the magnetization along a single given axis: such systems are called uniaxial. Other crystalline orders could give rise to biaxial, triaxial etc. anisotropy. In the case of the films grown for this work, the crystal structure is hexagonal close packed (hcp), which shows uniaxial MCA. In this case, it is energetically favorable for the magnetization to lie along the crystallographic c -axis of the Co, which is the so-called easy axis (EA). There is an energy cost to divert the magnetization away from the EA, and for the case of hcp-type crystals this contribution can be written as [17]

$$E_{MCA} = K_0 + K_1 \sin^2 \gamma + K_2 \sin^4 \gamma + \text{higher order terms}, \quad (1.3)$$

where K_1 and K_2 are anisotropy constants and γ is the angle between the magnetization and the easy axis.

Another energy contribution we have to consider is magnetostatic energy, which arises from the interaction of a magnetic moment with other magnetic moments in the same sample and can be expressed as follows:

$$E_s = -\frac{1}{2} \int \mathbf{M} \cdot \mathbf{H}_s \, dV. \quad (1.4)$$

The effect of the distribution of magnetic moments is introduced via the magnetic field it creates. This field is the magnetostatic field \mathbf{H}_s . In order to understand its origin, consider a

¹ If the spin state is a singlet (antiparallel) then $\widehat{\mathbf{S}}_1 \cdot \widehat{\mathbf{S}}_2 = -\frac{1}{4}$, if it is a triplet (parallel), $\widehat{\mathbf{S}}_1 \cdot \widehat{\mathbf{S}}_2 = \frac{3}{4}$. Thus $E(\text{singlet}) - E(\text{triplet}) = J$.

uniformly magnetized finite sample without any applied external field. At the surface, the sudden change in the magnetization produces a non-vanishing divergence. From Maxwell's equations we know that $\nabla \cdot \mathbf{H} = -\nabla \cdot \mathbf{M}$, so that a field opposing the magnetization is created at the surface. This field depends strongly on the shape of the magnet and only has analytical solutions for particular geometries, such as ellipsoids or thin films. In the latter case, the one we are interested in, the magnetostatic energy favors an in-plane alignment of the magnetization, thus giving rise to an extra source of anisotropy, the so-called shape anisotropy.

The last term to consider in this discussion² is the energy contribution that arises from the interaction of the magnetized sample with an externally applied magnetic field \mathbf{H} . This is the so-called Zeeman energy, which can be written as

$$E_Z = - \int \mathbf{M} \cdot \mathbf{H} dV. \quad (1.5)$$

This energy term favors the alignment of the magnetic moments of the magnet with the external field.

The sum of these four contributions E_x , E_{MCA} , E_S and E_Z is the total energy of the magnetic system, which has to be minimized to obtain the equilibrium state. Several aspects have to be considered when tackling the problem. First, the problem cannot be solved analytically in most of the cases. One should note that the E_S term has to be calculated self-consistently, because \mathbf{H}_S depends on the magnetization of the system. Second, a ferromagnetic sample tends to separate into domains. The domains are regions of the material in which the microscopic magnetic moments are aligned in a parallel manner, as favored by the exchange energy for $J > 0$, thus giving rise to a non-zero magnetization. However, this has a cost in magnetostatic energy and systems tend to minimize it by creating other regions in which the magnetization is in another direction. Eventually, if the applied field is zero, the net magnetization of the material, taking into account all its domains, will be zero in most of the cases. Creating these domains reduces magnetostatic energy, but it has a cost in exchange energy (it increases it because in the boundaries of the domains the magnetic moments are not parallel, as would be favored by E_x), and forces appear in the domain walls. Finally, as we shall see, minimizing the total energy is not enough to determine the state of the system, because the magnetization also depends on the history of the system. It may happen that the absolute minimum of the energy is not accessible because the system is in a local minimum and the energy barrier is too high to be overcome by thermal fluctuations. Under such circumstances the system will be in a metastable state.

The fact that the state of the system depends on its history is reflected in the well-known M vs H hysteresis loop exhibited by ferromagnetic materials, which is schematized in Fig. 1.1. Here, the value of the magnetization projected onto the axis along which the magnetic field H is applied ($M_{||}$) is plotted as a function of H . Relevant quantities in a hysteresis loop are

² There are other energy terms that might be necessary to include in certain circumstances, such as terms that couple the magnetic degree of freedom to others, e.g. magnetoelastic energy.

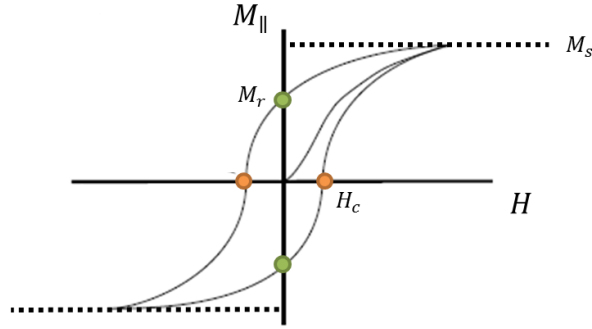


Fig. 1.1: Schematics of a hysteresis loop in a ferromagnetic material. Dotted lines represent the saturation magnetization. Green dots indicate the remanence magnetization, orange ones the coercive field. The curve that appears inside the hysteresis loop and that begins at the (0,0) point is the virgin magnetization curve.

the saturation magnetization M_s , which is the maximum value the magnetization can achieve, the remanence magnetization M_r , which is the value of the magnetization at $H = 0$, and the coercive field H_c , the value of the field needed to get zero magnetization. When the sample is initially unmagnetized one can magnetize it by applying a magnetic field. $M_{||}$ vs H then follows the curve in Fig. 1.1 that passes through the (0,0) point and is enclosed inside the hysteresis loop. This path is called the virgin magnetization curve.

1.2- Stoner-Wohlfarth model of ferromagnetism

A simple model for a single-domain uniaxial ferromagnetic material under the influence of an external magnetic field was proposed by Stoner and Wohlfarth in 1948 [19,20]. The model assumes that the material has homogeneous magnetization $M = M_s$ which rotates upon applying an external field H , an approximation that is suitable for small particles whose magnetic state has a single domain. Assuming only first order anisotropy, the energy of the system can be expressed as

$$E_{SW} = K \sin^2 \gamma - M_s H \cos(\gamma - \delta). \quad (1.6)$$

In this equation γ is the angle between the EA and the magnetization, and δ is the angle between the EA and the external field (see Fig. 1.2). With the assumption of homogeneous magnetization the exchange coupling is isotropic so it does not appear in this expression because it is just a constant term, independent of the angle. The anisotropy constant K takes into account both the K_1 term in equation (1.3) and the effect of the shape anisotropy. The term $2K/M_s$ is called the anisotropy field H_K and is the field needed to saturate the magnetization along the hard axis. The second term is the Zeeman energy, which tends to align the magnetization with the applied field.

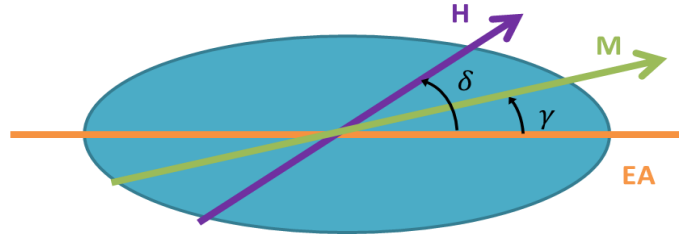


Fig. 1.2: Representation of the Stoner-Wohlfarth model.

The Stoner-Wohlfarth model is very useful to account for hysteresis loops. In the absence of an applied field, the system has two stable configurations with the magnetization along the EA direction. If the magnetic field is applied along the EA, i.e., if $\delta = 0$, the resultant hysteresis loop can be explained via the diagrams in Fig. 1.3. If the field is initially positive and has a large value, the magnetization is pointing in the field direction (I), because in this case there is only one minimum in the energy landscape. As the field is decreased and reverses its sign, the absolute minimum of the system corresponds to the magnetization pointing in the field direction, but there is a range of fields in which the initial state is still metastable and the system cannot overcome the energy barrier to jump to the most stable state (IV). As the field is further decreased, the absolute minimum is populated (V). The point at which the magnetization switches (V and X) is determined by the value of the anisotropy field H_K .

For the general case where $\delta \neq 0$ the minimization of the energy leads to hysteresis loops of different shapes. Figure 1.4 shows two examples where the angle between the applied field and the EA is 45° and 90° . This last one corresponds to the hard axis (HA), i.e., the axis along which the magnetization is least favored energetically. In this case, the magnetization undergoes a rotation and does not jump. The area of the hysteresis loop is zero and the curve passes through (0,0). By looking at equation (1.6) we see that when $H = 0$ the magnetization is favored to lie along the EA ($\gamma = 0$). Now, remember that the magnitude plotted in the hysteresis loop is the projection of the magnetization along the field axis. Thus, when the field is along the HA, zero field will lead to zero magnetization along the field axis. For any other orientation of the field that is not parallel to the EA or the HA, a combination of rotation and switching will occur, giving rise to hysteresis loops of different shapes.

The films I have fabricated have a very well-defined uniaxial anisotropy, and as long as one avoids the immediate vicinity of the coercive field they are in a homogeneous magnetization state. Vibrating sample magnetometry results indicate that from saturation to remanence the samples are well described by the Stoner-Wohlfarth model. Hence, this model will be utilized in this work to analyze the behavior of the samples.

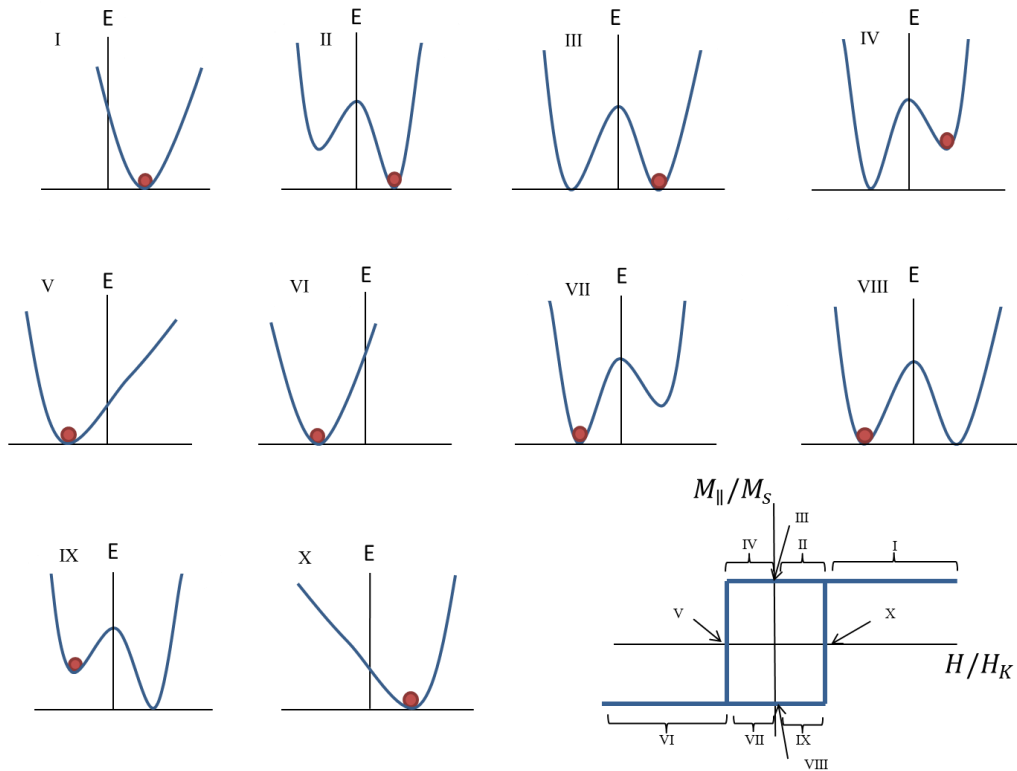


Fig. 1.3: Schematics of the energetic landscape and corresponding hysteresis loop for the Stoner-Wohlfarth model when the field is applied along the EA. The last figure shows the resulting hysteresis loop, showing the magnetization parallel to the applied field vs the magnitude of the applied field.

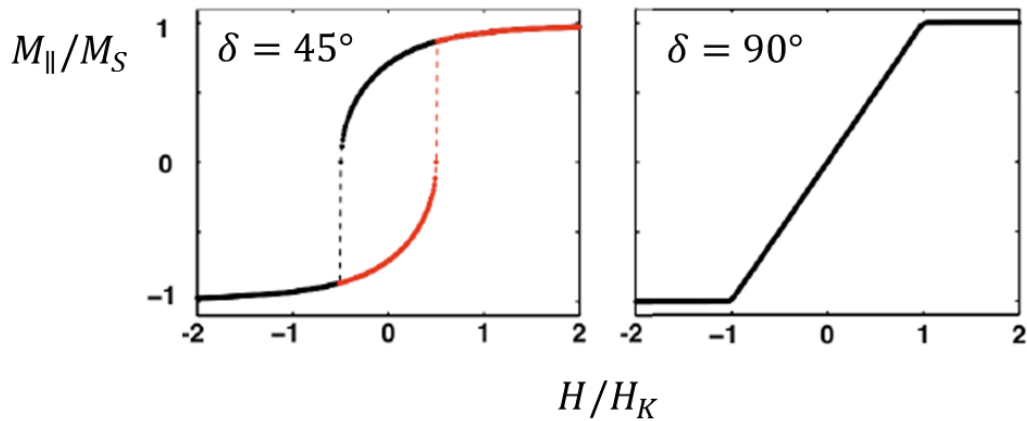


Fig. 1.4: Calculated hysteresis loops with the Stoner-Wohlfarth model, for angles between magnetic field and EA of 45° and 90° [21].

Chapter 2

EXPERIMENTAL TECHNIQUES

This chapter describes the different experimental techniques that have been used during the thesis. The chapter is divided in three sections. In the first one I will discuss the technique I have used to fabricate our samples, namely, sputter deposition. In the second section, structural characterization techniques will be explained, namely, X-ray diffractometry and X-ray reflectivity, as well as spectroscopic ellipsometry. Finally, vibrating sample magnetometry (VSM) and generalized magneto-optical ellipsometry (GME) will be discussed, which have been used to characterize the samples magnetically and magneto-optically.

2.1- Fabrication techniques: sputter deposition

The growth of our samples has been made by means of the sputter deposition technique [22]. Sputtering can be classified as a physical vapor deposition (PVD) technique, as no chemical reaction is involved in the procedure. This technique is very suitable for thin film growth due to its robustness and stability. The basic principle of the sputter process is to bombard with ions a target which, as a consequence of the collision, will eject atoms. These atoms are then deposited on a substrate for the purpose of film or multilayer growth.

A schematic picture of the sputtering process can be seen in Fig. 2.1. The target of the material that is to be deposited is placed in a gun, facing a holder in which the substrate is placed. The system is inside a vacuum chamber. A suitable gas (in this work chemically inert Ar has been used) is introduced in the chamber and is kept at a suitable pressure³. Then a negative voltage (with respect to the chamber walls, which are grounded) is applied to the target that is going to be sputtered, and which correspondingly works as an electrode. Free electrons that are present in the chamber are thus accelerated away from the target and some of them collide with the neutral atoms of the gas inside the chamber. The interaction of the free electrons with the outer shell electrons of the gas atoms provokes the ionization of such gas atoms and, in the case of Ar, we will have Ar⁺.

Hence, a plasma containing positively charged ions is created in the neighborhood of the gun. Now, these positively charged ions are accelerated towards the target and the subsequent energy and momentum transfer are enough to expel atoms (or other neutral

³ Unless otherwise stated, the Ar pressure that has been used in this work is 3 mtorr.

entities such as clusters of atoms) from the surface of the material. These target atoms then move ballistically away from the target, in arbitrary directions. Some of the atoms will reach the substrate and will contribute to the process of film growth.

In the process of extracting the target atoms, free electrons are also created, which in turn are able to produce more positive ions out of the gas molecules. The process is thus self-sustained as long as the potential of the cathode (the target) is sufficient. This avoids the use of an external ion gun, making this type of sputter deposition setup efficient and compact. Meanwhile, some free electrons interact with the gas ions and either recombine with them or produce excitations that decay afterwards. In these processes photons are emitted, making the plasma glow.

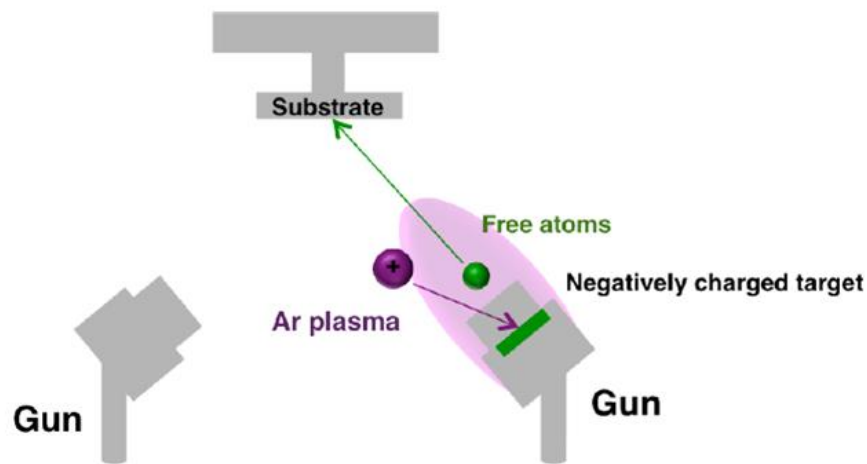


Fig. 2.1: Schematics of the sputtering process by an Ar plasma [21].

The most commonly used sputtering technique is magnetron sputtering. This technique uses a magnetic field to trap the free electrons. By doing so, electrons ionize more efficiently the gas around the gun and the plasma can be generated using lower gas pressures. As there is less gas in the chamber, the possibility to incorporate atoms of the gas into the film we are growing is reduced and, moreover, the collisions of the atoms ejected from the target with the gas atoms or ions are minimized, resulting in higher deposition rates. The magnetic field around the gun is created by a set of hard magnets placed behind the target. One pole is positioned in the axis of the target, and a second one is formed by a ring of magnets that are located around the outer edge of the target.

For the sputtering of metals, DC voltages are usually applied to the targets. As explained above, neutral entities as well as electrons are removed from the surface of the target, leaving in principle the system positively charged. However, in a metal, electrons coming from the circuit will be able to flow to the surface and neutralize it. Instead, if DC voltages were used to sputter insulators, there would be a positive charge accumulation at the surface. To avoid this, one needs to use AC voltages, specifically radiofrequency (RF) voltages. During the negative half cycle, positive ions of the gas will collide against the target and produce erosion, leaving the surface positively charged. This charge at the surface of the target

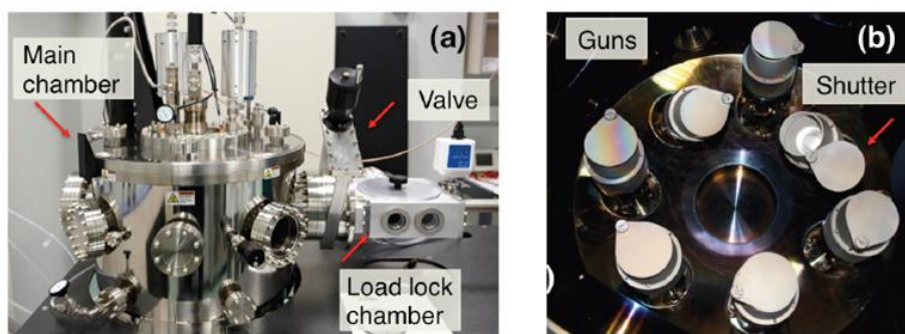


Fig. 2.2. AJA Sputter deposition system. (a) Outside view of the main chamber and the load lock chamber. (b) Inside view of the main chamber. The seven guns are visible. [21]

is neutralized during the positive cycle, when the target attracts free electrons that are present in the chamber towards it. As a consequence, sputtering only occurs in the negative half cycles, leading to lower deposition rates than in DC sputtering.

The sputter instrument available at nanoGUNE is the ATC series UHV sputtering system from AJA International, Inc. Company (Fig. 2.2), which uses the magnetron sputtering technique mentioned above. It has seven sputtering guns with automatized shutters and 6 power supplies (4 DC and 2 AC), so it has the capability to deposit simultaneously 6 materials, having thus a great potential to create novel compounds. Alternatively, it allows the deposition of multilayer structures without having to change the power supply from one gun to the other, thus minimizing the time between subsequent layer depositions.

The instrument has an ultrahigh vacuum (UHV) chamber that enables pristine cleanliness of the process and a better quality growth of the films. In addition to the main chamber, the instrument has a load lock chamber that can attain 10^{-7} mtorr. This chamber is used to load the substrate into the main chamber and to set up the configuration to start the deposition in a fast manner. Indeed, for the low volume load lock chamber, it takes only about 2 minutes to achieve a pressure of 10^{-7} mtorr starting from ambient pressure and when the sample is then introduced into the main chamber, the pressure of the latter is not altered in any significant way. If one were to load the substrate by opening the main chamber instead, the waiting time for the pressure inside it to be low enough to ensure a good deposition conditions would be several hours.

The AJA sputter also allows the manual control of the tilt of the seven guns while the deposition is ongoing. This permits the growth of wedge structures as the ones fabricated in this thesis (Secs. 3.1 and 3.2). Also, the sample holder can rotate, allowing for a very homogeneous deposition, if this is required by the intended sample structure.

2.2- Structural characterization techniques

The films grown by sputter deposition have to be calibrated and characterized in order to determine the thickness of each of the layers and their crystalline structure. This is crucial to

ensure that the samples meet the required properties, such as that the Co has been grown with an in-plane c -axis, as desired, or that the wedge overcoat has an appropriate thickness gradient. For the crystalline structure characterization, X-ray diffractometry has been used. For the thickness calibrations we have used X-ray reflectivity and spectroscopic ellipsometry techniques.

2.2.1- X-Ray diffractometry (XRD)

X-ray diffraction is a phenomenon that arises from the interaction of X-ray electromagnetic waves and matter. If the material under study has a crystalline structure, i.e., if its atomic structure has a periodicity, the scattering of X-ray waves with the atoms in the system will have a well-defined interference pattern [23,24]. Depending on the direction in which the scattering is observed, the interference will be constructive or destructive, producing a diffraction pattern of spatially varying intensity. The analysis of the diffraction pattern gives information about the symmetries of the crystal and the interatomic distances in it, which makes X-ray diffraction a widely used tool for the characterization and identification of crystal structures in a non-destructive way.

The measurement configuration is shown in Fig. 2.3(a). The X-ray tube forms an angle ω with the plane of the sample, and the detector forms an angle θ . The angle the sample rotates around the normal to its plane is called the azimuthal angle φ . The polar angle ψ (which is not shown in Fig. 2.3) is defined as the angle between the sample normal and the plane of incidence.

The configuration that has been used in this work to determine the crystallographic quality of the structures we have grown is the so-called $\theta - 2\theta$ configuration. In this case, $\omega = \theta$, $\psi = 0$, and the azimuthal angle φ is fixed. Figure 2.3(b) is showing this configuration. The condition for the constructive interference between the waves scattered at different planes is the so-called Bragg's law:

$$n \lambda = 2 d \sin\theta. \quad (2.1)$$

In this equation n is an integer that gives the interference order and λ is the wavelength of the X-rays. d and θ , both represented in Fig. 2.3(b), are, respectively, the interplanar distance and the angle of incidence of the wave with respect to the sample plane. With n and $\sin\theta$ being of the order of 1, λ should be of the order of the interatomic distances in order to be able to observe a diffraction pattern. As d is of the order of angstroms, λ has to be as well. That is why X-rays are being used for the structural characterization of crystals.

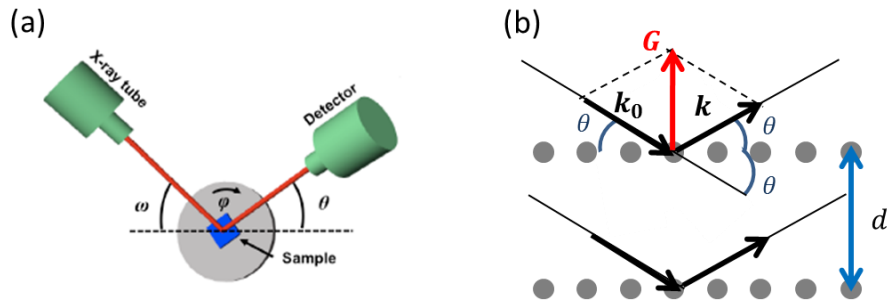


Fig. 2.3. (a) Perspective image of XRD measurement configuration with the representation of ω , θ and φ angles. (b) Schematic representation of the $\theta - 2\theta$ measurement scheme. \mathbf{k}_0 is the wave vector of the incident wave, \mathbf{k} the one of the scattered wave, and $\mathbf{G} = \mathbf{k} - \mathbf{k}_0$.

The vector \mathbf{k}_0 in Fig. 2.3(b) is the wave vector of the incident wave, and \mathbf{k} the wave vector of the outgoing wave. In the $\theta - 2\theta$ configuration, considering that the scattering is elastic (and thus $|\mathbf{k}_0| = |\mathbf{k}|$), one can easily prove that the vector $\mathbf{G} = \mathbf{k} - \mathbf{k}_0$ is normal to the plane. An equivalent of Bragg's law is the von Laue condition, which asserts that the diffracted amplitude has a maximum when \mathbf{G} is a reciprocal lattice vector. As a consequence, when performing $\theta - 2\theta$ scans on thin films, the reciprocal lattice vectors to which we are sensitive are the ones that are normal to the surface of the film. In other words, we are detecting interplanar distances among planes parallel to the sample surface. As an example of an XRD measurement we have Fig. 2.4, which shows a $\theta - 2\theta$ scan of a 100 nm thick epitaxial $(10\bar{1}0)$ Co sample.

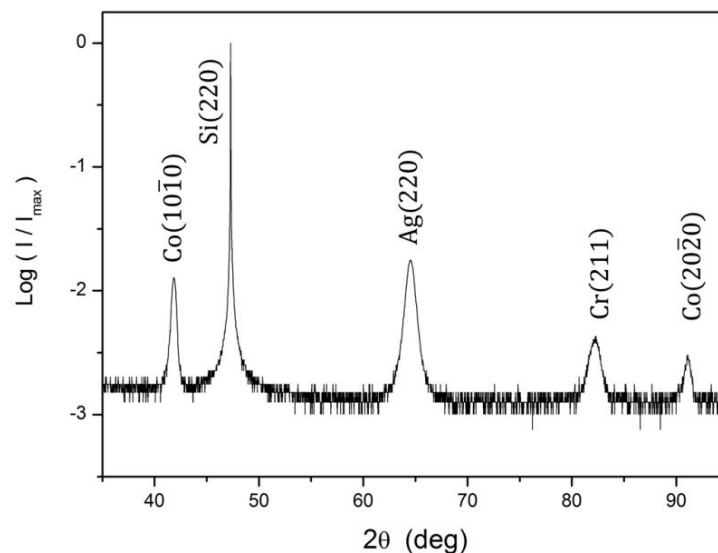


Fig. 2.4. X-ray $\theta - 2\theta$ diffraction measurement of a 100 nm thick epitaxial $(10\bar{1}0)$ Co film. The first and second order Co peaks are visible at $2\theta = 41.89^\circ$ and 91.27° respectively. The rest of the peaks correspond to the other elements present in the sample, which are necessary to obtain the desired crystal structure of Co (see Secs. 3.2 and 3.3).

A more detailed analysis of the crystallographic quality of the samples is achieved via φ -scans. These measurements allow the determination of the azimuthal orientation of the crystallites. In the case of the structures we have grown, a given plane of diffraction that is not parallel to the sample surface has been chosen. The sample is thus tilted by an appropriate ψ angle, specifically chosen for each element, and the θ and ω angles (with $\omega = \theta$) are fixed to a given value to obtain a specific diffraction peak. After setting ψ , θ and $\omega = \theta$, the sample is rotated along the surface normal, scanning the φ angle. A diffraction peak will appear when the plane of incidence of the X-rays is perpendicular to the selected plane of diffraction. Depending on the symmetry of the crystal the number of peaks that we find can vary, but there will be a peak at least for two different values of φ , with a shift of 180° . Only this measurement can provide information about the in-plane order, in order to distinguish epitaxial growth from an accidental texture and order in one direction that has nothing to do with the underlying crystals or template layers.

The X-ray diffractometer at nanoGUNE is an *X'Pert PRO PANalytical*. It uses a copper anode for the generation of X-rays. The radiation that is used corresponds to the K_α transition of Cu and has a wavelength of $\lambda = 1.54 \text{ \AA}$. Both the X-ray tube and the detector can be moved scanning the angles ω and θ . The sample can be rotated around the φ angle and the plane of the sample can also be tilted by changing the polar angle ψ . A database of the crystallographic phases of different materials and the angular position of their corresponding diffraction peaks is available via the software of the instrument. This tool has allowed me to identify the crystallographic structure of our samples and to confirm that the desired epitaxial growth has been achieved.

2.2.2- X-Ray reflectivity (XRR)

X-rays may also be used to determine the thickness of a thin film. The basis of the technique is to measure the interference pattern generated by reflected waves from the top and the bottom interfaces of a layer of thickness t as is shown schematically in Fig. 2.5(a). This distance is typically one, two or even three orders of magnitude larger than the interatomic distance. So, by looking at equation (2.1) and knowing that λ is kept constant and that it is of the order of angstroms, we infer that one has to look at very low angles to determine the thickness of thin films. For this reason, XRR uses grazing angle of incidence. The configuration in this case is also $\theta - 2\theta$. The interference pattern arising from the constructive and destructive interference of the waves reflecting on both interfaces (which in this context are called Kiessig fringes) gives information about the thickness of the layer [24,25].

The index of refraction of a material for electromagnetic waves in the range of X-rays is less than 1. Accordingly, when the X-ray wave travels from the air into the material, a critical angle θ_c exists, below which complete reflection will occur at the first interface, preventing any wave to penetrate the material. For angles above θ_c , reflections in the air-film and film-substrate interfaces are possible. Upon moving symmetrically the tube and the detector one obtains as a function of 2θ the kind of measurement that is depicted in Fig. 2.5(b). The period of the observed oscillations is related to the thickness of the thin film, which can be extracted by Fourier analysis or by means of a more elaborate fitting process.

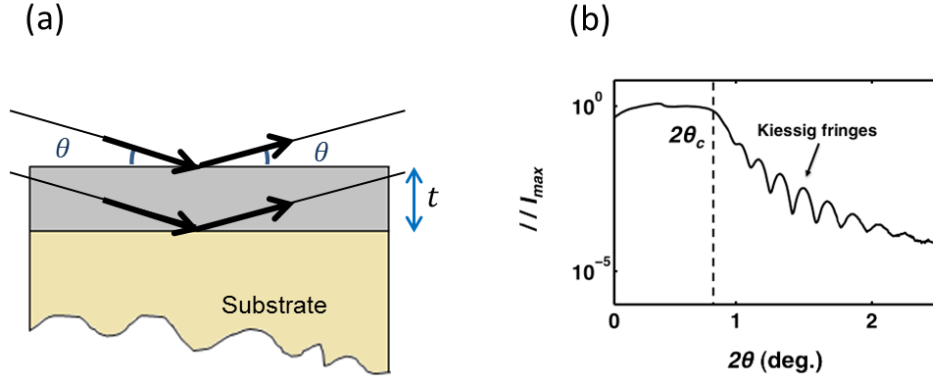


Fig. 2.5. (a) Grazing incidence configuration for XRR measurements. (b) Detected X-ray intensity as a function of the 2θ angle, giving rise to the so-called Kiessig fringes [21].

2.2.3- Spectroscopic ellipsometry

This technique has been used to provide information about the thickness of wedge sample structures I have grown. In this kind of samples the thickness of the deposited material changes with the position. The spectroscopic ellipsometer available at nanoGUNE can perform automatized measurements of the thickness in locations 1 mm apart, thus enabling one to obtain detailed profiles of wedge-shaped samples.

The basis of spectroscopic ellipsometry is the change in the polarization of light upon reflection from a sample. In Jones matrix formalism, the sample is represented by a reflection matrix. If the sample is not magnetized, as it is the case for this set of measurements, the reflection matrix can be written as

$$\mathbf{R} = \begin{pmatrix} r_s & 0 \\ 0 & r_p \end{pmatrix}, \quad (2.2)$$

where r_s and r_p are the Fresnel reflection coefficients for the s - and p - polarized waves (perpendicular and parallel to the plane of incidence, respectively). In spectroscopic ellipsometry a linearly polarized beam is reflected from the sample and the polarization becomes elliptic⁴. To measure the polarization change, the specific instrument at nanoGUNE utilizes a rotating compensator with a fixed analyzer. The amount of light allowed to pass will depend on the orientation of the compensator. This information is compared to the known input polarization to determine the polarization change caused by the sample reflection. The magnitude that is measured is the complex reflectance ratio

$$\rho = \frac{r_p}{r_s} = \tan(\Psi) e^{i\Delta}. \quad (2.3)$$

$\tan(\Psi)$ is the amplitude ratio between the p and s reflected components of the beam, while Δ is the phase difference in between them [26]. This ratio is measured for each photon energy,

⁴ If the incoming polarization is s or p , the polarization will not change upon reflection, because they are eigenstates of the reflection matrix (2.2). If the polarization is a combination of both, though, the reflected light will be elliptically polarized.

which ranges from 1.3 to 7.4 eV. By means of a model that includes the sequence of i materials and their optical constants ($n_i(\omega)$, $\kappa_i(\omega)$), a fitting of $\tan(\Psi)$ and $\cos(\Delta)$ permits one to obtain, amongst other quantities, the thickness of the layers, which has been the primary purpose of using this technique in this thesis.

2.3- Magnetic and magneto-optical characterization techniques

The magnetic characterization of the samples has been performed by means of two methods, namely Vibrating Sample Magnetometry (VSM) and Generalized Magneto-optical Ellipsometry (GME). The latter has also been used for the magneto-optical characterization. Both methods are explained in the following sections.

2.3.1- Vibrating sample magnetometry (VSM)

This method of characterization of magnetic samples is based on the well-known Faraday-Lenz law. A magnetized material is moved in between four pickup coils that detect the magnetic flux. The vibration of the sample makes the magnetic flux vary with time, which produces a potential difference that is proportional to the total magnetic moment of the sample [27]. VSM systems are typically equipped with electromagnets that generate an external magnetic field to enable measurements of the magnetization as a function of the applied field. One then makes the approximation that the applied field H varies so slowly as compared to the vibration frequency of the sample that it does not contribute to the time derivative of the magnetic flux.

The VSM system at nanoGUNE is The Princeton Measurements Corp. Model 3900 MicroMag™ VSM can apply up to 21000 Oe. In the case of this instrument, the pickup coils are aligned parallel to the applied field, so the setup is sensitive to the magnetic moment parallel to the applied field, although fundamentally VSM does not have to be like this. Our tool can measure signals as small as 0.5 μemu for an acquisition time of 1 s per point. In order to place the sample, whose size is limited to 8 x 8 mm², in the proper position, the VSM system has linear translation stages in the three directions of the space. Additionally, the instrument also enables the automatic rotation of the sample about the axis perpendicular to the applied field (and normal to the surface) by 360°, allowing for the measurement of hysteresis loops for different alignments of H and the EA.

2.3.2- Generalized magneto-optical ellipsometry (GME)

This characterization technique uses light as a probe and has its basis in the magneto-optical Kerr effect (MOKE). This effect was discovered by John Kerr in 1877, who observed that the polarization of light changes upon reflection from a magnetized sample [2]. A similar effect had been found in 1845 by Michael Faraday, although in this case the change in polarization was observed in the transmitted light. As metals exhibit strong light absorption, and thus the penetration depth Λ of visible light is rather small, of the order of 50 nm for Co, the Kerr effect

is more widely used for their magnetic characterization than the Faraday effect. Correspondingly, MOKE can be considered a surface-sensitive technique.

The macroscopic description of the MOKE is most useful for the purpose of the characterization of our samples. In the linear approximation, the effect that the magnetization of the material has with respect to light propagation can be described by introducing antisymmetric off-diagonal elements in the dielectric tensor. Assuming an optically and magneto-optically isotropic medium and only first order magneto-optical effects the dielectric tensor can be written as

$$\bar{\epsilon} = \epsilon \begin{pmatrix} 1 & -iQm_z & iQm_y \\ iQm_z & 1 & -iQm_x \\ -iQm_y & iQm_x & 1 \end{pmatrix}, \quad (2.4)$$

where ϵ is the dielectric constant of the material, Q is the magneto-optical coupling constant, also called Voigt constant, and m_x , m_y and m_z are the components of the normalized magnetization vector $\mathbf{m} = \mathbf{M}/M_s$. It should also be stressed that when writing down the dielectric tensor (2.4) magneto-optical isotropy has been assumed. As we shall see later, however, the samples that I have grown and characterized in this work show magneto-optical anisotropy. This effect will be introduced in due time, and here we consider the simplest possible case to illustrate the theory of the MOKE.

The three types of MOKE depending on the direction of the magnetization with respect to the plane of incidence are depicted in Fig. 2.6. The longitudinal Kerr effect is shown in (a). In this case, the sample is magnetized parallel both to the sample surface and the plane of incidence. Transverse MOKE is shown in (b), where the magnetization is parallel to the sample surface and perpendicular to the plane of incidence. Finally, the polar MOKE is shown in (c), in which the magnetization is perpendicular to the sample surface and contained in the plane of incidence. In the most general case there will be a combination of all three effects, which can even be present simultaneously.

By solving Maxwell's equation with the appropriate boundary conditions for a system with a dielectric tensor given by (2.4) one can obtain the magneto-optical Fresnel reflection matrix [1,3,29,30]

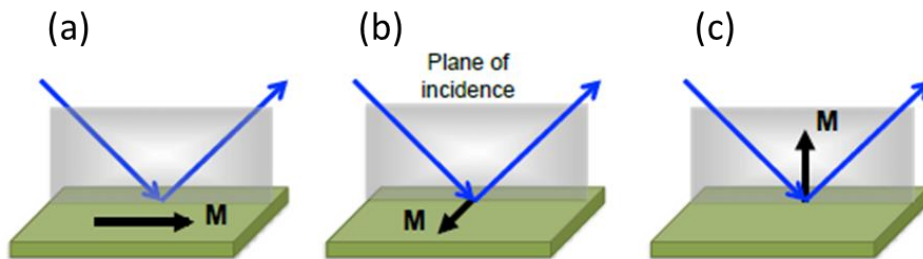


Fig. 2.6. The three types of MOKE. (a): longitudinal, (b): transverse, and (c): polar [28].

$$\mathbf{R} = \begin{pmatrix} r_{ss} & r_{sp} \\ r_{ps} & r_{pp} \end{pmatrix}. \quad (2.5)$$

Here r_{ss} , r_{pp} , r_{sp} and r_{ps} are the Fresnel reflection coefficients. r_{sp} and r_{ps} are zero if the material is not magnetized, and r_{pp} has a magnetically induced component as well.

The change in polarization upon reflection in MOKE arises from a combination of a rotation of the plane of polarization and a change in the ellipticity. Figure 2.7 represents the case where the incident beam is s polarized. Upon reflection on a magnetized sample, the polarization plane is rotated by an angle θ_K and the ellipticity, which was originally 0 for the linearly polarized incident light, becomes ϵ_K . If the sample were not magnetic, the off-diagonal elements of the reflection matrix (2.8) would be zero and the outgoing light would also be s polarized, because s -polarized light would be an eigenstate of such reflection matrix (See footnote 4 in Sec. 2.2.3). Conventional MOKE magnetometry is used as a hysteresis loop tracer by measuring the detected light intensity as a function of H . The intensity changes because, as H magnetizes the sample, the Kerr rotation and ellipticity change, as they depend on the magnetic state of the sample. Thus, making the reflected light pass through a polarizer, which is commonly referred to as an analyzer, the intensity collected at a detector will depend on H .

GME goes beyond the standard magneto-optical measurement techniques and aims at the characterization of the complete reflection matrix \mathbf{R} [31,32], which is the maximum information one can extract in a reflection experiment with polarization degree conservation. Using a simple reflection experiment, \mathbf{R} can be determined up to a constant. In the case where there is no polar MOKE component⁵ the reflection matrix in (2.5) can be written as

$$\mathbf{R} = \begin{pmatrix} r_s & \alpha \\ -\alpha & r_p + \beta \end{pmatrix} = r_p \begin{pmatrix} \tilde{r}_s & \tilde{\alpha} \\ -\tilde{\alpha} & 1 + \tilde{\beta} \end{pmatrix} = r_p \tilde{\mathbf{R}}, \quad (2.6)$$

where r_s and r_p are the Fresnel coefficients that also arise when the reflection from a nonmagnetic planar sample is studied [29], as explained in Sec. 2.2.3, and α and β are magnetically induced reflection elements. r_s and r_p are independent of the magnetization, but α and β are not. Specifically, α depends on the longitudinal MOKE, while β depends on the transverse one. An important property that holds in the linear approximation is that α and β switch their sign upon magnetization reversal, i.e., $\alpha(-\mathbf{M}) = -\alpha(\mathbf{M})$ and $\beta(-\mathbf{M}) = -\beta(\mathbf{M})$.

With the procedure that we shall now describe to extract the information of $\tilde{\mathbf{R}}$ and by means of the appropriate optical modeling, one can extract the index of refraction $n + ik$ and the magneto-optical coupling constant $Q = Q_r + iQ_i$ of the medium. Furthermore, the knowledge of $\tilde{\mathbf{R}}$ allows one to determine the orientation of the magnetization because, importantly, each of the components of the magnetization affects the reflection coefficients in a different manner, so GME is also a precise vector magnetometry technique [33].

⁵ We can restrict ourselves to the longitudinal and transverse cases, because as our thin films have an in-plane EA, the shape anisotropy favors in-plane magnetization and the magnetic field is applied parallel to the film surface, the polar component is virtually zero.

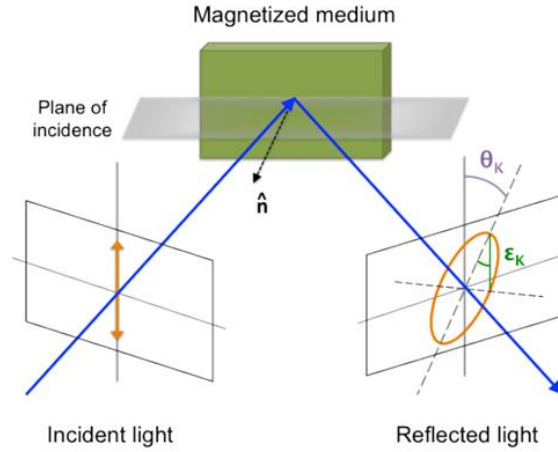


Fig. 2.7. Schematics of the MOKE when the incident wave is s polarized. Upon being reflected in a magnetized sample the plane of polarization rotates by an angle θ_K and light acquires an ellipticity ϵ_K .

The basic GME setup is sketched in Fig. 2.8. A laser providing linearly polarized light is used as a source. This light passes through a rotating linear polarizer P_1 before the sample. After being reflected by the sample, which is placed between the poles of an electromagnet, the light passes through a second rotating linear polarizer P_2 . Finally, the light is detected in a photodetector.

The intensity I measured at the detector is

$$I = \mathbf{E}_D \cdot \mathbf{E}_D^*, \quad (2.7)$$

where \mathbf{E}_D is the electric field at the detector. \mathbf{E}_D can be computed by using Jones' formalism. For this, we need to multiply the Jones matrices of each optical element in the appropriate order:

$$\mathbf{E}_D = \mathbf{P}_2 \cdot \mathbf{R} \cdot \mathbf{P}_1 \cdot \mathbf{E}_L, \quad (2.8)$$

where \mathbf{E}_L is the electric field vector of the light before passing the first polarizer, and \mathbf{P}_1 and

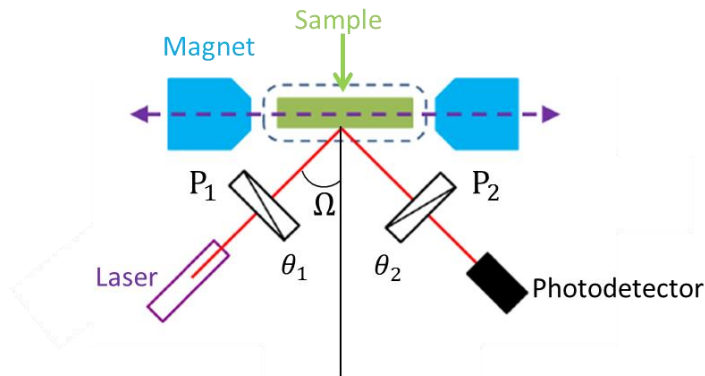


Fig. 2.8. Schematics of the GME setup. θ_1 and θ_2 are the polarizer angles, Ω is the angle of incidence.

P_2 are the Jones matrices for the linear polarizers P_1 and P_2 , which can be written as

$$P_i = \begin{pmatrix} \cos^2 \theta_i & \sin \theta_i \cos \theta_i \\ \sin \theta_i \cos \theta_i & \sin^2 \theta_i \end{pmatrix}. \quad (2.9)$$

Here, θ_i is the angle of the polarizer axis with respect the s polarization orientation.

Let us call I^+ the detected intensity when the magnetization is $+\mathbf{M}$ and I^- the detected intensity when the magnetization is $-\mathbf{M}$, so that $I^\pm = I(\pm\alpha, \pm\beta)$. These two magnetic states are achieved by applying an external magnetic field H , and the (I^+, I^-) pairs are determined by the H and the $-H$ data from the two different branches of the hysteresis loop, as it can be seen in Fig. 2.9, because only those fulfill the requirement of time reversal, i.e., $M(H) = -M(-H)$, and thus the corresponding inversions of the MOKE contributions to the reflection matrix. We define

$$\delta I = I^+ - I^- \quad (2.10)$$

and

$$I = \frac{1}{2}(I^+ + I^-). \quad (2.11)$$

Taking into account also a I_0 term that represents the background signal and accounts for the aspects that are not considered in the model, e.g. dark current, light that is not coming from the laser, the loss of complete polarization or imperfections of the polarizers, it can be proven that the relative change in intensity upon magnetic state reversal can be written as

$$\frac{\delta I}{I} = 4 \frac{B_1 f_1 + B_2 f_2 + B_3 f_3 + B_4 f_4}{I_0 + f_3 + B_5 f_5 + 2B_6 f_4}. \quad (2.12)$$

The f_i functions depend on the angles of the P_1 and P_2 polarizers:

$$f_1(\theta_1, \theta_2) = \sin^2 \theta_1 \sin \theta_2 \cos \theta_2 - \sin^2 \theta_2 \sin \theta_1 \cos \theta_1 \quad (2.13.a)$$

$$f_2(\theta_1, \theta_2) = \cos^2 \theta_2 \sin \theta_1 \cos \theta_1 - \cos^2 \theta_1 \sin \theta_2 \cos \theta_2 \quad (2.13.b)$$

$$f_3(\theta_1, \theta_2) = \sin^2 \theta_1 \sin^2 \theta_2 \quad (2.13.c)$$

$$f_4(\theta_1, \theta_2) = \sin \theta_1 \cos \theta_1 \sin \theta_2 \cos \theta_2 \quad (2.13.d)$$

$$f_5(\theta_1, \theta_2) = \cos^2 \theta_1 \cos^2 \theta_2. \quad (2.13.e)$$

The B_i parameters are related to the elements of the reduced reflection matrix $\tilde{\mathbf{R}}$

$$B_1 = \text{Re}(\tilde{\alpha}) \quad (2.14.a)$$

$$B_2 = \text{Re}(\tilde{r}_s \tilde{\alpha}^*) \quad (2.14.b)$$

$$B_3 = \text{Re}(\tilde{\beta}) \quad (2.14.c)$$

$$B_4 = \text{Re}(\tilde{r}_s \tilde{\beta}^*) \quad (2.14.d)$$

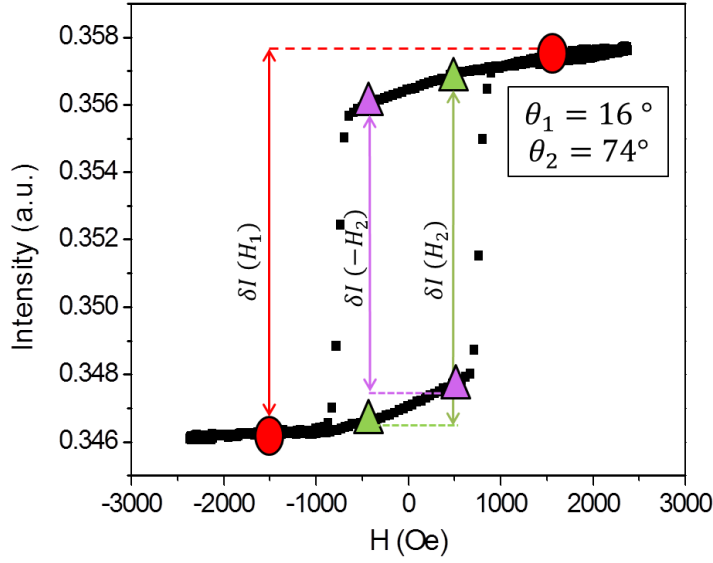


Fig. 2.9. Measured hysteresis loops for a given pair of (θ_1, θ_2) polarizer angles. δI is represented for $H_1 = 1500$ Oe in red, $H_2 = 500$ Oe in red and $-H_2 = -500$ Oe in purple.

$$B_5 = |\tilde{r}_s|^2 \quad (2.14.e)$$

$$B_6 = \text{Re}(\tilde{r}_s). \quad (2.14.f)$$

As one can see, B_1 and B_2 are related to the longitudinal MOKE, whereas B_3 and B_4 are related to the transverse one. Finally, B_5 and B_6 are purely optical constants.

The determination of the B_i parameters for each value of H can be done experimentally by measuring the $\frac{\delta I}{I}$ quantity for various θ_1 and θ_2 angle pairs. Although in principle only six measurements of hysteresis loops with varying (θ_1, θ_2) polarizer angles would suffice for a complete determination of $\tilde{\mathbf{R}}$ for all the available range of field values, it is much more precise to acquire a larger set of data, typically with more than 400 (θ_1, θ_2) configurations, building for each value of H what we call a $\frac{\delta I}{I}(\theta_1, \theta_2)$ map (as the ones shown in Fig. 2.10). Then, the B_i parameters are obtained by least-squares fits using Eq. (2.12). Furthermore, this over-determination of the B_i factors allows one to check the consistency of the data sets, which is typically excellent. Two additional fitting parameters are introduced, namely, the corrections for the polarizer angles, which we call θ_1^0 and θ_2^0 . These are included in the model because there might be a misalignment in the setup, as it is difficult to align the polarizers with a plane of incidence that one cannot see. We shall focus more on the quality of the data in Sec. 4.1, with the actual measurements performed in this thesis, but we should say that very good agreement is generally obtained between the measured and the fitted maps. Fig. 2.10 shows side by side a measured $\frac{\delta I}{I}(\theta_1, \theta_2)$ map and a fitted one, and we can see that the fit quality is exceptional. Typically, the obtained R^2 values of these multiparameter fits are above 0.95.

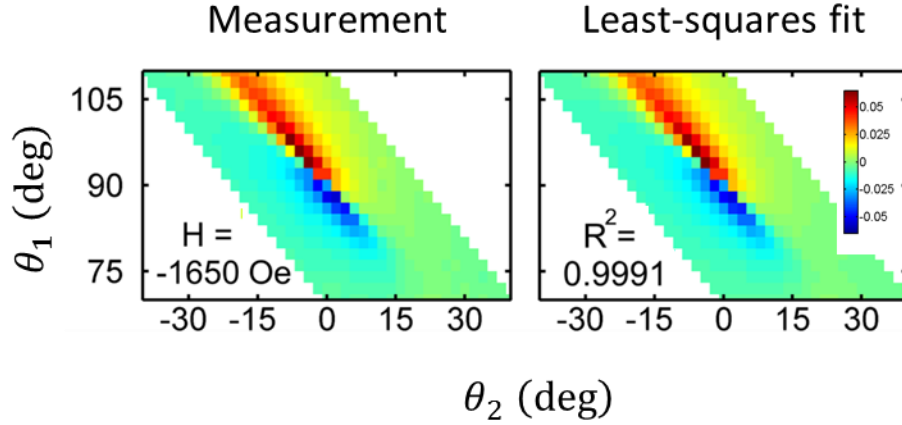


Fig. 2.10. Side-by-side comparison of measured GME $\frac{\delta I}{I}(\theta_1, \theta_2)$ map at $H = -1650$ Oe and least-squares fit with equation (2.15).

The actual GME setup that has been used in this work can be seen in Fig.2.11. All the optical elements are mounted on an optical table for the suppression of vibrational noise. The incidence angle in our experiment is $\Omega = 45^\circ$. We use a laser with $\lambda = 635$ nm, coherent and intensity-stabilized light. The polarization of the laser is linear, and the beam is passed through a $\lambda/4$ retarder in order to obtain a circularly polarized light before the beam passes through the first rotatable polarizer P_1 . The presence of the retarder does not change the GME formulation, which does not assume a specific incident polarization of the beam before passing through P_1 . Moreover, if the beam were linearly polarized before passing through the first polarizer, rotating P_1 would lead to different light intensity reaching the sample for different θ_1 angles. This is far from ideal, as the signal to noise ratio, for instance, would depend on θ_1 . If the $\lambda/4$ retarder is used, light coming out of P_1 will always have the same intensity, regardless of θ_1 . It can be proved analytically that having a circularly polarized incoming light in the first polarizer makes the I_0 term independent of θ_1 . After passing through the first polarizer, the light gets reflected by the sample, which is mounted on a computer-controlled linear translation stage. This part of the setup permits the linear motion of elongated sample types, so that points with different overcoat thicknesses in our strip samples can be measured in an automatized fashion. The part of the sample that is illuminated by the laser is placed between the poles of an electromagnet that can achieve 1700 Oe at the sample position. The value of the field is measured by a Hall probe. Finally, the reflected beam passes through the second rotatable polarizer P_2 and is detected in a photodiode detector.

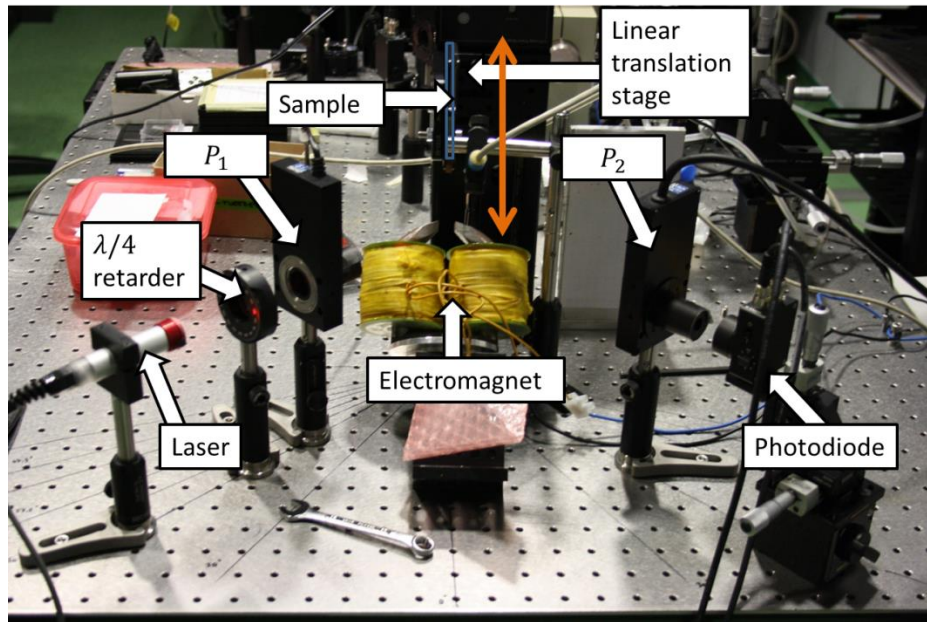


Fig. 2.11. Experimental setup of the GME. The elements are indicated in the picture.

Chapter 3

SAMPLE FABRICATION

AND STRUCTURAL CHARACTERIZATION

The technique that we have used to grow our samples is sputter deposition, which I have explained in Sec. 2.1. To obtain the desired crystal structure of Co, a series of processes has to be followed. The process to achieve epitaxial growth will be detailed in Sec. 3.2 and the explanation why this process works, together with the characterization of the crystal structure of the samples, will be shown in Sec. 3.3. As for now, all we need to know is that Si wafer has to be HF etched to remove the native SiO_2 and that two template layers of 75 nm Ag and 40 nm Cr have to be deposited before Co following the work in Refs. [21,34,35], so that Co grows showing the desired crystal structure.

Figure 3.1 shows the structure of our samples. The samples are grown on Si wafers cut in 5 mm x 8 cm strips. Along the main axis of the strip, a wedge-shaped Pt layer with thickness ranging from 0.3 to 1.8 nm is deposited on top of Co. The wedge structure provides a complete set of subsamples with different Pt thicknesses fabricated at the same time. The Co thickness is either 20 nm or 100 nm thick and is deposited on top of the aforementioned template layers. Finally, a 10-nm-thick SiO_2 protective layer is sputtered, to prevent the oxidation of the structure. Therefore, the sputter targets that are needed to fabricate the samples are Ag, Cr, Co, Pt and SiO_2 .

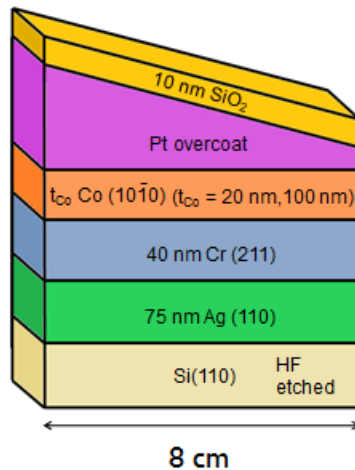


Fig. 3.1. Sample structure (not in scale). Pt overcoat thickness ranges from 0.3 nm to 1.8 nm.

I have fabricated three different kinds of samples, and two sister samples (A and B) have been sputtered at the same time for each of the kinds:

- 1) Pt20A and Pt20B: The Co layer is 20 nm thick and it has a Pt wedge-shaped overcoat.
- 2) Pt100A and Pt100B: The Co layer is 100 nm thick and it has a Pt wedge-shaped overcoat.
- 3) Ref20A and Ref20B: The Co layer is 20 nm thick and it has no Pt overcoat. These are reference samples to check whether the effects we see in the other samples are overcoat-induced or produced by some inhomogeneity.

3.1- Thickness calibrations

In order to establish the deposition time for each of the layers, I have performed thickness calibrations. For these calibrations, the materials have been sputtered on Si wafers without further treatment, as we are not concerned about crystallinity in these preliminary tests. I will first explain the procedure to calibrate Ag, Cr, Co and SiO₂, and I will then focus on the more complicated calibration of the Pt wedge.

3.1.1 - Thickness calibrations of Ag, Cr, Co and SiO₂

For the calibrations of Ag, Cr and Co, I have sputtered these materials separately on Si wafer chips. Three different calibration samples have been deposited for each material, with different deposition times. As for the deposition conditions, the Ar pressure in the main chamber of the sputter tool has been chosen to be 3 mtorr and the sample holder has been rotating to obtain homogeneous thickness in the whole area of the sample, which is placed in the middle of the holder. Ag has been deposited at 40 W, Cr at 100 W and Co at 100 W.

The thickness of the calibration samples has been measured with XRR technique. An example of the measurements is shown in Fig. 3.2, where the analysis of the Kiessig fringes

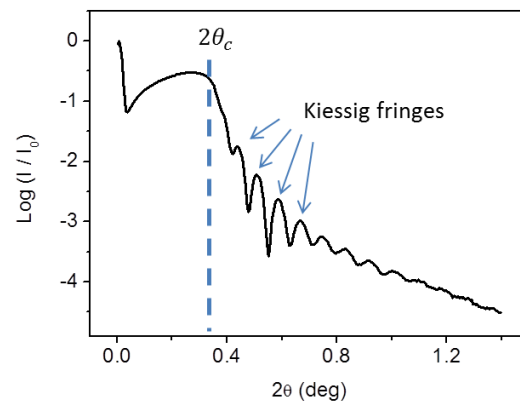


Fig. 3.2. Kiessig fringes obtained from XRR measurements on a film of Cr for a deposition time of 10 minutes. The thickness is 51.6 nm.

yields a thickness of 51.6 nm for a Cr thin film deposited for 10 minutes. The measured thickness for all the calibration samples is depicted in Fig. 3.3, for Ag, Cr and Co. The (0,0) point is included in the figures, as no deposition time obviously implies zero deposited thickness. To calculate the deposition rate of each material, I have performed a linear fit to the thickness vs. deposition time data. The linear fits are shown as red lines in Fig. 3.3. As we can observe, the linearity is excellent in the three cases, indicating that the sputtering process is stable over the time. The slope of the fitted straight lines gives the deposition rates, which are shown in each case at the bottom of each graph. Once the deposition rates are known, we know how long it takes to deposit the amounts of Ag, Cr and Co necessary for the planned epitaxial base structure [21,34,35].

75 nm Ag → 8 min 23 s at 40 W

40 nm Cr → 7min 45 s at 100 W

20 nm Co → 5min 50 s at 100 W, 100 nm Co → 29min 14 s at 100 W

To calibrate the SiO₂ deposition rate, I have used an Al₂O₃ substrate instead of a Si one, because the difference of densities between SiO₂ and Al₂O₃ enables a better signal when using XRR. The sputtering of SiO₂ has been performed at 200 W. As it is an insulator, it has to be deposited with RF sputtering. In order to be able to obtain a stable plasma, the Ar pressure of the main chamber has to be raised to 25 mtorr while the SiO₂ target has a power of 60 W. After the plasma strike, the pressure has to be lowered to 3 mtorr to perform the deposition, and the power increased gradually, in about 100 s, to 200 W. The sample holder is rotating in order to ensure a homogeneous deposition, and the substrate placed in the middle of the sample holder. The calibration procedure explained above has been used to determine the deposition rate of SiO₂, which turned out to be 0.0295 nm/s. Thus, to get a 10 nm layer, SiO₂ has to be deposited for 5 min 39 s.

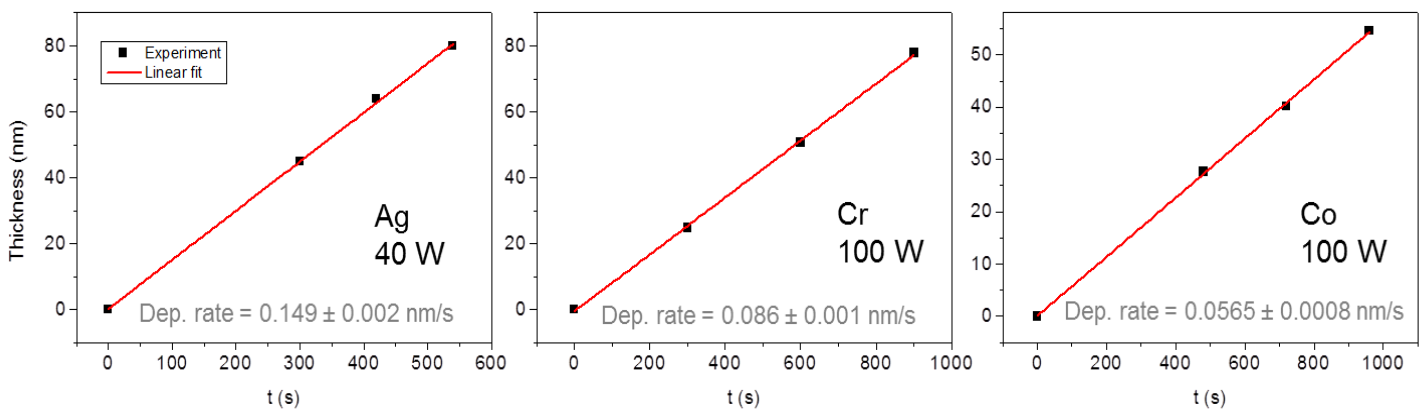


Fig. 3.3. Linear fit to determine deposition rate of Ag, Cr and Co.

3.1.2 - Thickness calibrations for the Pt wedge

In order to grow the wedge-shaped structures, the sample holder has to be motionless to obtain a gradient of thickness, as opposed to the rotating sample holder for homogeneous thickness in the entire sample that was necessary in Sec. 3.1.1 (see Fig. 3.4). Moreover, to obtain the desired gradient, the tilting of the gun containing the Pt target has to be finely adjusted. For certain degrees of inclination of the Pt gun used in tests the deposition rates have proved to be too low or the gradient of thickness of the resulting wedge structure too high for our purpose⁶. The power at which Pt has been sputtered is 40 W. I have performed two types of calibrations for the Pt wedge, a first type by means of XRR to get an estimate of the necessary inclination of the Pt gun, and a second one via spectroscopic ellipsometry to get the profile of the wedge with bigger spatial resolution.

a) Preliminary calibration of the Pt wedge via XRR

For the first type of calibrations three small chips of Si wafers have been placed on the sample holder. The chips have been placed in line at the positions that are indicated with “F”, “M” and “C” labels in Fig. 3.4, so that they are at different distances from the gun containing Pt. “F” indicates “far”, and the chip placed here will have the smaller thickness of Pt. “C” indicates “close”, so this chip will have the biggest amount of Pt. Finally, “M” is in the “middle”. I have measured by means of XRR the Pt thickness in the chips, and I have found the proper tilting of the Pt gun in order to get close to the desired 1:6 ratio. For the selected tilting, the deposition rates are the following:

“C” → 0.1 nm/s

“M” → 0.06 nm/s

“F” → 0.02 nm/s

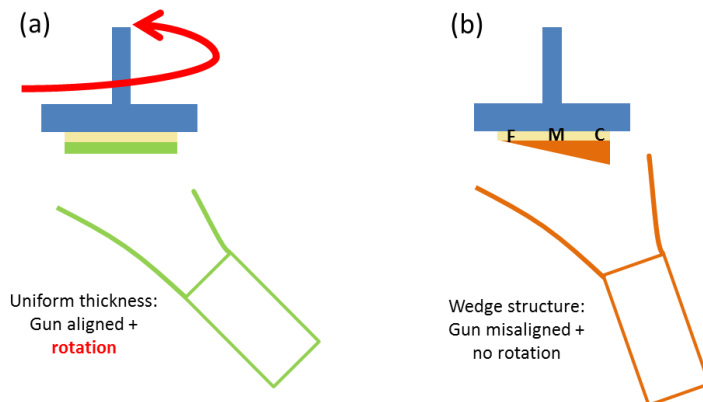


Fig. 3.4. Position of the gun and rotation of the sample holder for (a) uniform thickness samples and (b) wedge type samples. In (b) the labels “F”, “M” and “C” denote “Far”, “Middle” and “Close”, the positions on which the chips for a first calibration of the gradient of the wedge have been placed.

⁶ We want to have a ratio of about 1:6 in the Pt thickness between the end points of the strip, with thicknesses ranging from about 1 atomic layer to 6 atomic layers. It is expected that interfacial effects will no longer depend on the Pt thickness above several atomic layers.

This procedure serves us to have a first estimate in order to choose the proper tilting of the Pt gun. A second more accurate calibration has been performed by means of spectroscopic ellipsometry, in order to have a measurement of the Pt thickness along the whole strip, with a better spatial resolution.

a) Calibration of the Pt wedge profile via spectroscopic ellipsometry

For the second type of calibrations I have fabricated a Pt wedge on a 8-cm-long Si substrate strip. With the tilting of the gun selected thanks to the previous calibration and keeping the sample holder motionless, I have sputtered Pt for 150s, which based on the previous calibration would lead to a wedge of about 3 nm Pt in the thin end and about 15 nm in the thick end. Right after the Pt deposition, I have deposited a 10 nm SiO₂ layer to protect Pt from oxidation. During the deposition of SiO₂ the sample holder has to rotate to obtain a homogeneous thickness of the protective layer.

I have measured the thickness profile of this sample with spectroscopic ellipsometry. With this tool, as opposed to XRR, we can measure the thickness of the thin film at each point in an automatized way. I have measured the ellipsometric parameters and used the database of refractive indices available in the software to fit the data, thus obtaining the thickness of the Pt layer. Figure 3.5 shows the Pt thickness at each point of the calibration strip. It can also be observed that XRR data and spectroscopic ellipsometry data are consistent with each other. The left-hand side vertical axis represents the thickness of the calibration wedge, while the right-hand side corresponds to the Pt thickness of the wedges that are deposited in the Pt20A&B and Pt100A&B samples, which are 10 times thinner than the calibration wedge, with thicknesses ranging from 0.3 nm to 1.8 nm.

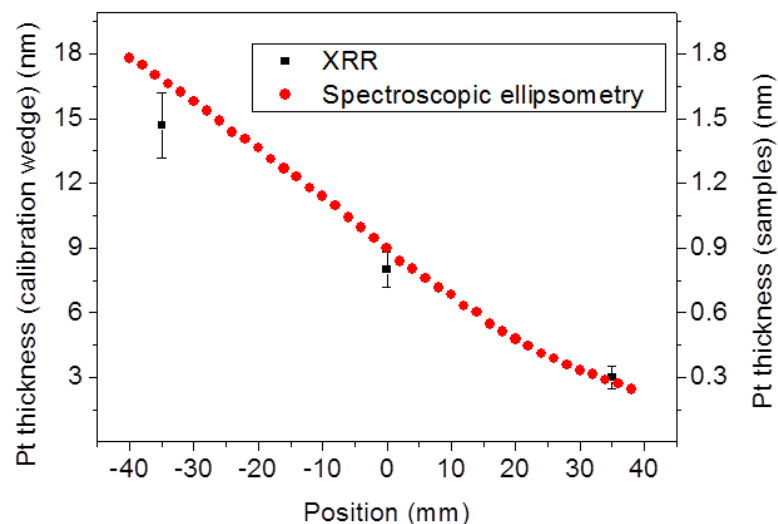


Fig. 3.5. Profile of the calibration Pt wedge. Red circles are spectroscopic ellipsometry data and black squares indicate the thickness calculated from the deposition rates measured by means of XRR in the “F”, “M” and “C” chips.

3.2- Sample fabrication

After having characterized properly all the thicknesses of the multilayer structure, I have proceeded to fabricate the samples listed at the beginning of the chapter. Figure 3.6 schematizes all the fabrication steps.

(1) First, a Si (110) wafer has to be cut into strips. This specific type of Si wafer is needed to ensure the growth of Co with the desired crystal structure and orientation. The strips have been cut in such way that, upon depositing the Ag and Cr template layers, the *c*-axis of Co, which is the magnetic easy axis, will be 15° tilted with respect to the long axis of the strip, as it is shown in the figure. We have chosen this specific orientation of the EA because in the GME setup the field will be applied perpendicular to the axis of the strip. The choice of the tilting of the EA enables to have components of the magnetization that give rise to the longitudinal and the transverse Kerr effect.

(2) After cutting the strips, the native SiO₂ of the wafer has to be removed by HF etching, so that the first template layer (Ag) can accommodate on the Si in order to achieve epitaxial growth. The HF etching is performed in a cleanroom. First the strips are immersed during 5 min in acetone, afterwards during 5 min in isopropanol and during 5 min in deionized water. Finally, the strips are immersed in 1% HF during 10 min.

Immediately after performing this treatment, two strips are placed side by side on the sample holder, because in each deposition we fabricate two sister samples at the same time (A and B). The two strips have to be introduced into the vacuum system of the sputter as soon as possible, to avoid the formation of a new oxide layer on Si. Once the sample holder with the two strips is inserted in the chamber of the sputter, the deposition is started. We flow Ar until a pressure of 25 mtorr is obtained. We then produce a plasma strike in the SiO₂ gun, with the power at the target being 60 W. After the plasma has been produced in the SiO₂ gun, the pressure of the chamber is decreased to 3 mtorr, keeping the plasma in the SiO₂ gun stable. The SiO₂ target has plasma during the entire deposition sequence, but its shutter remains closed until the very last step, when the protective layer of 10 nm SiO₂ has to be deposited⁷.

Once the pressure of the sputter chamber is 3 mtorr, we proceed to sputter first Ag, then Cr and after that Co. These three guns point towards the sample holder, which has to be rotating for the thickness to be homogeneous. The procedure is detailed in the following paragraphs.

(3) A power of 40 W is set to the Ag target and plasma is created. The Ag shutter is opened and a deposition of 8 min 23 s is carried out. When there are 2 min left of the Ag deposition, the Cr target is turned on at a power of 100 W, while its shutter remains closed, for the purpose of presputtering Cr. When the 8 min 23 s finish, the Ag shutter is closed and the power of this gun is stopped.

⁷ The deposition of the materials is done at 3 mtorr, but SiO₂ needs a plasma strike at 25 mtorr. By keeping the plasma on the SiO₂ gun on during all the deposition, we avoid increasing the pressure of the chamber while the deposition is going on and we are thus able to deposit the protective layer right after the Pt wedge, minimizing the waiting time this ultrathin overcoat is unprotected.

(4) The shutter of the Cr gun is opened for a period of 7 min 45 s. When there are two minutes left for the Cr deposition, the Co gun is turned on at 100 W for presputtering. After the deposition time of Cr is elapsed, its shutter is closed and the power of its gun stopped.

(5) The Co shutter is opened. The sputtering time of Co is 5 min 50 s for the 20 nm Co samples (Ref20A&B and Pt20A&B), or 29 min 14 s, for the 100 nm Co samples (Pt100A&B). When one minute of Co deposition remains, Pt starts to be presputtered and the power of the SiO₂ target is gradually increased to 200 W, in order to have it ready for the deposition of the protective layer. When the deposition of Co finishes, its shutter is closed and the power turned off.

(6) For the deposition of the overcoat, the rotation of the sample holder is stopped and the sample is aligned with respect to the gun of Pt, which is properly tilted (See Sec. 3.1.2) to get the desired gradient of thickness. Pt is deposited in such way during 15 s at a power of 40 W. This leads to a Pt wedge that is 10 times smaller than the calibration wedge. Right after the Pt deposition is finished, the corresponding shutter is closed and the deposition turned off. In the meantime, the power at the SiO₂ has reached 200 W, the power at which it will be deposited. Step (6) is skipped for the reference samples RefA&B.

(7) The shutter of the SiO₂ gun is immediately opened. This material is deposited during 5 min 39 s. For the SiO₂ deposition the rotation of the sample holder is switched on again to obtain a homogeneous thickness for the entire sample. When the deposition finishes, the shutter of the SiO₂ gun is closed and its RF power removed.

Finally, the Ar flow is stopped and when the pressure of the main chamber is lower than that of the load lock chamber the sample is extracted.

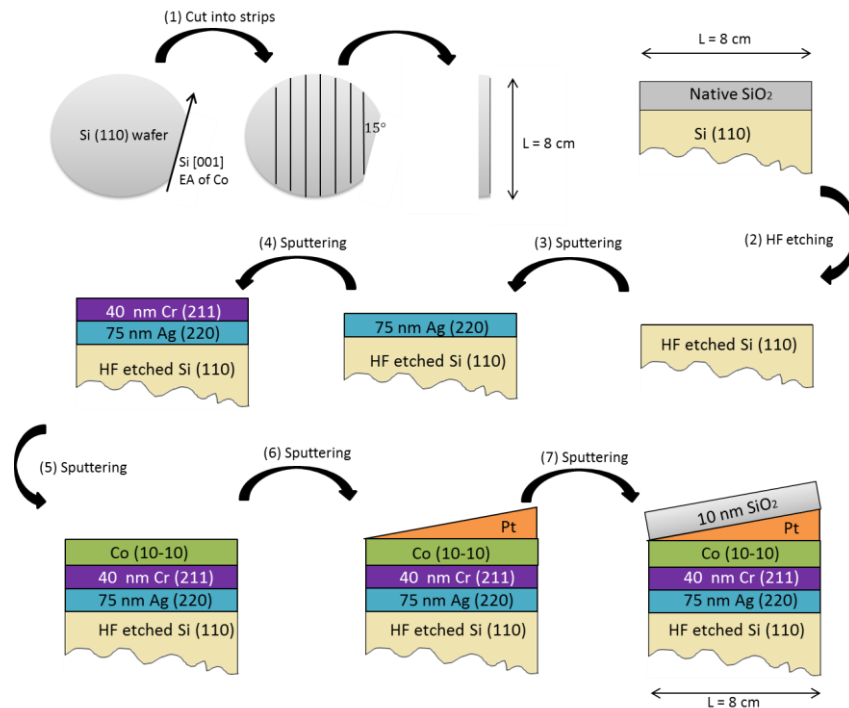


Fig. 3.6. Sample fabrication process. The steps are explained in the main text.

3.3- Crystallographic characterization. Epitaxy

Discussing the structural characterization of our samples by means of XRD will allow me to explain more easily the relations that hold between the substrate, the template layers and the Co layer, which in combination give rise to the type of crystallinity that is desired. I will thus be able to justify the growth sequence that I have followed.

X-ray diffractometry measurements have been performed on each sample in order to determine whether the desired crystalline structure has been achieved. Figure 3.7 shows the XRD $\theta - 2\theta$ scans of Pt100B, Pt20B and Ref20B. The peaks have been indexed using the available software. We identify the peaks of Co ($10\bar{1}0$), Si (220), Ag (220), Cr(211) and Co ($20\bar{2}0$). This scan serves us to check that, indeed, the Co has grown with the appropriate direction perpendicular to the sample surface, and that consequently the c -axis is in plane.

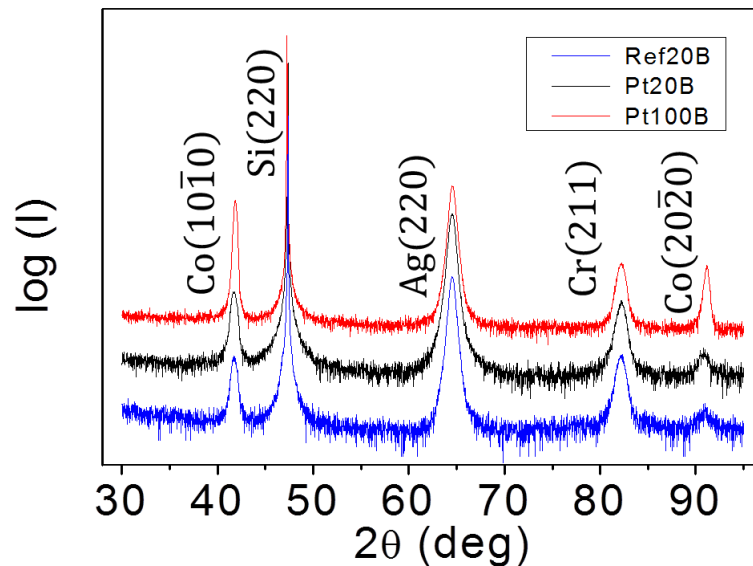


Fig. 3.7. $\theta - 2\theta$ scan of Ref20B (blue), Pt20B (black) and Pt100B (red) samples. The peaks of the identified phases are labeled.

One has to take into account that with $\theta - 2\theta$ scans one only probes the reciprocal lattice vectors perpendicular to the sample surface [24]. The diffraction peaks that are achieved and are shown in Fig. 3.7 are not a complete proof to ensure that the growth of the layers has been epitaxial. Instead, these materials could grow in these specific directions perpendicular to the sample surface not because of the matching between each material and the one deposited below, but simply because these structures are favored. In such case, the grains would not have a defined orientation in the plane of the sample. However, if the growth is epitaxial, the relations between the in-plane orientations of the crystallites of subsequent layers are fixed. To confirm that the growth is epitaxial, I have performed φ -scans by tilting the plane of the sample by an angle ψ , in order to be able to probe reciprocal lattice vectors that are not perpendicular to the surface of the sample.

For this task, I have performed four different φ -scans, for Si, Ag, Cr and Co. I have chosen different ψ angles for each material. For Si, I have tilted the sample to $\psi = 44.34^\circ$, and I have set $2\theta = 69.05^\circ$. Thus, the reciprocal lattice vector we are sensitive to is (400). I have performed a 360° scan of the φ angle. Given the crystal structure of Si, a diffraction peak should only occur twice in the full scan, with an 180° difference in position. For Ag the selected ψ has been 45° and $2\theta = 44.30^\circ$, enabling sensitivity to the (200) vector. By scanning φ two peaks are obtained, in the same position as the Si peaks. For Cr $\psi = 29.73^\circ$ and $2\theta = 44.46^\circ$, so that the diffraction peak that will be detected corresponds to the (110) plane. By scanning φ two peaks appear, at angles that are 90° shifted with respect to the position of the Si and the Ag peaks. Finally, for Co $\psi = 27.74^\circ$ and $2\theta = 47.47^\circ$ and we are sensitive to the $(10\bar{1}1)$ plane. The φ -scan shows two peaks at the same positions as the Cr peaks, 90° shifted with respect to Si and Ag. These relationships are shown in Fig. 3.8. The fact that these peaks appear and that they are aligned this way is indicative of the epitaxial growth [34].

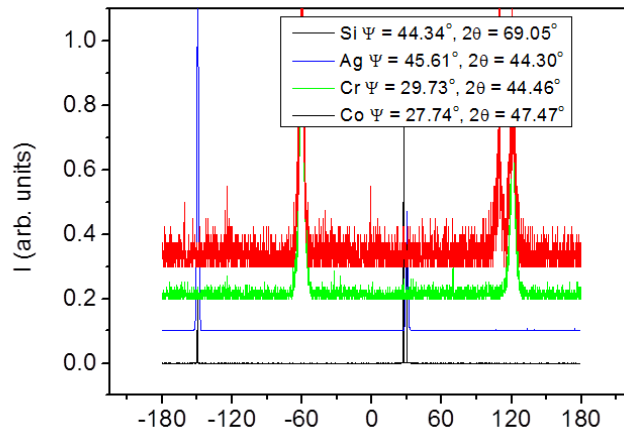


Fig. 3.8. φ -scan of Ref20B sample.

Figure 3.9 shows the epitaxial relation of the layers based on the bulk lattices of the materials [21,34]. The dimensions of the surface unit cells and the crystallographic directions are shown in the figure. As a summary of Fig. 3.9 we can say that Si, which exhibits a face-centered diamond cubic crystal structure, has a (110) crystallographic plane with a rectangular cell. Ag has also fcc structure and the surface unit cell of its (110) orientation is a rectangle. According to the dimensions of the surface unit cells of Si and Ag in the (110) orientation, a 2×4 Ag (110) [001] supercell mesh matches almost perfectly to half a 3×3 Si (110) [001] supercell mesh. Cr has a bcc structure and also shows a rectangular surface unit cell in the (211) direction, which can grow on top of the one of Ag. Cr grows onto Ag (110) [001]. Finally, the Cr (211) surface is an excellent template for hcp Co, which grows with its [0001] direction (the easy axis) aligned with the [110] direction of the Cr (211) surface. So in the end the EA of Co is aligned with the [001] direction of Si. Actually, the wafer is not completely round, as it may be seen in the first picture in Fig. 3.6. The cut it has, which is called the primary flat, indicates the [001] direction. Once the Co is grown epitaxially following the indicated sequence, its magnetic EA will be parallel to the primary flat. The primary flat has served as an indicator to cut the strips.

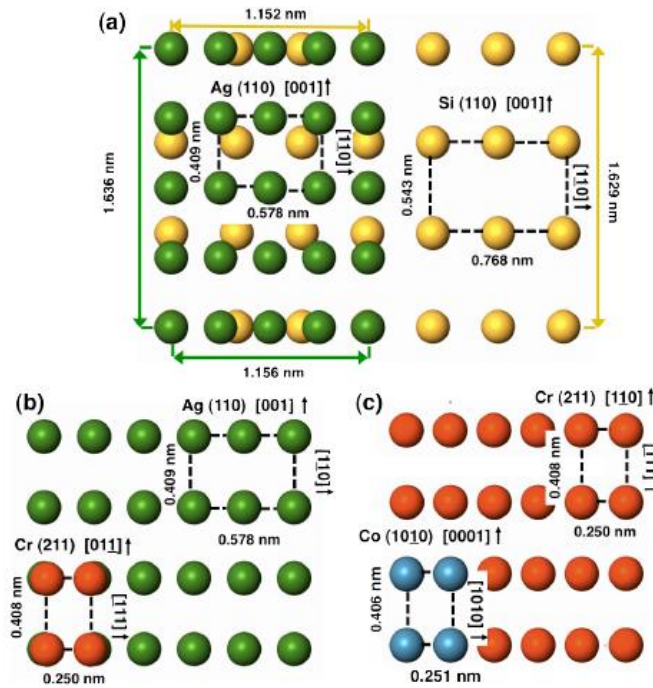


Fig. 3.9. Display of the epitaxial relations between subsequent layers in the stacking sequence $\text{Si}(110)[001]/\text{Ag}(110)[001]/\text{Cr}(211)[0\bar{1}1]/\text{Co}(10\bar{1}0)[0001]$ by means of their respective crystallographic surface unit cells. (a) shows the epitaxy relation of $\text{Si}(110)[001]/\text{Ag}(110)[001]$, (b) of $\text{Ag}(110)[001]/\text{Cr}(211)[0\bar{1}1]$ and (c) of $\text{Cr}(211)[0\bar{1}1]/\text{Co}(10\bar{1}0)[0001]$ [21].

Another thing that should be pointed out is the lack of diffraction peaks corresponding to Pt in the XRD scans. One reason could be that the thickness of the Pt overcoat is too thin to see any epitaxy. However, based on the dimensions of the cells and the lack of reports of epitaxy we believe that epitaxial overcoat growth is unlikely.

To sum up, I have fabricated $\text{Co}(10\bar{1}0)$ films with in-plane easy axis by means of epitaxial growth on macroscopic strips. The crystal structure of the samples has been confirmed by means of XRD. Additionally, I have successfully grown a wedge-shaped Pt overcoat of thicknesses ranging from 0.3 nm to 1.8 nm along the strip, for which I have carefully designed and followed the fabrication step, including calibrations of the wedge.

Chapter 4

GENERALIZED MAGNETO-OPTICAL ELLIPSOMETRY

RESULTS

The magnetic and magneto-optical characterization of our three samples has been performed via GME measurements. The samples have been placed in an automatized linear motion stage, which enables us to control and vary in an automatic way the point of the sample on which the laser of the GME is hitting, i.e., the measurement point. Figure 4.1 represents schematically the measurement configuration. The strip-type sample is placed perpendicular to the applied field. The EA (c -axis, green dashed line) is tilted by 15° from the vertical (x -axis). The angle of the magnetization (orange arrow) with the x -axis is called ϕ . The piece of the sample that is illuminated by the laser (red spot in Fig. 4.1) is the one that is placed in between the poles of the electromagnet, and it is this subsample that is measured by means of a complete GME measurement set. The linear stage moves (1 or 2 mm) after the measurement at a given point is finished, so that a different part of the strip is placed between the poles and is hit by the laser. The samples that have been measured with in this way are Pt20B (20 nm Co with Pt overcoat wedge), Pt100B (100 nm Co with Pt overcoat wedge) and as reference, Ref20B (20 nm Co without Pt overcoat).

I have aligned the setup before measuring the samples. All the optical elements and the linear motion stage have to be aligned, so that the plane of incidence is perpendicular to the axis of the strip sample. To ensure this, I have tested that upon moving the linear motion stage the reflected laser spot always follows the same path. Additionally, I have optimized the intensity at the detector. After ensuring that the experimental conditions are stable, I have proceeded to measure $\frac{\delta I}{I}(\theta_1, \theta_2)$ maps at different positions of the macroscopic strip sample. In the Pt20B and Pt100B samples, the different positions on the strip correspond to different Pt overcoat thicknesses. In sample Ref20B, the measured quantities should be independent of the measurement position. If this were not the case, point to point changes in the Pt20B and Pt100B measurements could be due to a nonuniform fabrication, and not to an overcoat-induced effect. After the measurements, a multiparameter least-squares fit of the measured maps to Eq. (2.12) enables us to obtain the fitting parameters that are related to the reflection matrix of the sample.

In this chapter, I will first discuss the quality of the data and perform a qualitative analysis of the data. For this purpose I will focus on a given measurement point (position -19.5 mm of sample Pt20B, which has 1.36 nm of Pt overcoat). This point is representative and

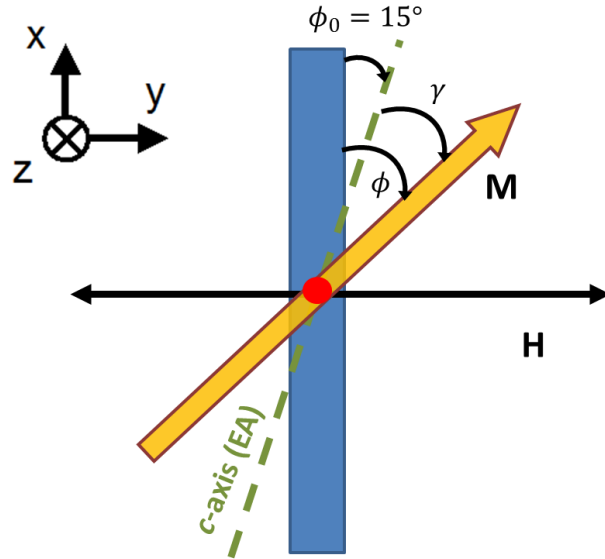


Fig. 4.1. Measurement configuration. The sample (blue rectangle) is aligned perpendicular to the applied field, which is depicted as a black line and is contained in the plane of incidence of the light. The *c*-axis of Co, i.e., the easy axis of the magnetization, is 15° away from the main axis of the sample. The magnetization is represented by an orange arrow, and the angle it forms with the main axis of the sample is called ϕ . γ is the angle between the EA and the magnetization. The red spot on the sample symbolizes the laser spot, indicating the measurement point in the GME experiment.

shows the features displayed by the rest of measurements. After that, I will show a set of measurements and point out an apparent inconsistency of the data with the assumed model of a homogeneous magnetization rotating upon applying a field. I will then explain magneto-optical anisotropy (MOA) and show how its inclusion can consistently explain our data. I will then show how MOA is enhanced by the Pt overcoat layer, and how this enhancement is affected by the Pt thickness. Finally, I will discuss the effect of the Pt overcoat on the magnetocrystalline anisotropy (MCA).

4.1 - Data quality

As a representative measurement, I have selected the one performed on sample Pt20B, at the location where it has 1.36 nm of Pt overcoat thickness. The maps measured via GME in this subsample have been fitted with Eq. (2.12). Figure 4.2 shows $\frac{\delta I}{I}(\theta_1, \theta_2)$ maps for four different values of the applied field, namely the maximum field strengths that are achieved ($H = \pm 1650$ Oe), an intermediate value ($H = 875$ Oe) and the remanence state ($H = 0$ Oe). The left column shows the measured maps and the middle column shows the maps obtained by least-squares fits of Eq. (2.12). As it can be observed, both maps for each field value are virtually identical and the R^2 values of the least-squares fits are very good. Moreover, in the third column, we observe that the difference between the measured and the fitted values are caused by randomly distributed noise (white noise).

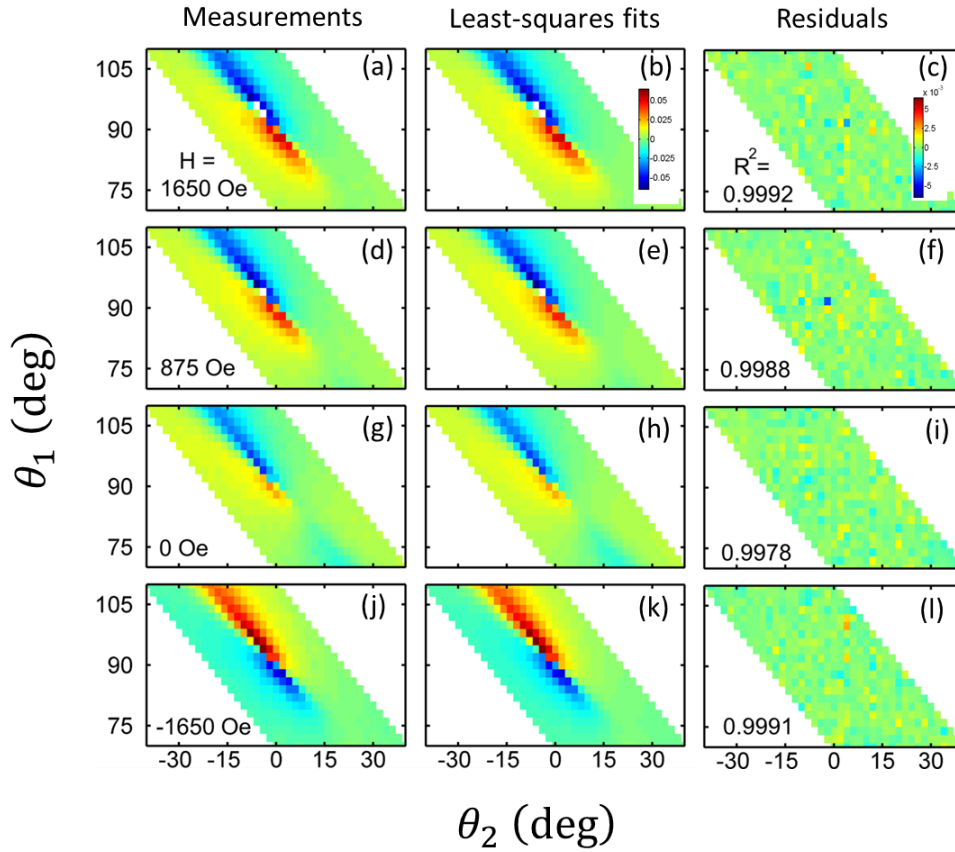


Fig. 4.2. Comparison between measured (left column) and fitted (middle column) $\frac{\delta I}{I}$ maps for different values of the applied field. The right column shows the residuals of the least-squares fits. The color bar for the left and middle columns is placed on (b), the one for the right column on (c).

It should be pointed out that the quality of the fits is decreased when the magnetization is near the switching point, i.e., in the vicinity of H_c , because in this field regime the sample can form a non-uniform magnetization state and the description of the experiment by a single reflection matrix is not as good as for truly uniform magnetization states. This can be observed in Fig. 4.3, where the R^2 of the fit is plotted as a function of the applied magnetic field for the decreasing field branch. In the main figure we can see a sudden decrease of the quality of the fit at the $H = -300$ Oe, where the magnetization switches. In the inset, we can see that this decrease actually starts in a gradual way but still, the R^2 values are very close to 1 until the immediate vicinity of the coercive field.

4.2 - Qualitative data from least-squares fitting of $\frac{\delta I}{I}$ maps

The fit of the data to Eq. (2.12) enables the extraction of the six B_i parameters for each value of the field, the corrections for the polarizer angles θ_1^0 and θ_2^0 , and I_0 . Figure 4.4 shows the B_i parameters as a function of the field for the selected sample we are discussing here. It has to be pointed out that these parameters have been extracted for the decreasing

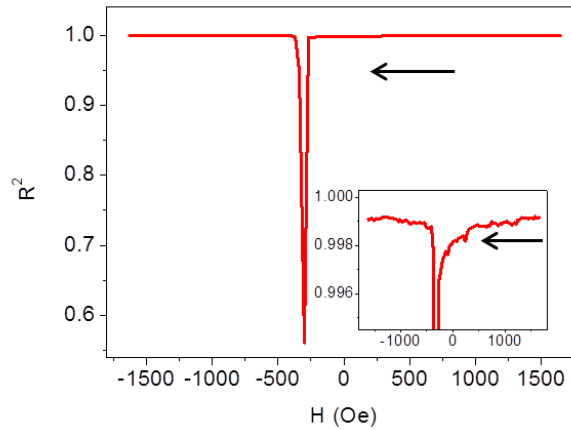


Fig. 4.3. R^2 values as a function of the applied field H . The arrow indicates the direction in which the field changes (decreasing field branch). Inset: zoom around the highest R^2 values.

field branch. There are some relevant observations that can be made in Fig. 4.4:

- The shape of B_1 to B_4 is reminiscent of that of the decreasing branch of hysteresis loops (see, for instance, Fig 2.9). This is because these parameters depend on the magnetically induced elements of the reflection matrix in equation (2.9), namely α and β , and they change sign when the magnetization switches, at about $H = -300$ Oe.
- As the absolute value of the field increases, B_1 and B_2 also increase in absolute value. However, the absolute value of B_3 and B_4 decreases as the field gets larger. To understand this, we have to remember from Sec. 2.3.2 that B_1 and B_2 are related to the longitudinal magnetization, i.e., the magnetization component contained in the sample plane and in the plane of incidence (so, in our measurement configuration, along the axis of the applied magnetic field). Assuming a pure rotation of the magnetization, the Zeeman energy favors the alignment of the magnetization with the magnetic field and thus there is an increase of the magnetization component along its axis, and consequently of B_1 and B_2 as the field strength increases. On the other hand, as B_3 and B_4 are related to the transverse magnetization, i.e., the component which is perpendicular to the plane of incidence, their absolute value decrease when the absolute value of the magnetic field is increased.
- B_5 and B_6 show no field dependence within the error bars, as can be seen in the insets of the corresponding figures. Overall, we see that only the point at which R^2 decreases dramatically deviates from this field-independent characteristic. This is the expected behavior, because B_5 and B_6 only depend on the optical constants.

The other three fitting parameters, namely I_0 , θ_1^0 and θ_2^0 are displayed in Fig. 4.5. The full-scale graphs show a spike-like feature due to the points where R^2 deviates significantly from 1. The corresponding zooms show a very minor field dependence of the parameters.

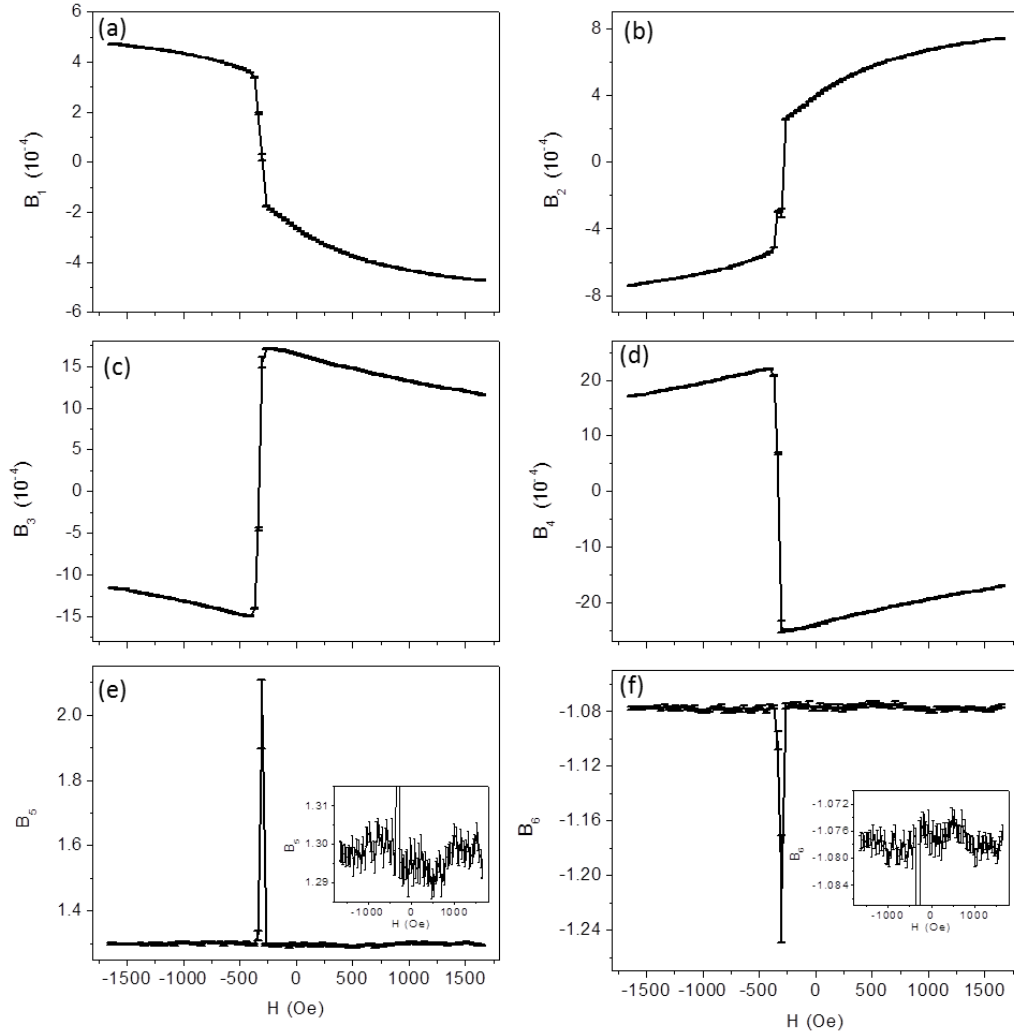


Fig. 4.4. B_1 to B_6 parameters vs. the magnetic field strength H . The error bars are hardly visible because the error is very small compared with the scale of the variation of the parameters.

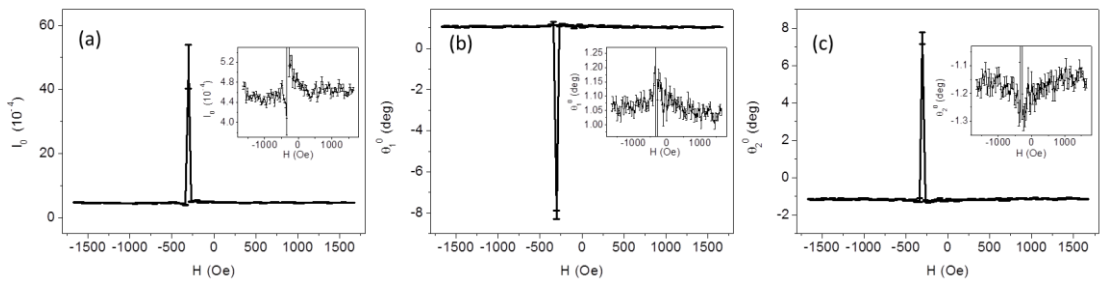


Fig. 4.5. I_0 , θ_1^0 and θ_2^0 parameters.

Moreover, the size of I_0 is small in comparison to the other terms of the denominator in Eq. 2.12, and the corrections of the polarizers are of the order of 1° . The corrections of the polarizers are due to the fact that one cannot align them by eye with respect to a plane of incidence that is not visible.

4.3- Quantitative analysis of the data

4.3.1- Pure rotation of magnetization without magneto-optical anisotropy

In order to achieve a quantitative analysis, we have studied the data from the highest applied field to remanence, where the magnetization is homogeneous and the description of the sample by the reflection matrix in Eq. (2.6) is accurate. In this field range we can assume that the magnetization of our samples undergoes a pure rotation, so that upon applying a magnetic field the angle ϕ in Fig. 4.1 changes. In this field range the pure rotation assumption is confirmed by means of VSM measurements (Chapter 5), where the measured data are in very good agreement with the Stoner-Wohlfarth model, which assumes a homogeneous magnetization that rotates upon applying a magnetic field from saturation to remanence.

Another assumption we have made in a first step is that the system displays no magneto-optical anisotropy (MOA), so that the magneto-optical coupling constant Q is independent from the magnetization direction. With these two assumptions, B_1 and B_2 have to be proportional to $\sin(\phi)$, because they are related to the longitudinal magnetization, i.e., along the y -axis in Fig. 4.1. B_3 and B_4 , which are related to the transverse magnetization, i.e., along the x -axis in Fig. 4.1, have to be proportional to $\cos(\phi)$. The proportionality constants are independent of the magnetic state, so that, within this model, the expected values (which we denote with a bar) of B_1 to B_4 normalized to their remanence values follow the relations

$$\overline{NB}_1 = \frac{\overline{B}_1(H)}{B_1(H=0)} = \overline{NB}_2 = \frac{\overline{B}_2(H)}{B_2(H=0)} = \frac{\sin(\phi)}{\sin(\phi_0)} \quad (4.1.a)$$

$$\overline{NB}_3 = \frac{\overline{B}_3(H)}{B_3(H=0)} = \overline{NB}_4 = \frac{\overline{B}_4(H)}{B_4(H=0)} = \frac{\cos(\phi)}{\cos(\phi_0)}, \quad (4.1.b)$$

because for $H = 0$ the magnetization lies along the EA, which is at an angle $\phi = \phi_0$, fixed in our experiment to 15° .

Each magnetic field value H determines a corresponding magnetization angle ϕ , which has to describe consistently the four measured data sets of the normalized B_i , $i = 1,4$. To obtain $\phi(H)$ we minimize numerically the $\chi^2(H)$ function

$$\chi^2(H) = \left(\frac{B_1(H)}{B_1(H=0)} - \overline{NB}_1 \right)^2 + \left(\frac{B_2(H)}{B_2(H=0)} - \overline{NB}_2 \right)^2 + \left(\frac{B_3(H)}{B_3(H=0)} - \overline{NB}_3 \right)^2 + \left(\frac{B_4(H)}{B_4(H=0)} - \overline{NB}_4 \right)^2. \quad (4.2)$$

Hereby, the number of experimental data is $4n$ (where n is the number of applied fields for which the normalized B_i 's are analyzed), and the number of fitting parameters ϕ is n . With the fitted values of ϕ , we can calculate the expected \overline{NB}_i , $i = 1,4$.

Figure 4.6 shows the four normalized experimental quantities with filled symbols. The red line represents the expected values from the fitted ϕ 's. As it may be observed, according to the assumed model, the experimental NB_1 and NB_2 should be identical, as well as NB_3 and NB_4 . However, this is not the case. Moreover, the fit is inconsistent with the data: the decrease of NB_3 and NB_4 upon increasing the field strength is not compensated by a sufficiently large increase of NB_1 and NB_2 . As the fitted values show, the model we have assumed leads to a smaller decrease of NB_3 and NB_4 . This model clearly fails to explain the behavior of our samples, so that further refinement has to be incorporated to the model.

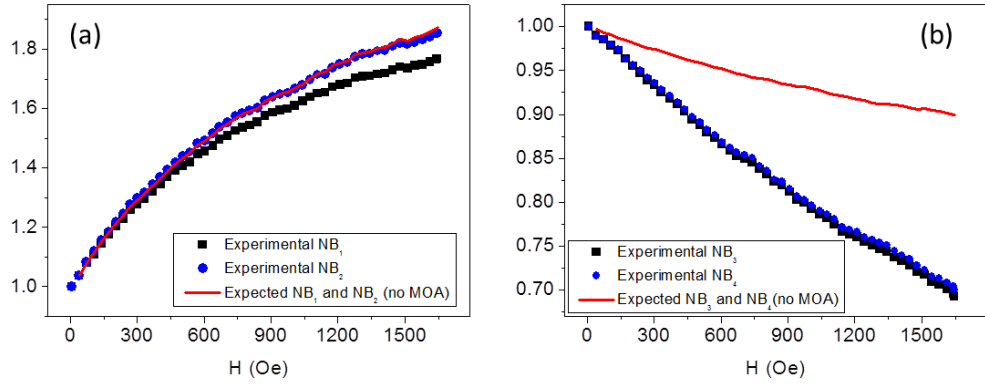


Fig. 4.6. B_1 and B_2 (a), and B_3 and B_4 (b) normalized to their remanence value from the maximum applied field to remanence in the decreasing field branch. Data have been obtained from the measurements on the subsample of Pt20B with 1.36 nm thick Pt overcoat. Black squares and blue circles represent experimental values. The red lines represent the fitted values assuming pure rotation of the magnetization and no magneto-optical anisotropy.

4.3.2- Pure rotation of magnetization with magneto-optical anisotropy

The first thing one might question is whether the magnetization is indeed homogeneous and undergoes a pure rotation. Nevertheless, this assumption is well confirmed by means of our VSM measurements in Chapter 5. Additionally, we see in Fig. 4.6 that the deviation of the data from the pure rotation model without magneto-optical anisotropy (red line) is bigger for high field values. However, it is precisely at high field values where the pure rotation of the magnetization is a better assumption. As a consequence, we stick to the assumption of pure magnetization rotation.

However, the other assumption in Sec. 4.3.1, namely that the samples are magneto-optically isotropic, has to be abandoned. Indeed, a recent study [11] has addressed that the level of MOA in Co ($10\bar{1}0$) films is very substantial. I will now show that the inclusion of MOA leads to a consistent interpretation of our results.

a) Implications of magneto-optical anisotropy in the B_1 , B_2 , B_3 and B_4 parameters

MOA is a phenomenon that arises from the fact that the properties of a crystalline material depend on the direction. One of these properties that depend on the crystal lattice is the magneto-optical coupling. In Sec. 4.3.1 and also in Sec. 2.3.2, where I have presented the GME technique, the magneto-optical coupling has been taken as a constant, Q . Nevertheless, this quantity is in reality a tensor. In the case of having hcp Co (uniaxial) this tensor is defined by only two quantities, namely Q_{\parallel} , the magneto-optical coupling along the c -axis, and Q_{\perp} , the one perpendicular to the c -axis. The fact that these two couplings are different leads to a mixture between the longitudinal and transverse components of the magnetization. As a consequence, the GME parameters B_1 , B_2 , B_3 and B_4 cannot be interpreted as to be following the rotation of the magnetization as in Sec. 4.3.1.

I have derived analytically the form of the B_i ($i = 1,4$) parameters for a magneto-optically anisotropic and optically isotropic system with in-plane magnetization and uniaxial symmetry in Appendix A. Here, I will just present the basic ideas and the final result.

Let us suppose that we have a magneto-optically anisotropic uniaxial medium with in-plane magnetization and the EA aligned with the x -axis in Fig. 4.1 ($\phi_0 = 0^\circ$). The dielectric tensor would be

$$\bar{\epsilon} = \epsilon \begin{pmatrix} 1 & 0 & iQ_{\perp}m_{\perp} \\ 0 & 1 & -iQ_{\parallel}m_{\parallel} \\ -iQ_{\perp}m_{\perp} & iQ_{\parallel}m_{\parallel} & 1 \end{pmatrix} \quad (4.3)$$

with $m_{\perp} = \cos(\phi - \phi_0)$ and $m_{\parallel} = \sin(\phi - \phi_0)$. For a general orientation of the EA, $\phi_0 \neq 0$, the tensor (4.3) has to be rotated. This rotation leads to a mixture of the m_{\perp} and m_{\parallel} terms in the elements of the rotated dielectric tensor (See Eqs. (A.3.a-c)). If $Q_{\parallel} = Q_{\perp}$, the elements of the matrix will only have either transverse or longitudinal magnetization, not a mixture of both.

One can solve Maxwell's equations with the appropriate boundary conditions for a medium with the dielectric tensor (A.3.a) and get the reflection matrix [29]. From the reflection matrix and the relations (2.14.a-f) one can get the GME B_i ($i = 1,4$) parameters. In Appendix A I show that the B_i parameters normalized to their remanence value can be written as in Eqs. (4.4)-(4.7) with the definitions:

$N = n + i\kappa$, the refractive index of the magnetic medium

$\cos \Omega_1 = c + id$, where Ω_1 is the refraction angle inside the magnetic medium

Ω_0 is the incident angle, which in our case is 45° .

$Q_{\perp}^{(r)}$ and $Q_{\perp}^{(i)}$ are the real and imaginary parts of Q_{\perp} , and $Q_{\parallel}^{(r)}$ and $Q_{\parallel}^{(i)}$ are the real and imaginary parts of Q_{\parallel} .

$$\overline{NB}_1 = \frac{\sin(\phi - \Delta_1)}{\sin(\phi_0 - \Delta_1)} \quad \Delta_1 = \text{atan}\left(-\frac{c_1}{d_1}\right) \quad (4.4.a)$$

$$C_1 = \left[F_1 \left(Q_{\perp}^{(i)} - Q_{\parallel}^{(i)} \right) - \tilde{F}_1 \left(Q_{\perp}^{(r)} - Q_{\parallel}^{(r)} \right) \right] \sin \phi_0 \cos \phi_0 \quad (4.4.b)$$

$$D_1 = -F_1 \left(Q_{\perp}^{(i)} \cos^2 \phi_0 + Q_{\parallel}^{(i)} \sin^2 \phi_0 \right) + \tilde{F}_1 \left(Q_{\perp}^{(r)} \cos^2 \phi_0 + Q_{\parallel}^{(r)} \sin^2 \phi_0 \right) \quad (4.4.c)$$

$$F_1 = c[n \cos^2 \Omega_0 + \cos \Omega_0 (n^2 c - n\kappa d - c) - (nd + \kappa c)(\kappa \cos \Omega_0 - d) - nc^2 + \kappa cd] - d[(nd + \kappa c)(n \cos \Omega_0 - c) + (\kappa \cos \Omega_0 - d)(\cos \Omega_0 + nc - \kappa d)] \quad (4.4.d)$$

$$\tilde{F}_1 = d[n \cos^2 \Omega_0 + \cos \Omega_0 (n^2 c - n\kappa d - c) - (nd + \kappa c)(\kappa \cos \Omega_0 - d) - nc^2 + \kappa cd] + c[(nd + \kappa c)(n \cos \Omega_0 - c) + (\kappa \cos \Omega_0 - d)(\cos \Omega_0 + nc - \kappa d)] \quad (4.4.e)$$

$$\overline{NB}_2 = \frac{\sin(\phi - \Delta_2)}{\sin(\phi_0 - \Delta_2)} \quad \Delta_2 = \text{atan}\left(-\frac{c_2}{D_2}\right) \quad (4.5.a)$$

$$C_2 = \left[-F_2(Q_{\perp}^{(i)} - Q_{\parallel}^{(i)}) - \tilde{F}_2(Q_{\perp}^{(r)} - Q_{\parallel}^{(r)})\right] \sin \phi_0 \cos \phi_0 \quad (4.5.b)$$

$$D_2 = F_2(Q_{\perp}^{(i)} \cos^2 \phi_0 + Q_{\parallel}^{(i)} \sin^2 \phi_0) + \tilde{F}_2(Q_{\perp}^{(r)} \cos^2 \phi_0 + Q_{\parallel}^{(r)} \sin^2 \phi_0) \quad (4.5.c)$$

$$F_2 = -F_1(T_1 T_3 + T_2 T_4) + \tilde{F}_1(T_2 T_3 - T_1 T_4) \quad (4.5.d)$$

$$\tilde{F}_2 = F_1(T_2 T_3 - T_1 T_4) + \tilde{F}_1(T_1 T_3 + T_2 T_4) \quad (4.5.e)$$

$$T_1 = n(\cos^2 \Omega_0 - c^2 + d^2) + 2\kappa cd + c \cos \Omega_0 (1 - n^2 + \kappa^2) + 2n\kappa d \cos \Omega_0 \quad (4.5.f)$$

$$T_2 = \kappa \cos^2 \Omega_0 - \kappa(c^2 - d^2) - 2ncd + d(1 - n^2 + \kappa^2) - 2n\kappa c \quad (4.5.g)$$

$$T_3 = n(\cos^2 \Omega_0 - c^2 + d^2) + 2\kappa cd - c \cos \Omega_0 (1 - n^2 + \kappa^2) - 2n\kappa d \cos \Omega_0 \quad (4.5.h)$$

$$T_4 = \kappa \cos^2 \Omega_0 - \kappa(c^2 - d^2) - 2ncd - d(1 - n^2 + \kappa^2) + 2n\kappa c \quad (4.5.i)$$

$$\overline{NB}_3 = \frac{\cos(\phi - \Delta'_3)}{\cos(\phi_0 - \Delta'_3)} \quad \Delta'_3 = \text{atan}\left(\frac{D_3}{c_3}\right) \quad (4.6.a)$$

$$C_3 = F_3(Q_{\perp}^{(i)} \sin^2 \phi_0 + Q_{\parallel}^{(i)} \cos^2 \phi_0) - \tilde{F}_3(Q_{\perp}^{(r)} \sin^2 \phi_0 + Q_{\parallel}^{(r)} \cos^2 \phi_0) \quad (4.6.b)$$

$$D_3 = \left[-F_3(Q_{\perp}^{(i)} - Q_{\parallel}^{(i)}) + \tilde{F}_3(Q_{\perp}^{(r)} - Q_{\parallel}^{(r)})\right] \sin \phi_0 \cos \phi_0 \quad (4.6.c)$$

$$F_3 = n \cos \Omega_0 - c \quad (4.6.d)$$

$$\tilde{F}_3 = \kappa \cos \Omega_0 - d \quad (4.6.e)$$

$$\overline{NB}_4 = \frac{\cos(\phi - \Delta'_4)}{\cos(\phi_0 - \Delta'_4)} \quad \Delta'_4 = \text{atan}\left(\frac{D_4}{c_4}\right) \quad (4.7.a)$$

$$C_4 = -F_4(Q_{\perp}^{(i)} \sin^2 \phi_0 + Q_{\parallel}^{(i)} \cos^2 \phi_0) - \tilde{F}_4(Q_{\perp}^{(r)} \sin^2 \phi_0 + Q_{\parallel}^{(r)} \cos^2 \phi_0) \quad (4.7.b)$$

$$D_4 = \left[F_4(Q_{\perp}^{(i)} - Q_{\parallel}^{(i)}) + \tilde{F}_4(Q_{\perp}^{(r)} - Q_{\parallel}^{(r)})\right] \sin \phi_0 \cos \phi_0 \quad (4.7.c)$$

$$F_4 = -F_3(T_1 T_3 + T_2 T_4) + \tilde{F}_3(T_2 T_3 - T_1 T_4) \quad (4.7.d)$$

$$\tilde{F}_4 = F_3(T_2 T_3 - T_1 T_4) + \tilde{F}_3(T_1 T_3 + T_2 T_4) \quad (4.7.e)$$

MOA thus introduces four different phase shifts for each of the \overline{NB}_i ($i = 1,4$) parameters. By looking at the equations, one can note that these phase shifts vanish if $Q_{\parallel} = Q_{\perp}$ (See Appendix A).

b) Simulations with the transfer-matrix method including MOA

The analytic derivation of the B_i parameters with MOA assumes a bulk material. However, our samples are thin films that have a SiO_2 protective layer. These facts do not alter the form of \overline{NB}_i , and equations (4.4.a), (4.5.a), (4.6.a) and (4.7.a) still hold. To demonstrate that the fundamental form of the equations is not altered, I have performed numerical simulations that use the transfer-matrix method [36,37] to calculate the GME parameters. This approach enables us to calculate the reflection matrix of a multilayer system, formed of materials with different optical and magneto-optical properties. In the model I have used, I have included a 10 nm thick amorphous SiO_2 layer, a 20 nm thick uniaxial Co layer with MOA, and finally an optically isotropic Cr substrate, because the light penetration depth at $\lambda = 635$ nm is significantly smaller than the combined thickness of Co and Cr layers. The values of the parameters that have been chosen for the calculation are the ones that have been reported for Co in the literature. $n = 2.22$, $\kappa = 4.17$, [38] and $Q_{\parallel} = 0.03 - 0.01i$, a value that is typically measured in the kind of samples we have. Q_{\perp} is a constant times Q_{\parallel} , $Q_{\perp} = \sigma Q_{\parallel}$, with $\sigma \in \mathbb{C}$. For the SiO_2 layer, $\varepsilon = 2.1316$ [38]. For Cr, $n_{Cr} = 3.55$, $\kappa_{Cr} = 4.27$ [38].

In Fig. 4.7 we can see the simulated B_i , $i = 1, 4$ values, normalized to the remanence value, as a function of the magnetization angle ϕ , for two different values of σ , namely $\sigma = 1$, (no MOA), and $\sigma = 1.2 - 0.3i$. For $\sigma = 1$, the case without MOA, represented in black lines in Fig. 4.7, $NB_1 = NB_2$ and $NB_3 = NB_4$ ⁸. For $\phi = 0$, $NB_1 = NB_2 = 0$ and $NB_3 = NB_4$ have their maximum, because the magnetization lies along the x -axis. For $\phi = \pm 90^\circ$ the opposite happens, $NB_1 = NB_2$ are maximal and $NB_3 = NB_4$ are zero, because the magnetization is along the y -axis. When MOA is included, NB_1 and NB_2 are no longer identical, as it can be seen in the blue and red curves in Fig. 4.7(a), and neither are NB_3 and NB_4 . The curves including MOA have a phase shift with respect to those without MOA. For $\phi = 0^\circ$, NB_1 and NB_2 , which are related to the longitudinal Kerr effect, are different from zero even if the magnetization is completely transverse. Concomitantly, for $\phi = \pm 90^\circ$, when the magnetization is completely longitudinal, NB_3 and NB_4 are not zero, even if they are related to the transverse Kerr effect. This arises because of the mixture of the longitudinal and transverse magnetizations that is a consequence of MOA. Another thing that is worth to point out is that, before normalizing the B_i 's to their remanence value, B_1 and B_2 on the one hand, and B_3 and B_4 on the other hand, take the same value for any value of σ at $\phi = 15^\circ$ and $\phi = 15^\circ - 180^\circ$. This is the case because, for this particular angle of the magnetization, the magnetization lies along the EA we are only sensitive to Q_{\parallel} . If we look at Eqs. (A.3 b-c), when $\phi = 15^\circ$ or $15^\circ - 180^\circ$, ε_{13} and ε_{23} depend on Q_{\parallel} but not on Q_{\perp} , so that the values are independent of σ .

⁸ In fact, this is true for any real value of σ , as it is shown in Appendix A. It can be deduced from the set of equations (4.4), (4.5), (4.6) and (4.7).

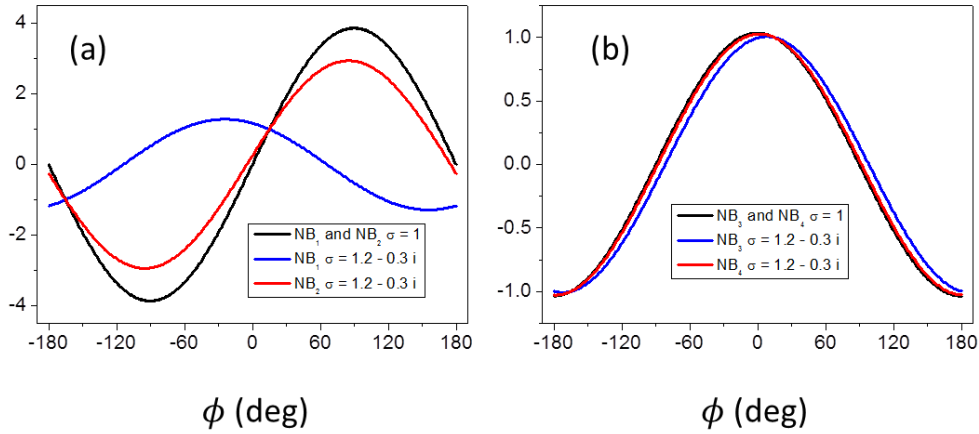


Fig. 4.7. Simulated values of NB_1 and NB_2 in (a), and of NB_3 and NB_4 in (b), for two different values of σ , namely, $\sigma = 1$ (no MOA, black curve) and $\sigma = 1.2 - 0.3i$ (with MOA, blue and red curves).

I have fitted the curves in Figs. 4.7(a) and 4.7(b) with the corresponding equation (4.4.a), (4.5.a), (4.6.a) or (4.7.a). Table 4.1 summarizes the obtained values. The table also includes the case of $\sigma = 1.2$, a pure real number, in order to confirm that when $\sigma \in \mathbb{R}$ $\Delta_1 = \Delta_2$ and $\Delta'_3 = \Delta'_4$. In Appendix A I show this analytically, and closed forms for $\tan \Delta_1 = \tan \Delta_2$ and $\tan \Delta'_3 = \tan \Delta'_4$ are given for the case of $\sigma \in \mathbb{R}$ as:

$$\tan \Delta_1 = \tan \Delta_2 = \frac{(\sigma-1) \sin \phi_0 \cos \phi_0}{\sigma \cos^2 \phi_0 + \sin^2 \phi_0} \quad (4.8.a)$$

$$\tan \Delta'_3 = \tan \Delta'_4 = \frac{(1-\sigma) \sin \phi_0 \cos \phi_0}{\cos^2 \phi_0 + \sigma \sin^2 \phi_0} \quad (4.8.b)$$

The value of the phase shifts obtained analytically from (4.8.a) and (4.8.b) for the case with $\sigma = 1.2$ and $\phi_0 = 15^\circ$ coincide with the fit of the simulations. Finally, we have to stress that the fact that the R^2 of the fit is 1 indicates that Eqs. (4.4.a), (4.5.a), (4.6.a) and (4.7.a) still hold even if the SiO_2 layer is included in the formulation.

c) Least-squares fit of the experimental data

The experimental data that we want to fit with this model consist of the measured $NB_i, i = 1,4$ parameters as a function of the applied field. When fitting the $4n$ experimental data with $n + 4$ parameters (n ϕ 's, one for each field value, and 4 phase shifts $\Delta_1, \Delta_2, \Delta'_3$ and Δ'_4 that do not depend on the field), we obtain a good fit to the measured quantities, as it may be observed in Fig 4.8. The fitting is performed by minimizing χ^2 given in Eq. (4.2) but the expected values of the normalized B_i 's (\overline{NB}_i) are given by Eqs. (4.4.a), (4.5.a), (4.6.a) and (4.7.a).

$\sigma = 1$	$\Delta_1 = 0^\circ$	$R^2 = 1$
	$\Delta_2 = 0^\circ$	$R^2 = 1$
	$\Delta'_3 = 0^\circ$	$R^2 = 1$
	$\Delta'_4 = 0^\circ$	$R^2 = 1$
$\sigma = 1.2 - 0.3i$	$\Delta_1 = -4.9^\circ$	$R^2 = 1$
	$\Delta_2 = -66.9^\circ$	$R^2 = 1$
	$\Delta'_3 = 7.4^\circ$	$R^2 = 1$
	$\Delta'_4 = 2.0^\circ$	$R^2 = 1$
$\sigma = 1.2$	$\Delta_1 = 2.4^\circ$	$R^2 = 1$
	$\Delta_2 = 2.4^\circ$	$R^2 = 1$
	$\Delta'_3 = -2.8^\circ$	$R^2 = 1$
	$\Delta'_4 = -2.8^\circ$	$R^2 = 1$

Table 4.1. Fitted phase shifts using Eqs. (4.4.a), (4.5.a), (4.6.a) and (4.7.a) for NB_1 , NB_2 , NB_3 and NB_4 respectively. R^2 values are shown in the right column.

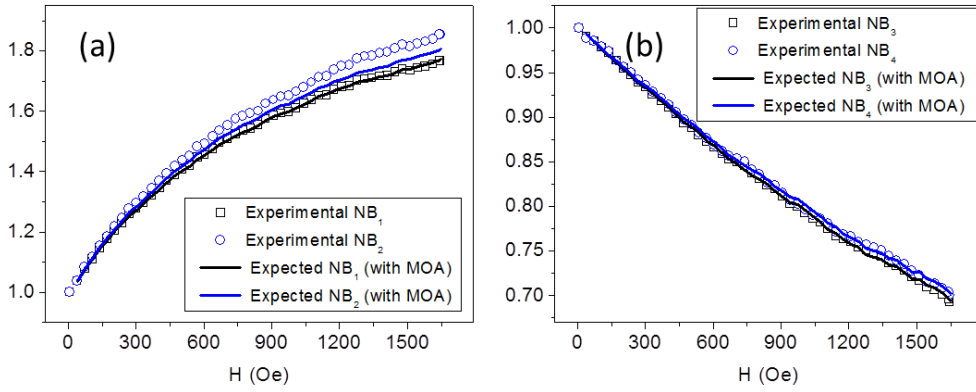


Fig. 4.8. B_1 and B_2 (a), and B_3 and B_4 (b) normalized to their respective remanence values vs. applied field strength H . Black squares and blue circles represent experimental values. Lines represent the fits with equations (4.4.a), (4.5.a), (4.6.a) and (4.7.a).

The inclusion of the Δ_1 , Δ_2 , Δ'_3 and Δ'_4 phase shifts affects the fit, and the magnetization angles $\phi(H)$ are changed with respect to the fit that assumes magneto-optical isotropy. Figure 4.9 shows the fitted ϕ values for the same NB_i data set corresponding to the subsample of Pt20B which has 1.36 nm Pt overcoat. The red curve corresponds to the $\phi(H)$ that has been fitted assuming no MOA [(Eqs. (4.1.a-b)], while the blue curve corresponds to the fit that includes MOA [Eqs. (4.4.a), (4.5.a), (4.6.a) and (4.7.a)]. As it may be observed, if MOA is not included, the error in ϕ can be very large. A pure magnetometry interpretation of data obtained by means of magneto-optical measurements is not correct, and this is due to the fact that MOA mixes the components of the magnetization. However, when MOA is included, ϕ can be determined correctly and, moreover, the level of MOA can be quantified thanks to the Δ_1 , Δ_2 , Δ'_3 and Δ'_4 phase shifts.

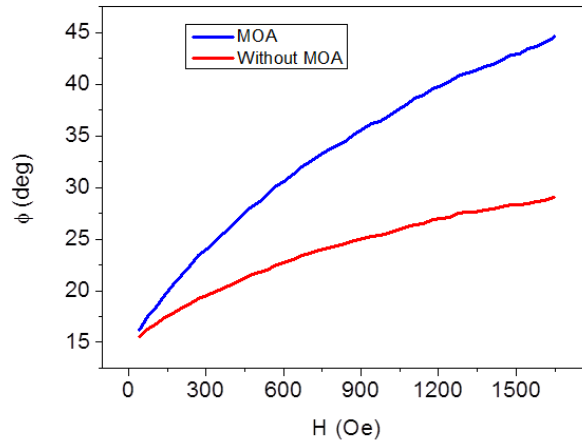


Fig. 4.9. ϕ vs H fitting the data to the model without MOA (red curve), and to the model including MOA (blue curve).

4.4- Overcoat thickness dependence of magneto-optical anisotropy

We have seen that the specific sample we selected to exemplify the data analysis (20 nm Co with 1.36 Pt overcoat) shows MOA. We will now see that the effect of MOA is very substantially affected by the thickness of the Pt overcoat. This is readily visible in Fig. 4.10. In this figure one can see represented with filled squares the NB_1 and NB_3 values measured at different points in the Pt20B sample, corresponding to different overcoat thicknesses. The lines represent the fitted values with the assumption of pure rotation of the magnetization in the absence of MOA [Eqs (4.1a-b)]. As we can see, the accuracy of the fit, which is already poor for the thinnest Pt value, decreases even further when the Pt overcoat gets thicker: for the blue line (0.24 nm of Pt) there is a substantial discrepancy, but for the purple line (1.40 nm of Pt) the discrepancy is even larger. This is an indicator that the effect of MOA increases with Pt overcoat thickness. In Fig. 4.10 one can also observe that the effect of increasing the Pt thickness is mostly affecting NB_1 rather than NB_3 . It is also confirmed, although it is not shown in Fig. 4.10, that NB_2 is affected very substantially, while NB_4 behaves similar to NB_3 , changing very little from measurement point to measurement point.

The inclusion of MOA and the corresponding fitting with Eqs. (4.4.a), (4.5.a), (4.6.a) and (4.7.a) recovers the consistency and the fitted curves are in very good agreement with the measured quantities, as it may be seen in Fig. 4.11. For each of the subsamples, corresponding to a different Pt overcoat thickness, we have a set of Δ_1 , Δ_2 , Δ'_3 and Δ'_4 phase shift fitting parameters, as well as as much ϕ magnetization angles as values of the applied field. The phase shifts are assumed to be independent from subsample to subsample.

The values of Δ_1 , Δ_2 , Δ'_3 and Δ'_4 obtained from the fitting for each subsample of Pt20B are represented in Fig. 4.12 as a function of the Pt overcoat thickness. As we can see, Δ'_3 and Δ'_4 are virtually identical and hardly vary with Pt thickness, even if there are some point-to-point fluctuations. However, Δ_1 and Δ_2 show a clear modulation, and even if their values are not identical, they are very close to each other.

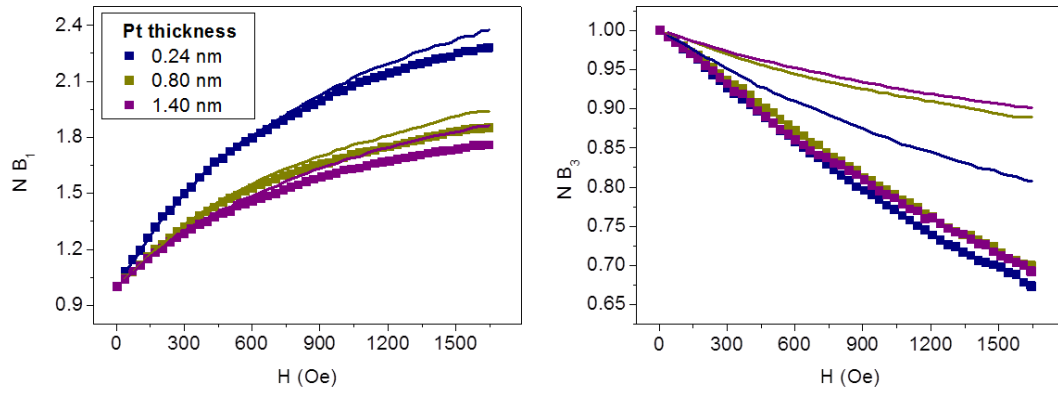


Fig. 4.10. B_1 and B_3 normalized to their remanence value as a function of the applied field, for different Pt overcoat thicknesses. Filled squares represent the experimental values, and lines the expected values assuming no MOA, calculated with Eqs. (4.1.a) and (4.1.b).

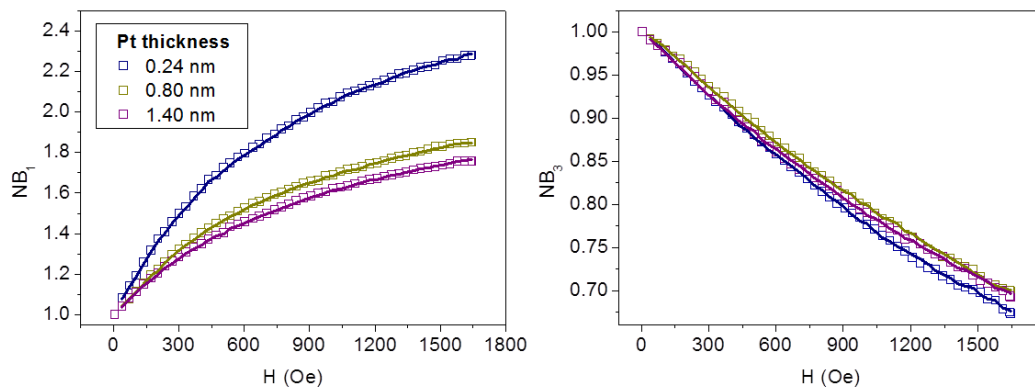


Fig. 4.11. B_1 and B_3 normalized to their remanence value as a function of the applied field, for different Pt overcoat thicknesses. Open squares represent the experimental values and lines correspond to the fitted values assuming MOA.

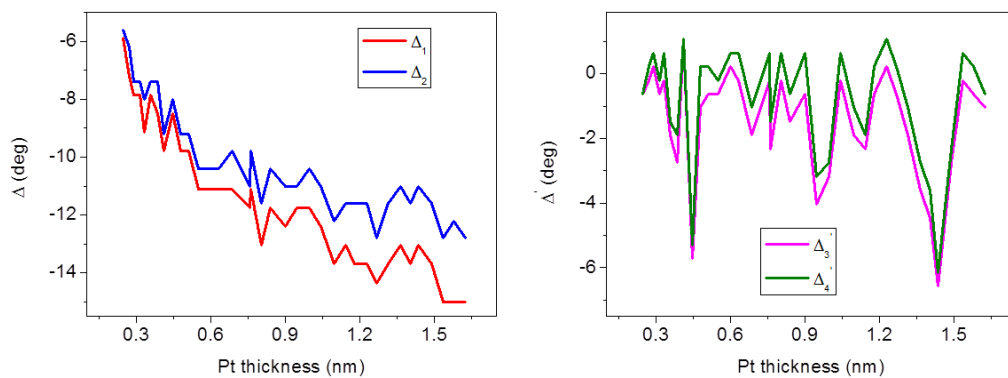


Fig. 4.12. Δ_1 , Δ_2 , Δ_3 and Δ_4 vs Pt overcoat thickness for the Pt20B sample.

Until now we have only focused on the Pt20B sample. However, the effect of MOA is also very important in Ref20B and Pt100B. As an indicative value of the level of MOA, Fig. 4.13 shows the phase shift Δ_1 obtained from fitting the NB_i data sets of each of the measured subsamples in samples Ref20B, Pt100B and Pt20B. The values of Δ_1 are plotted as a function of the Pt thickness. The Pt thickness quantity is meaningless for the Ref20B sample, which does not have the Pt overcoat. In this case, the horizontal axis is the measurement position in the strip. The correspondence between Pt thickness and the position in the strip is given by the profile of the Pt wedge in the right-hand side axis of Fig. 3.5. The first thing I would like to stress about Fig. 4.13 is the fact that the Δ_1 phase shift of the reference sample Ref20B does not show any position dependence. The mean value of Δ_1 for Ref20B is -3.9° and is depicted as a horizontal green line in the figure. This confirms that the effect seen in the other two samples, the ones with a Pt overcoat, is related to the presence of the overcoat, and not to sample inhomogeneity or to possible misalignments in the experiment. On the other hand, we can observe that the dependence of Δ_1 with Pt thickness in Pt100B and Pt20B is very well described by an exponential, with a multiplicative constant A , a decay length t_0 and an offset y_0 .

$$\Delta_1(t_{Pt}) = A \left(1 - e^{-\left(\frac{t_{Pt}}{t_0}\right)} \right) + y_0 \quad (4.9)$$

The exponential fits to the data are shown in red and black lines in Fig. 4.13. The decay length t_0 is found to be 0.60 nm for Pt100B and 0.73 nm for Pt20B. A saturation of the effect of the Pt thickness appears around 1.5 nm of Pt. Additionally, I would like to point out the extrapolations of Δ_1 values to zero Pt thickness are very well in accordance with the Δ_1 of the sample without an overcoat. Δ_2 values for the three samples shows a behavior almost identical to the respective Δ_1 phase shift, whereas Δ'_3 and Δ'_4 show no dependence on the overcoat thickness, as it is already seen in Fig. 4.12 for Pt20B.

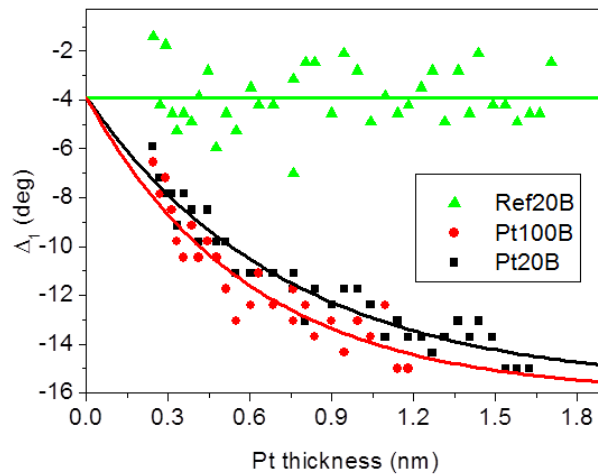


Fig. 4.13. Δ_1 as a function of Pt thickness for Pt100B (red circles) and Pt20B (black squares). The values for Ref20B (green triangles) are data for different measurement positions on the strip. The green horizontal line represents the mean value of Δ_1 for the Ref20B sample. Red and black lines are the exponential fit for the Pt100B and Pt20B data respectively.

We should also point out that behavior of Δ_1 and Δ_2 as a function of Pt thickness is very similar for samples Pt20B and Pt100B. This is the case because magneto-optical properties, which depend on the overlap of electronic wave-functions, have a short length-scale. Thus, the effect of the Pt overcoat in the MOA is similar in samples with 20 nm or 100 nm Co.

From Eq. (4.8.a) we can estimate the value of σ in our samples assuming that $\sigma \in \mathbb{R}$. With a $\Delta_1 \approx -15^\circ$ phase shift we get a value of $\sigma = 0.46$. This means that the value of Q_{\parallel} , the magneto-optical coupling along the EA, is more than double the value of Q_{\perp} , so obviously, the assumption of magneto-optical isotropy in this system is not justified. Without the Pt overcoat, $\Delta_1 \approx -4^\circ$ and we get $\sigma = 0.78$, which is closer to the magneto-optically isotropic case $\sigma = 1$, but still shows a significant level of MOA.

4.5- Overcoat thickness dependence of magnetocrystalline anisotropy

Once we have corrected for the MOA, we can analyze the magnetocrystalline anisotropy (MCA) by studying the ϕ angle of the magnetization and dependence on the applied field. I have obtained the value of ϕ for each value of H from the kind of fittings discussed in Sec. 4.3.2. Figure 4.14 shows ϕ as a function of H for the three different subsamples of Pt20B that have been discussed in Figs. 4.10 and 4.11. For $H = 0$ the angle of the magnetization is $\phi = \phi_0 = 15^\circ$. As H increases, ϕ also increases, i.e., the magnetization rotates towards the axis of the applied field. However, the rotation is not the same for subsamples with different Pt overcoat thickness: the measurements on the thin end of the wedge show a bigger rotation of the magnetization than those on the thick end. Correspondingly, we can say, at least qualitatively, that increasing the Pt overcoat thickness increases magnetocrystalline anisotropy of Co, because for the same value of the applied field, the magnetization rotates less than for thinner Pt overcoats.

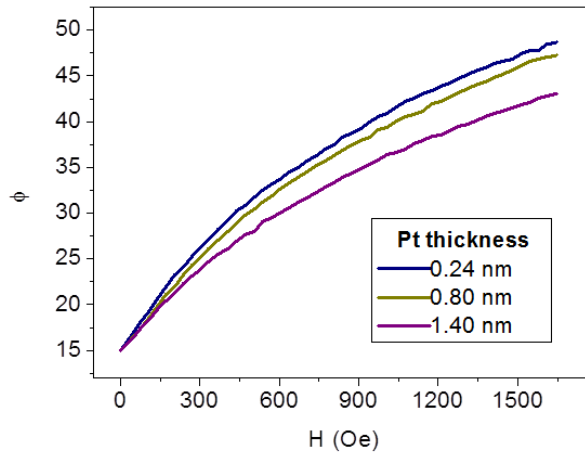


Fig. 4.14. ϕ vs H for different Pt overcoat thickness. For this fitting, $\Delta_3=\Delta_4$ are fixed to be the average of Δ_3 for all Pt thicknesses, because its value does not change with the overcoat thickness. Δ_1 and Δ_2 are optimized as free fit parameters in each case.

This can also be observed in Fig. 4.15, where I have represented the maximum change of ϕ , i.e., $\phi(H_{\max}) - \phi_0 = \gamma_{\max}$, as a function of the Pt overcoat thickness, for the Pt20B and Pt100B. Even if the noise level is quite high, the effect of the Pt overcoat thickness on the anisotropy is apparent for the Pt20B sample, as γ_{\max} changes by 2° from the thinnest to the thickest overcoat. For Pt100B, however, the trend is not so clear as the Pt thickness increases. This smaller overcoat effect onto the MCA in the sample with a thicker Co film can be understood because Pt only affects the Co at the interface. The net Co quantity is 5 times larger in Pt100B than in Pt20B, and the magnetization reversal is collective behavior of the entire Co film, and not just the interface region. Thus, Pt20B is more sensitive to the change of MCA produced by the Pt overcoat. Finally, we corroborate that for the Ref20B sample there is not a trend of γ_{\max} as a function of the sample position, as one would expect, confirming once again a good homogeneity in the Co layer.

The change in the magnetocrystalline anisotropy can be quantified if we use the Stoner-Wohlfarth model to fit $\phi(H)$ for each subsample. From this fit we can extract the values of $H_{K1} = \frac{2K_1}{M_s}$ and $H_{K2} = \frac{4K_2}{M_s}$, where K_1 and K_2 are the first and second order anisotropy constants in Eq. (1.3). The values of such parameters as a function of the Pt thickness are depicted in Fig. 4.16 for the Pt20B and Pt100B samples. As we can observe, H_{K1} shows a clear increase as a function of the Pt thickness. The data for H_{K2} are more scattered and a clear trend as a function of the Pt thickness is not that clearly noticeable. The same happens for $H_K = H_{K1} + H_{K2}$. The fitting we have performed takes ϕ_0 as a fitting variable, but we can see in Figs. 4.16(d) and 4.16(h) that the fitted value does not deviate from 15° , showing consistency with nominal value of ϕ_0 . These results indicate that there is an enhancement of magnetocrystalline anisotropy as the thickness of the Pt overcoat increases.

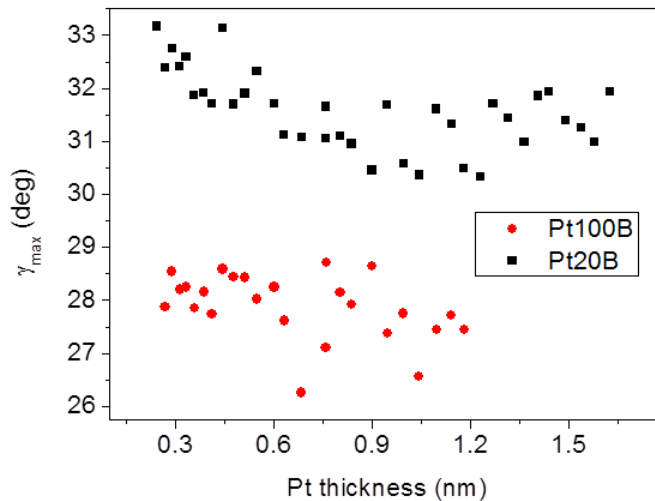


Fig. 4.15. γ_{\max} vs Pt overcoat thickness for Pt20B and Pt100B.

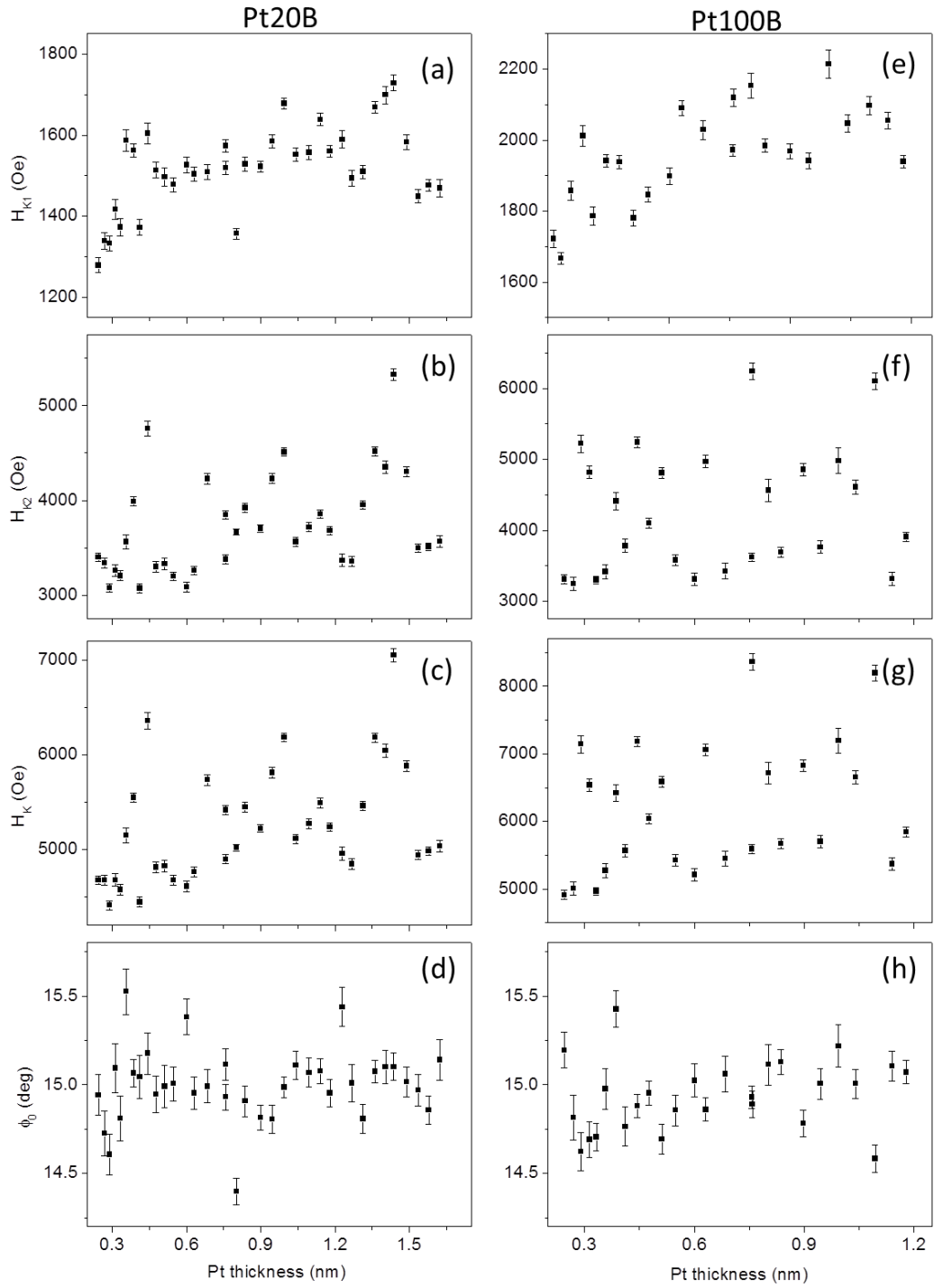


Fig. 4.16. H_{K1} , H_{K2} , H_K and ϕ_0 values obtained from fitting with the Stoner-Wohlfarth model the $\phi(H)$ data.

Chapter 5

VIBRATING SAMPLE MAGNETOMETRY RESULTS

In this chapter I will show the vibrating sample magnetometry (VSM) measurements performed on the Pt20A sample, which confirm that the magnetization of our samples can be described by the Stoner-Wohlfarth model. Moreover, VSM measurements have been used to get a preliminary idea about the change in magnetocrystalline anisotropy upon increasing the Pt overcoat thickness, in order to confirm the results obtained with GME.

To perform VSM measurements, the strip sample Pt20A has been cut into pieces of 5 mm x 5 mm, a size that is suitable for the VSM system. This technique probes the magnetic properties of the sample as a whole, so it is convenient to ascribe to each of the pieces a single value for the Pt thickness. We ascribe to each of the pieces the Pt thickness corresponding to that of the middle point of the piece. Being the gradient of the overcoat wedge so small, it is sensible to neglect the variation of Pt thickness along 5 mm. I have performed VSM measurements on pieces of the Pt20A sample corresponding to Pt thickness values of 0.5 nm, 0.8 nm and 1.4 nm.

The first measurement that I have performed in each piece is intended to locate the easy and hard axes. A large magnetic field is applied (8 KOe in our case), so that saturation is achieved. Then the field is decreased to zero, and the magnetization will thus align with the EA. With the sample in the remanence state, a 360° rotation scan is performed by rotating the sample holder, and the magnetic moment of the sample parallel to the axis of the pickup coils is recorded as a function of the angle. Figure 5.1 shows the outcome of this kind of experiment. The sample is randomly oriented at the beginning, and upon rotating it, we reach a point where the measured magnetic moment is maximal (at 76°). This is the point at which the EA is aligned with the pickup coils. In this way we can identify the EA, and 90° away from it is the HA.

A second measurement is performed to test the orientation of the EA. From the estimate obtained from the first measurement, the sample is oriented with the estimated HA parallel to the pickup coils, and a hysteresis loop is measured, shown in Fig. 5.2(a). The first thing to point out is that the hysteresis loop does not achieve a constant value at large fields (saturation). At large values of the applied field the magnetic moment decreases linearly. The reason for this is that we are not only measuring the ferromagnetic signal of the sample, but also a diamagnetic background coming, for instance, from the substrate or the Si grease used to paste the sample to the sample holder. In order to obtain only the ferromagnetic signal,

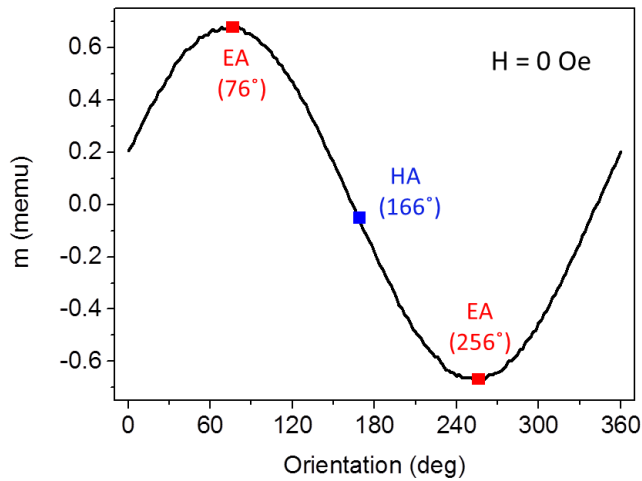


Fig. 5.1. Magnetic moment parallel to the pickup coils as a function of the orientation of the sample for zero applied field (remanence). Starting point is random, depending on how the sample is placed in the instrument.

which should saturate at high fields, one has to subtract the slope of the diamagnetic contribution, obtained from a linear fitting of the high field data points. From the corrected hysteresis loop [Fig. 5.2(b)], we get the value at which the magnetization saturates. In the case of Fig. 5.2(b) this happens at about 4700 Oe. Then, the same measurement as in Fig. 5.1 is performed, but now with an applied field that is enough to saturate the magnetization along the HA. The orientation dependent measurement is depicted in Fig. 5.3. In the Stoner-Wohlfarth model one can fully saturate the sample only along the EA and the HA, and this is exactly what is observed in Fig. 5.3. At certain values of the rotation angle the magnetic moment shows two sudden peaks which correspond to the position of the HA. With this second measurement one can determine more precisely the orientation of the HA, and therefore of the EA.

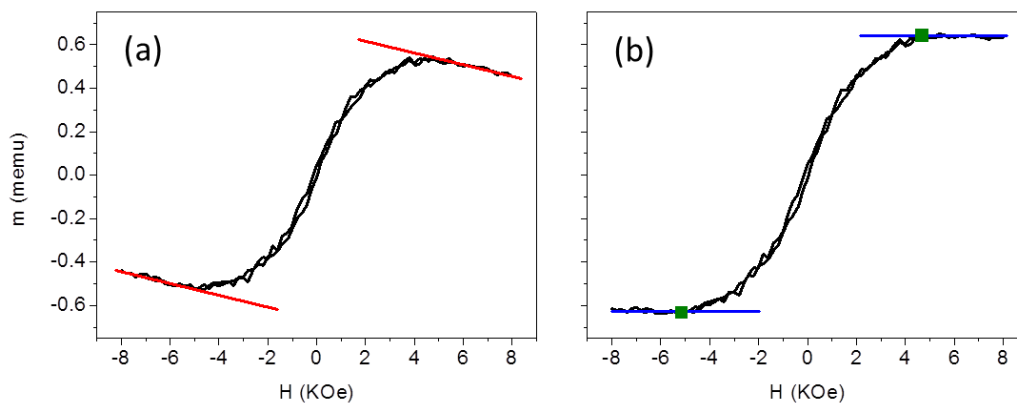


Fig. 5.2. Magnetic moment parallel to the pickup coils vs magnetic field hysteresis loop when the magnetic field is applied along the hard axis. (a) Measured hysteresis loop. (b) Hysteresis loop after correcting diamagnetic linear background.

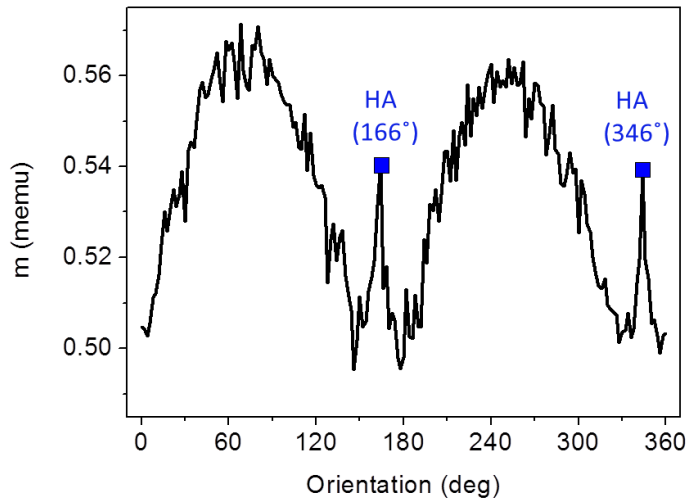


Fig. 5.3. Magnetic moment parallel to the pickup coils as a function of the orientation of the sample for $H = 4700$ Oe (saturation).

The sample is then rotated so that the EA is aligned with the direction along which the field is applied, which in our case is the one parallel to the pickup coils. This is set to be the origin of the rotation angle. With this choice, the angle of rotation of the sample is also the angle δ between the applied field H and the EA. After the alignment, a series of measurements is performed: for each angle δ (in steps of 2°), I have measured a hysteresis loop with applied field from +8 KOe to -8 KOe and back to +8 KOe.

To treat the data, I have first subtracted the linear background due to diamagnetism in each of the hysteresis loops, and correct for possible offsets. The corrected data for magnetic field values from 8 KOe to 0 (from saturation to remanence, the field range where the magnetization of the sample is assumed to be uniform) are shown in the left column of Fig. 5.4 for different pieces corresponding to different Pt overcoat thicknesses. These color maps represent the value of the measured magnetic moment parallel to the pickup coils in color scale, as a function of δ , the angle between the applied field and the EA, and as a function of the strength of the field. One can clearly distinguish the HA, at $\delta = 90^\circ$ and $\delta = 270^\circ$, where at zero field the magnetic moment is zero (blue color), because in such case the magnetization lies along the EA, which is 90° from the HA. As the field increases, above approximately 4500 Oe, we obtain the same value of the magnetic moment at the HA and at the EA.

The right column of Fig. 5.4 shows the fitted maps with the Stoner-Wohlfarth model, including first and second order anisotropy constants. The quality of the fits is excellent, the average R^2 value being 0.9849. Hence, this reinforces the assumption of pure rotation of the magnetization in this range of the applied field.

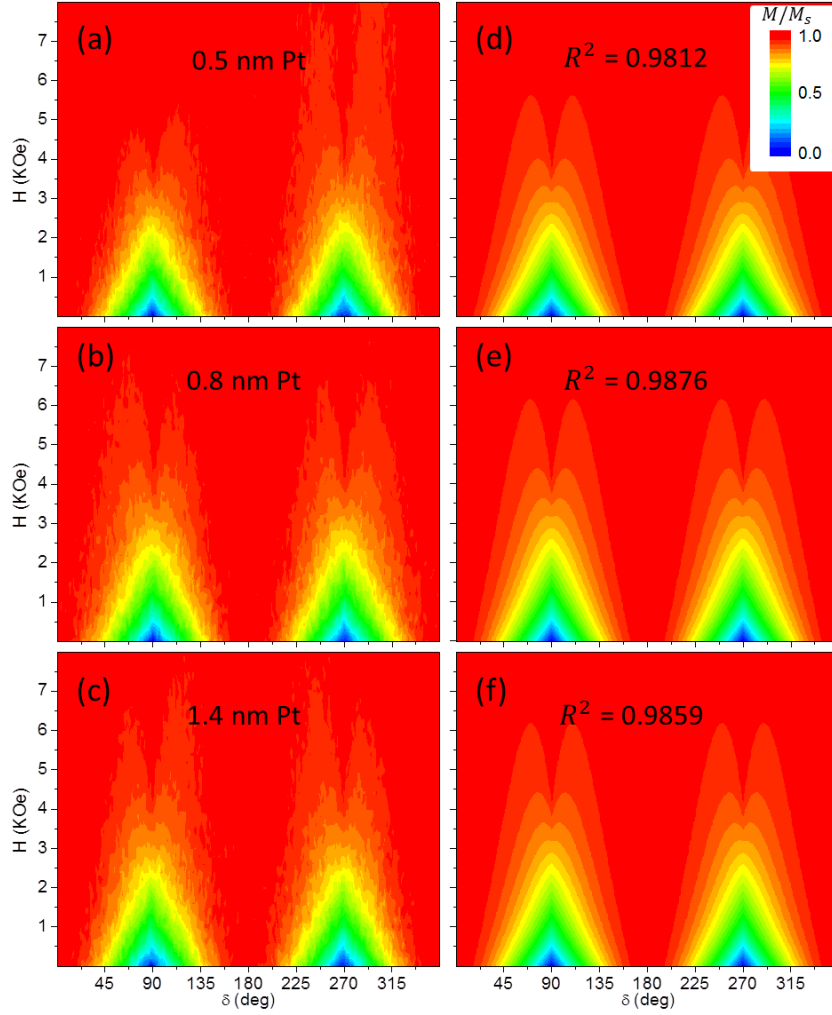


Fig. 5.4. Color maps showing the magnetic moment parallel to the pickup coils as a function of the angle between the applied field and the EA, and as a function of the field strength. Left column [(a) to (c)] are the measured data, right column [(d) to (f)] are the least-squares fits assuming the Stoner-Wohlfarth model.

From the least-squares fits with the Stoner-Wohlfarth model (whose parameters depend on the total magnetic moment of the sample) and the ferromagnetic volume of the pieces (used to normalize the values) we can extract the parameters of the model, namely, the saturation magnetization M_s , and H_{K1} and H_{K2} . Table 5.1 shows these three values for the different pieces.

Pt thickness (nm)	M_s (emu/cm ³)	H_{K1} (Oe)	H_{K2} (Oe)	H_K (Oe)
0.5	1400 ± 100	1740 ± 20	2390 ± 20	4130 ± 30
0.8	1400 ± 100	2060 ± 40	2400 ± 20	4460 ± 50
1.4	1400 ± 100	1950 ± 40	2590 ± 20	4540 ± 50

Table 5.1. M_s , H_{K1} , H_{K2} and $H_K = H_{K1} + H_{K2}$ for the different pieces of Pt20A.

There is an increase in $H_K = H_{K1} + H_{K2}$ upon increasing the Pt thickness. One may note that the values of H_K , H_{K1} and H_{K2} do not coincide with the ones obtained from the GME measurements. Three factors may be relevant here. First, the sample measured via VSM is Pt20A, while GME measurements were performed on Pt20B and Pt100B, so there might be some sample-to-sample variability. Second, there may be a miscalibration of the applied field in the GME experiment that affects the determination of the anisotropy parameters. Finally, in GME we are sensitive to the topmost atomic layers of the structure, and even if in the Co film the magnetization corresponding to different depths is coupled by exchange coupling, the depth-dependent anisotropy coming from the interface-induced effect will cause a depth-dependent magnetization orientation state. Thus, GME probes more the anisotropy near the surface, as opposed to VSM, which is sensitive to all the volume.

More measurements are needed to determine with more accuracy the increase of the anisotropy as the thickness of the overcoat increases. In this regard, work is ongoing and we are measuring more samples with different Pt overcoat thicknesses and with higher precision. Still, the preliminary results shown here indicate an increase of magnetocrystalline anisotropy with the Pt thickness. I would also like to point out that complementary measurements using Brillouin light scattering (BLS) technique are ongoing on our samples, and the results we have obtained also show that the magnetocrystalline anisotropy varies with the Pt overcoat thickness. Thus, adding an ultrathin Pt overcoat could be a promising pathway to increase the magnetocrystalline anisotropy of Co.

CONCLUSIONS

This results show that magneto-optical anisotropy (MOA) can be substantial in crystalline Co thin films. Even if most MOKE studies neglect MOA by considering a constant magneto-optical coupling Q , this approximation is not always valid. Here that not considering the tensor character of Q can lead to a substantial misinterpretation of the angle of magnetization. The generalized magneto-optical ellipsometry (GME) technique, which permits to measure the reflection matrix of the sample, and the analytic derivation of the parameters that we can measure experimentally have enabled me to separate the contribution of the MOA from the rotation of the magnetization. I have shown that the effect of the MOA is to produce a phase shift in the NB_i parameters. By performing least-squares fits of the measured data to the equations I have derived, I have quantified the MOA with the phase shifts Δ_1 , Δ_2 , Δ'_3 and Δ'_4 .

The successful fabrication of epitaxial Co ($10\bar{1}0$) thin films with ultrathin wedge-shaped Pt overcoats by means of sputter deposition has enabled me to investigate systematically how the MOA varies with the thickness of Pt. I have observed an increase of the Δ_1 and Δ_2 parameters upon increasing the Pt thickness up to a limit of 1.5 nm, where the enhancement of the MOA saturates. I also observe that the effect can be described by an exponential law. A very thin layer of Pt (below 2 nm) suffices to produce very substantial variations on the MOA of our samples. Indeed, the difference between the magneto-optical coupling along the easy axis Q_{\parallel} and perpendicular to it Q_{\perp} has been estimated for an overcoat thickness of 1.5 nm, and I have found that $\sigma \approx 0.5$, indicating that Q_{\parallel} is twice as big as Q_{\perp} . We conclude that MOA is very large in this case, with the Pt overcoat. However, we see that even in the case of Co without Pt overcoat MOA is substantial and we estimate a σ of 0.78.

In this regard, we are planning to perform the analysis of the results by applying the transfer-matrix method with a complete optical model that includes magneto-optical anisotropy and possibly optical anisotropy, in order to determine by least-squares fits the optical constants of the Co, as well as Q_{\parallel} and Q_{\perp} , for samples with different Pt overcoat thickness. We envision this model to provide valuable information about the physical mechanism for the MOA enhancement.

As for the magnetocrystalline anisotropy (MCA), the rotation of the magnetization has also been quantified via GME. We observe that when the applied field is maximal the magnetization rotates more towards the field axis, deviating more from the easy axis, when the Pt overcoat is thinner. As the thickness of the overcoat increases, it is more difficult for the magnetization to go away from the easy axis, indicating that MCA is higher for thicker Pt overcoats. Least-squares fits with the Stoner-Wohlfarth model also indicate that MCA increases. Preliminary results obtained by vibrating sample magnetometry and Brillouin light scattering measurements also indicate that there is an increase of MCA when the thickness of the Pt increases.

MCA enhancement has to be further investigated, by performing more accurate VSM measurements and combining these with other methods. This is something we are working on

in order to confirm the enhancement of MCA by Pt overcoats, as well as to find an explanation for the effect.

To sum up, the deposition of an ultrathin layer of Pt on epitaxial Co samples leads to a very substantial enhancement of the magneto-optical anisotropy of Co and could also be used as a pathway to enhance magnetocrystalline anisotropy, which could be relevant for technological applications.

Appendix A

MAGNETO-OPTICAL ANISOTROPY:

CALCULATION OF B_1, B_2, B_3 AND B_4

For a uniaxial magnetic material with an in-plane magnetization of arbitrary angle and the crystallographic c -axis lying in the plane of the film, one finds a dielectric tensor:

$$\bar{\epsilon} = \epsilon \begin{pmatrix} 1 & 0 & iQ_{\perp}m_{\perp} \\ 0 & 1 & -iQ_{\parallel}m_{\parallel} \\ -iQ_{\perp}m_{\perp} & iQ_{\parallel}m_{\parallel} & 1 \end{pmatrix} \quad (\text{A.1})$$

if the c -axis is aligned with the x -axis of the coordinate system. Hereby, we assume the x - y plane to represent the surface plane of the magnetic material. Furthermore, the y -axis is assumed to be in the plane of incidence of the light path considered later. Q_{\parallel} and Q_{\perp} are the magneto-optical coupling constants for the magnetization orientation along the c -axis and perpendicular to it.

If the c -axis is now rotated within the plane of the surface towards the y -axis by an angle ϕ_0 (see Fig. 4.1), we can calculate the new dielectric tensor within the x - y - z laboratory coordinate system as

$$\bar{\epsilon}(\phi_0) = \begin{pmatrix} \cos \phi_0 & -\sin \phi_0 & 0 \\ \sin \phi_0 & \cos \phi_0 & 0 \\ 0 & 0 & 1 \end{pmatrix} \bar{\epsilon} \begin{pmatrix} \cos \phi_0 & \sin \phi_0 & 0 \\ -\sin \phi_0 & \cos \phi_0 & 0 \\ 0 & 0 & 1 \end{pmatrix} \quad (\text{A.2})$$

resulting in:

$$\bar{\epsilon}(\phi_0) = \epsilon \begin{pmatrix} 1 & 0 & \epsilon_{13} \\ 0 & 1 & \epsilon_{23} \\ \epsilon_{31} & \epsilon_{32} & 1 \end{pmatrix}, \quad (\text{A.3.a})$$

with

$$\varepsilon_{13} = \varepsilon_{31}^* = iQ_{\perp}m_{\perp} \cos \phi_0 + iQ_{\parallel}m_{\parallel} \sin \phi_0 \quad (\text{A.3.b})$$

$$\varepsilon_{23} = \varepsilon_{32}^* = iQ_{\perp}m_{\perp} \sin \phi_0 - iQ_{\parallel}m_{\parallel} \cos \phi_0 \quad (\text{A.3.c})$$

and using $m_{\perp} = \sin(\phi - \phi_0)$ and $m_{\parallel} = \cos(\phi - \phi_0)$

$$\varepsilon_{13} = \varepsilon_{31}^* = i\varepsilon[m_y(Q_{\perp} \cos^2 \phi_0 + Q_{\parallel} \sin^2 \phi_0) - m_x \sin \phi_0 \cos \phi_0 (Q_{\perp} - Q_{\parallel})] \quad (\text{A.3.d})$$

$$\varepsilon_{23} = \varepsilon_{32}^* = i\varepsilon[m_y \sin \phi_0 \cos \phi_0 (Q_{\perp} - Q_{\parallel}) - m_x (Q_{\perp} \sin^2 \phi_0 + Q_{\parallel} \cos^2 \phi_0)] \quad (\text{A.3.e})$$

with $m_x = \cos \phi$ and $m_y = \sin \phi$, where ϕ is the magnetization angle visible in Fig. 4.1.

It should be remarked that the dielectric tensor has the same shape and anti-symmetric properties as the original one. Thus, the reflection matrix will have the same symmetry as well and can be calculated simply by replacing the dielectric tensor elements by these new ones.

The reflection matrix can be computed by solving Maxwell's equations with the appropriate boundary conditions [29]. The elements in the reflection matrix

$$\mathbf{R} = \begin{pmatrix} r_s & \alpha \\ -\alpha & r_p + \beta \end{pmatrix} = r_p \begin{pmatrix} \tilde{r}_s & \tilde{\alpha} \\ -\tilde{\alpha} & 1 + \tilde{\beta} \end{pmatrix} = r_p \tilde{\mathbf{R}} \quad (\text{A.4.a})$$

can be written as

$$r_p = \frac{n_1 \cos \Omega_0 - n_0 \cos \Omega_1}{n_1 \cos \Omega_0 + n_0 \cos \Omega_1} \quad (\text{A.4.b})$$

$$r_s = \frac{n_0 \cos \Omega_0 - n_1 \cos \Omega_1}{n_0 \cos \Omega_0 + n_1 \cos \Omega_1} \quad (\text{A.4.c})$$

$$\alpha = \frac{n_0 n_1 \cos \Omega_0 \sin \Omega_1 \varepsilon_{13}}{(n_1 \cos \Omega_0 + n_0 \cos \Omega_1)(n_0 \cos \Omega_0 + n_1 \cos \Omega_1) \cos \Omega_1} \quad (\text{A.4.d})$$

$$\beta = \frac{2n_0 n_1 \cos \Omega_0 \sin \Omega_1 \varepsilon_{23}}{n_1 \cos \Omega_0 + n_0 \cos \Omega_1} \quad (\text{A.4.e})$$

Here, n_0 is the refractive index of the first medium. n_1 is the refractive index of the magnetic material, which is complex. Ω_0 and Ω_1 are the incident and refraction angle respectively. Ω_0 is real, while Ω_1 is related to Ω_0 via Snell's law $n_0 \sin \Omega_0 = n_1 \sin \Omega_1$, so Ω_1 will also be complex.

By writing $n_1 = n + i\kappa$, we have that $\sin \Omega_1 = \frac{n_0 \sin \Omega_0 (n - i\kappa)}{n^2 + \kappa^2}$. $\cos \Omega_1$ is also a complex quantity and we can write $\cos \Omega_1 = c + id$. In the calculation we take $n_0 = 1$, as the first medium in our case is air. We also write ε_{13} and ε_{23} , which are complex numbers, in the following manner:

$$\varepsilon_{13} = i(\tilde{A} + i\tilde{B}) = -\tilde{B} + i\tilde{A} \quad (\text{A.5.a})$$

$$\varepsilon_{23} = i(A + iB) = -B + iA \quad (\text{A.5.b})$$

For the calculation we want to perform we will find this quantities useful:

$$\begin{aligned}
\tilde{\alpha} &= \frac{\alpha}{r_p} = \frac{n_0 n_1 \cos \Omega_0 \sin \Omega_1 \varepsilon_{13}}{(n_0 \cos \Omega_0 + n_1 \cos \Omega_1)(n_1 \cos \Omega_0 - n_0 \cos \Omega_1) \cos \Omega_1} = \\
&= \frac{\cos \Omega_0 \sin \Omega_0 (-\tilde{B} + i\tilde{A})}{[\cos \Omega_0 + nc - \kappa d + i(nd + \kappa c)][n \cos \Omega_0 - c + i(\kappa \cos \Omega_0 - d)](c + id)} \\
&= \frac{\cos \Omega_0 \sin \Omega_0 (-\tilde{B} + i\tilde{A})}{F_1 + i\tilde{F}_1} \propto \\
&\propto (-\tilde{B} + i\tilde{A})(F_1 - i\tilde{F}_1) = -\tilde{B}F_1 + \tilde{A}\tilde{F}_1 + i(\tilde{A}F_1 + \tilde{B}\tilde{F}_1) \tag{A.6.a}
\end{aligned}$$

with

$$\begin{aligned}
F_1 &= c[n \cos^2 \Omega_0 + \cos \Omega_0 (n^2 c - n\kappa d - c) - (nd + \kappa c)(\kappa \cos \Omega_0 - d) - nc^2 + \kappa cd] - \\
&d[(nd + \kappa c)(n \cos \Omega_0 - c) + (\kappa \cos \Omega_0 - d)(\cos \Omega_0 + nc - \kappa d)] \tag{A.6.b}
\end{aligned}$$

$$\begin{aligned}
\tilde{F}_1 &= d[n \cos^2 \Omega_0 + \cos \Omega_0 (n^2 c - n\kappa d - c) - (nd + \kappa c)(\kappa \cos \Omega_0 - d) - nc^2 + \kappa cd] + \\
&c[(nd + \kappa c)(n \cos \Omega_0 - c) + (\kappa \cos \Omega_0 - d)(\cos \Omega_0 + nc - \kappa d)] \tag{A.6.c}
\end{aligned}$$

$$\begin{aligned}
\tilde{\beta} &= \frac{\beta}{r_p} = \frac{2n_0 n_1 \cos \Omega_0 \sin \Omega_1 \varepsilon_{23}}{n_1 \cos \Omega_0 - n_0 \cos \Omega_1} = \frac{2 \cos \Omega_0 \sin \Omega_0 \varepsilon_{23}}{(n + i\kappa) \cos \Omega_0 - (c + id)} \propto (-B + iA)(F_3 - i\tilde{F}_3) = \\
&= (-BF_3 + A\tilde{F}_3) + i(AF_3 + B\tilde{F}_3) \tag{A.7.a}
\end{aligned}$$

with

$$F_3 = n \cos \Omega_0 - c \tag{A.7.b}$$

$$\tilde{F}_3 = \kappa \cos \Omega_0 - d \tag{A.7.c}$$

$$\begin{aligned}
\tilde{r}_s &= \frac{r_s}{r_p} = \frac{(n_0 \cos \Omega_0 - n_1 \cos \Omega_1)(n_1 \cos \Omega_0 + n_0 \cos \Omega_1)}{(n_0 \cos \Omega_0 + n_1 \cos \Omega_1)(n_1 \cos \Omega_0 - n_0 \cos \Omega_1)} = \\
&= \frac{n_1(\cos^2 \Omega_0 - \cos^2 \Omega_1) + \cos \Omega_0 \cos \Omega_1(1 - n_1^2)}{n_1(\cos^2 \Omega_0 - \cos^2 \Omega_1) - \cos \Omega_0 \cos \Omega_1(1 - n_1^2)} = \\
&= \frac{(n + i\kappa)(\cos^2 \Omega_0 - c^2 + d^2 - 2icd) + \cos \Omega_0 (c + id)(1 - n^2 + \kappa^2 - 2in\kappa)}{(n + i\kappa)(\cos^2 \Omega_0 - c^2 + d^2 - 2icd) - \cos \Omega_0 (c + id)(1 - n^2 + \kappa^2 - 2in\kappa)} = \frac{T_1 + iT_2}{T_3 + iT_4} \propto \\
&\propto (T_1 + iT_2)(T_3 - iT_4) = (T_1 T_3 + T_2 T_4) + i(T_2 T_3 - T_1 T_4) \tag{A.8.a}
\end{aligned}$$

with

$$T_1 = n(\cos^2 \Omega_0 - c^2 + d^2) + 2\kappa cd + \cos \Omega_0 [c(1 - n^2 + \kappa^2) + 2n\kappa d] \quad (\text{A.8.b})$$

$$T_2 = \kappa(\cos^2 \Omega_0 - c^2 + d^2) - 2n\kappa c + \cos \Omega_0 [d(1 - n^2 + \kappa^2) - 2n\kappa c] \quad (\text{A.8.c})$$

$$T_3 = n(\cos^2 \Omega_0 - c^2 + d^2) + 2\kappa cd - \cos \Omega_0 [c(1 - n^2 + \kappa^2) + 2n\kappa d] \quad (\text{A.8.d})$$

$$T_4 = \kappa(\cos^2 \Omega_0 - c^2 + d^2) - 2n\kappa c - \cos \Omega_0 [d(1 - n^2 + \kappa^2) - 2n\kappa c] \quad (\text{A.8.e})$$

One can now calculate B_1, B_2, B_3 and B_4 . From now on, $Q_{\perp}^{(r)}$ and $Q_{\perp}^{(i)}$ are the real and imaginary parts of Q_{\perp} , and $Q_{\parallel}^{(r)}$ and $Q_{\parallel}^{(i)}$ the real and imaginary parts of Q_{\parallel} :

$$\begin{aligned} B_1 = \text{Re}(\tilde{\alpha}) \propto -\tilde{B}F_1 + \tilde{A}\tilde{F}_1 = \\ -F_1 \left[m_y \left(Q_{\perp}^{(i)} \cos^2 \phi_0 + Q_{\parallel}^{(i)} \sin^2 \phi_0 \right) - m_x \sin \phi_0 \cos \phi_0 \left(Q_{\perp}^{(i)} - Q_{\parallel}^{(i)} \right) \right] + \\ \tilde{F}_1 \left[m_y \left(Q_{\perp}^{(r)} \cos^2 \phi_0 + Q_{\parallel}^{(r)} \sin^2 \phi_0 \right) - m_x \sin \phi_0 \cos \phi_0 \left(Q_{\perp}^{(r)} - Q_{\parallel}^{(r)} \right) \right] \end{aligned} \quad (\text{A.9.a})$$

Recalling that $m_x = \cos \phi$ and $m_y = \sin \phi$, we have that

$$B_1 \propto C_1 \cos \phi + D_1 \sin \phi \quad (\text{A.9.b})$$

with

$$C_1 = \left[F_1 \left(Q_{\perp}^{(i)} - Q_{\parallel}^{(i)} \right) - \tilde{F}_1 \left(Q_{\perp}^{(r)} - Q_{\parallel}^{(r)} \right) \right] \sin \phi_0 \cos \phi_0 \quad (\text{A.9.c})$$

$$D_1 = -F_1 \left(Q_{\perp}^{(i)} \cos^2 \phi_0 + Q_{\parallel}^{(i)} \sin^2 \phi_0 \right) + \tilde{F}_1 \left(Q_{\perp}^{(r)} \cos^2 \phi_0 + Q_{\parallel}^{(r)} \sin^2 \phi_0 \right) \quad (\text{A.9.d})$$

$$\begin{aligned} B_2 = \text{Re}(\tilde{\tau}_5 \tilde{\alpha}^*) \propto (T_1 T_3 + T_2 T_4)(-\tilde{B}F_1 + \tilde{A}\tilde{F}_1) + (T_2 T_3 - T_1 T_4)(\tilde{A}F_1 + \tilde{B}\tilde{F}_1) = \\ = \tilde{B}F_2 + \tilde{A}\tilde{F}_2 \end{aligned} \quad (\text{A.10.a})$$

with

$$F_2 = -F_1(T_1 T_3 + T_2 T_4) + \tilde{F}_1(T_2 T_3 - T_1 T_4) \quad (\text{A.10.b})$$

$$\tilde{F}_2 = F_1(T_2 T_3 - T_1 T_4) + \tilde{F}_1(T_1 T_3 + T_2 T_4) \quad (\text{A.10.c})$$

By replacing \tilde{A} and \tilde{B} as before we get to

$$B_2 \propto C_2 \cos \phi + D_2 \sin \phi \quad (\text{A.10.d})$$

with

$$C_2 = \left[-F_2 (Q_{\perp}^{(i)} - Q_{\parallel}^{(i)}) - \tilde{F}_2 (Q_{\perp}^{(r)} - Q_{\parallel}^{(r)}) \right] \sin \phi_0 \cos \phi_0 \quad (\text{A.10.e})$$

$$D_2 = F_2 (Q_{\perp}^{(i)} \cos^2 \phi_0 + Q_{\parallel}^{(i)} \sin^2 \phi_0) + \tilde{F}_2 (Q_{\perp}^{(r)} \cos^2 \phi_0 + Q_{\parallel}^{(r)} \sin^2 \phi_0) \quad (\text{A.10.f})$$

$$\begin{aligned} B_3 = \text{Re}(\tilde{\beta}) \propto -BF_3 + A\tilde{F}_3 = -F_3 \left[m_y \sin \phi_0 \cos \phi_0 (Q_{\perp}^{(i)} - Q_{\parallel}^{(i)}) - m_x (Q_{\perp}^{(i)} \sin^2 \phi_0 + \right. \\ \left. Q_{\parallel}^{(i)} \cos^2 \phi_0) \right] + \tilde{F}_3 \left[m_y \sin \phi_0 \cos \phi_0 (Q_{\perp}^{(r)} - Q_{\parallel}^{(r)}) - m_x (Q_{\perp}^{(r)} \sin^2 \phi_0 + Q_{\parallel}^{(r)} \cos^2 \phi_0) \right] = \\ C_3 \cos \phi + D_3 \sin \phi \end{aligned} \quad (\text{A.11.a})$$

with

$$C_3 = F_3 (Q_{\perp}^{(i)} \sin^2 \phi_0 + Q_{\parallel}^{(i)} \cos^2 \phi_0) - \tilde{F}_3 (Q_{\perp}^{(r)} \sin^2 \phi_0 + Q_{\parallel}^{(r)} \cos^2 \phi_0) \quad (\text{A.11.b})$$

$$D_3 = \left[-F_3 (Q_{\perp}^{(i)} - Q_{\parallel}^{(i)}) + \tilde{F}_3 (Q_{\perp}^{(r)} - Q_{\parallel}^{(r)}) \right] \sin \phi_0 \cos \phi_0 \quad (\text{A.11.c})$$

Finally,

$$\begin{aligned} B_4 = \text{Re}(\tilde{r}_3 \tilde{\beta}^*) \propto (T_1 T_3 + T_2 T_4) (-BF_3 + A\tilde{F}_3) + (T_2 T_3 - T_1 T_4) (AF_3 + B\tilde{F}_3) = \\ = BF_4 + A\tilde{F}_4 \end{aligned} \quad (\text{A.12.a})$$

with

$$F_4 = -F_3 (T_1 T_3 + T_2 T_4) + \tilde{F}_3 (T_2 T_3 - T_1 T_4) \quad (\text{A.12.b})$$

$$\tilde{F}_4 = F_3 (T_2 T_3 - T_1 T_4) + \tilde{F}_3 (T_1 T_3 + T_2 T_4) \quad (\text{A.12.c})$$

By replacing A and B as before we get to

$$B_4 \propto C_4 \cos \phi + D_4 \sin \phi \quad (\text{A.12.d})$$

with

$$C_4 = -F_4 (Q_{\perp}^{(i)} \sin^2 \phi_0 + Q_{\parallel}^{(i)} \cos^2 \phi_0) - \tilde{F}_4 (Q_{\perp}^{(r)} \sin^2 \phi_0 + Q_{\parallel}^{(r)} \cos^2 \phi_0) \quad (\text{A.12.e})$$

$$D_4 = \left[F_4 (Q_{\perp}^{(i)} - Q_{\parallel}^{(i)}) + \tilde{F}_4 (Q_{\perp}^{(r)} - Q_{\parallel}^{(r)}) \right] \sin \phi_0 \cos \phi_0 \quad (\text{A.12.f})$$

I have proved that the expressions for these four B_i parameters may be arranged in such way that they can all be written as $B_i \propto C_i \cos \phi + D_i \sin \phi$, with real C_i and D_i .

This can be written as $B_i \propto \sin(\phi - \Delta_i)$ or alternatively as $B_i \propto \cos(\phi - \Delta_i')$. This enables us to write the B_i 's normalized to their remanence value in the form

$$NB_i = \frac{\sin(\phi - \Delta_i)}{\sin(\phi_0 - \Delta_i)}, i = 1, 2 \quad (\text{A.13})$$

with $\tan \Delta_1 = -\frac{C_1}{D_1}$ and $\tan \Delta_2 = -\frac{C_2}{D_2}$

and

$$NB_i = \frac{\cos(\phi - \Delta'_i)}{\cos(\phi_0 - \Delta'_i)}, i = 3, 4 \quad (\text{A.14})$$

with $\tan \Delta'_3 = \frac{D_3}{C_3}$ and $\tan \Delta'_4 = \frac{D_4}{C_4}$.

The sine form is used for NB_1 and NB_2 , because without MOA they have the form of a sine, being $\Delta_1 = \Delta_2 = 0$, while the cosine form is used for NB_3 and NB_4 , since in the case of having no MOA they have the form of a cosine, being $\Delta'_3 = \Delta'_4 = 0$ ⁹.

The expressions that I have derived relate the phase shifts fitted in Sec. 4.3.2 to the optical and magneto-optical properties of the material.

I should also point out that even with MOA ($Q_{\perp} \neq Q_{\parallel}$), if the σ proportionality constant between Q_{\perp} and Q_{\parallel} , ($Q_{\perp} = \sigma Q_{\parallel}$) is real, then $NB_1 = NB_2$ and $NB_3 = NB_4$. If $\sigma \in \mathbb{R}$, then $Q_{\perp}^{(r)} = \sigma Q_{\parallel}^{(r)}$ and $Q_{\perp}^{(i)} = \sigma Q_{\parallel}^{(i)}$. This simplifies the expressions for $\tan \Delta_1, \tan \Delta_2, \tan \Delta'_3$ and $\tan \Delta'_4$:

$$\tan \Delta_1 = \tan \Delta_2 = \frac{(\sigma - 1) \sin \phi_0 \cos \phi_0}{\sigma \cos^2 \phi_0 + \sin^2 \phi_0} \quad (\text{A.15.a})$$

$$\tan \Delta'_3 = \tan \Delta'_4 = \frac{(1 - \sigma) \sin \phi_0 \cos \phi_0}{\cos^2 \phi_0 + \sigma \sin^2 \phi_0} \quad (\text{A.15.b})$$

These expressions are confirmed by the simulations with real values of σ , and this approximation is used to estimate the value of σ in our samples.

⁹ If $Q_{\perp} = Q_{\parallel}$, $C_1 = C_2 = D_3 = D_4 = 0$, so $\Delta_1 = \Delta_2 = \Delta'_3 = \Delta'_4 = \text{atan } 0 = 0$.

REFERENCES

- [1] M. J. Freiser, "A Survey of Magneto-optic Effects", *IEEE Trans. Magn.* **4**, 142 (1968).
- [2] J. Kerr, "On Rotation of the Plane of Polarization by Reflection from the Pole of a Magnet", *Philos. Mag.* **3**, 339 (1877); "Reflection of Polarized Light from the Equatorial Surface of a Magnet", *Philos. Mag.* **5**, 161 (1878).
- [3] Z.Q. Qiu, and S. D. Bader, "Surface magneto-optic Kerr effect (SMOKE)", *J. Magn. Magn. Mater.* **200**, 664 (1999).
- [4] Th. Hermann, K. Lüdge, W. Richter, K. G. Georgarakis, P. Pouloupoulos, R. Nünthel, J. Lindner, M. Wahl, and N. Esser, "Optical anisotropy and magneto-optical properties of Ni on preoxidized Cu(110)", *Phys. Rev. B* **73**, 134408 (2006).
- [5] G. S. Krinchik, E. A. Ganshina, and V. S. Gushchin, "Orientation magneto-optic effect in nickel and ferrosilicon monocrystals", *Sov. Phys. JETP* **33**, 115 (1971) [*Zh. Eksp. Teor. Fiz.* **60**, 209 (1971)]; G. S. Krinchik, E. A. Ganshina, and V. S. Gushchin, "Anisotropy of magneto-optical orientation effect in single crystal of nickel", *J. Physique* **32**, C1-1061 (1971).
- [6] E. A. Ganshina, G. S. Krinchik, L. S. Mironova, and A. S. Tablin, "Anisotropy of the magneto-optical properties of cobalt single crystals", *Sov. Phys. JETP* **51**, 329 (1980) [*Zh. Eksp. Teor. Fiz.* **78**, 733 (February 1980)].
- [7]] D. Weller, G. R. Harp, R. F. C. Farrow, A. Cebollada, and J. Sticht, "Orientation dependence of the polar Kerr effect in fcc and hcp Co", *Phys. Rev. Lett.* **72**, 2097 (1994).
- [8] R. M. Osgood III, B. M. Clemens, and R. L. White, "Asymmetric magneto-optic response in anisotropic thin films", *Phys. Rev. B* **55**, 8990 (1997); R. M. Osgood III, K. T. Riggs, A. E. Johnson, J. E. Mattson, C. H. Sowers, and S. D. Bader, "Magneto-optic constants of hcp and fcc Co films", *Phys. Rev. B* **56**, 2627 (1997).
- [9] L. Uba, S. Uba, V. N. Antonov, A. N. Yaresko, T. Ślęzak, and J. Korecki, "Magneto-optical anisotropy study of Fe_n/Au_n superlattices", *Phys. Rev. B* **62**, 13731 (2000).
- [10] D. Schmidt, C. Briley, E. Schubert, and M. Schubert, "Vector magneto-optical generalized ellipsometry for sculptured thin-films", *Appl. Phys. Lett.* **102**, 123109 (2013).
- [11] J. A. Arregi, J. B. González-Díaz, O. Idigoras, and A. Berger, "Strain-induced magneto-optical anisotropy in epitaxial hcp Co- films", submitted (2015).
- [12] D. Weller, H. Brändle, G. Gorman, C.-J. Lin, and H. Notarys, "Magnetic and magneto-optical properties of cobalt-platinum alloys with perpendicular magnetic anisotropy", *Appl. Phys. Lett.* **61**, 2726 (1992).
- [13] T. R. Albrecht, D. Bedau, E. Dobisz, H. Gao, M. Grobis, O. Hellwig, D. Kercher, J. Lille, E. Marinero, K. Patel, R. Ruiz, M. E. Schabes, L. Wan, D. Weller, and T.-W. Wu, "Bit Patterned Media at 1Tdot/in² and Beyond", *IEEE Trans. Magn.* **49**, 773 (2013).
- [14] W. B. Zeper, H. W. van Kesteren, B. A. J. Jacobs, J. H. M. Spruit, and P. F. Carcia, "Hysteresis, microstructure, and magneto-optical recording in Co/Pt and Co/Pd multilayers", *J. Appl. Phys.* **70**, 2264 (1991).
- [15] S. S. Perry, C. M. Mate, R. L. White, G. A. Somorjai, "Bonding and tribological properties of perfluorinated lubricants and hydrogenated amorphous carbon films", *IEEE Trans. Magn.* **32**, 115(1996).
- [16] S. Blundell, "Magnetism in Condensed Matter", Oxford Univ. Press, Oxford, U.K. (2001).
- [17] J. M. D. Coey, "Magnetism and Magnetic Materials", Cambridge Univ. Press, Cambridge, U.K. (2010).
- [18] N. A. Spaldin, "Magnetic Materials. Fundamentals and Applications", Cambridge Univ. Press, Cambridge, U.K. (2011).

- [19] E. C. Stoner, and E. P. Wohlfarth, "A Mechanism of Magnetic Hysteresis in Heterogeneous Alloys", *Phil. Trans. R. Soc. Lond. A* **240** (826), 599 (1948).
- [20] C. Tannous and J. Gieraltowski, "The Stoner–Wohlfarth model of ferromagnetism", *Eur. J. Phys.* **29**, 475 (2008).
- [21] O. Idigoras, "Magnetization reversal behavior of ferromagnetic thin-films and nanostructures", *PhD Thesis*, University of the Basque Country (2014).
- [22] <http://www.ajaint.com/what-is-sputtering.html> (Visited 04/07/15).
- [23] B.D. Cullity and S. Stock, *Elements of X-ray Diffraction*, Prentice-Hall, Inc., New Jersey, U.S.A. (2001).
- [24] M. Birkholz, *Thin Film by X-ray Scattering*, Wiley-VCH Verlag GmbH & Co., Weinheim, Germany (2006).
- [25] M. Yasaka, "X-ray thin-film measurement techniques. V. X-ray reflectivity measurement", *The Rigaku Journal* **26**, 1757 (2010).
- [26] http://www.jawoolam.com/tutorial_1.html (Visited 04/07/15).
- [27] F. Fiorillo, *Metrologia* **47**, S114 (2010).
- [28] J. A. Arregi, "Magnetization reversal mode transition in Co-films", *Master thesis*, University of the Basque Country (2011).
- [29] C.-Y. You and S.-C. Shin, "Generalized analytic formulae for magneto-optical Kerr effects", *J. Appl. Phys.* **84**, 541 (1998).
- [30] S. Visnovsky, "Magneto-optical ellipsometry", *Czech. J. Phys. B* **36**, 625 (1986).
- [31] A. Berger and M.R. Pufall, "Generalized magneto-optical ellipsometry", *Appl. Phys. Lett.* **71**, 965 (1997).
- [32] J. A. Arregi, J. B. Gonzalez-Diaz, E. Bergaretxe, O. Idigoras, T. Unsal, and A. Berger, "Study of generalized magneto-optical ellipsometry measurement reliability", *J. Appl. Phys.* **111**, 103912 (2012).
- [33] A. Berger and M.R. Pufall, "Quantitative vector magnetometry using generalized magneto-optical ellipsometry", *J. Appl. Phys.* **85**, 4583 (1999).
- [34] W. Yang, D. N. Lambeth, and D. E. Laughlin, "Unicrystal Co–alloy media on Si (110)", *J. Appl. Phys.* **85**, 4723 (1999).
- [35] O. Idigoras, A. K. Suszka, P. Vavassori, B. Obry, B. Hillebrands, P. Landeros, and A. Berger, "Magnetization reversal of in-plane uniaxial Co-films and its dependence on epitaxial alignment", *J. Appl. Phys.* **115**, 083912 (2014).
- [36] J. Zak, E. R. Moog, C. Liu, and S. D. Bader, "Magneto-optics of multilayers with arbitrary magnetization directions", *Phys. Rev. B* **43**, 6423 (1991).
- [37] M. Schubert, "Polarization-dependent optical parameters for arbitrarily anisotropic homogeneous layered systems", *Phys. Rev. B* **53**, 4265 (1996).
- [38] <http://refractiveindex.info> (Visited 04/07/15).